LAGRANGIAN SIMULATIONS OF TURBULENT DRAG REDUCTION BY A DILUTE SOLUTION OF POLYMERS IN A CHANNEL FLOW

A DISSERTATION
SUBMITTED TO THE DEPARTMENT OF MECHANICAL ENGINEERING
AND THE COMMITTEE ON GRADUATE STUDIES
OF STANFORD UNIVERSITY
IN PARTIAL FULFILLMENT OF THE REQUIREMENTS
FOR THE DEGREE OF
DOCTOR OF PHILOSOPHY

Vincent Emmanuel Terrapon
June 2005

I certify that I have read this dissertation and that, in my opinion, it is fully adequate in scope and quality as a dissertation for the degree of Doctor of Philosophy.

Parviz Moin
(Principal Adviser)

I certify that I have read this dissertation and that, in my opinion, it is fully adequate in scope and quality as a dissertation for the degree of Doctor of Philosophy.

Eric S.G. Shaqfeh

I certify that I have read this dissertation and that, in my opinion, it is fully adequate in scope and quality as a dissertation for the degree of Doctor of Philosophy.

Sanjiva K. Lele

Approved for the University Committee on Graduate Studies.

Abstract

Much progress in understanding the phenomenon of turbulent drag reduction by polymer additives has been made since its first experimental observation. While the use of direct numerical simulations has achieved significant success and dramatically improved our understanding of the mechanisms associated with polymer drag reduction, a conclusive explanation of the physics associated with the phenomenon is still lacking. In particular, the stretching and relaxtion mechanisms of individual polymer molecules are still unclear since the numerical simulations have relied on a continuum approach to compute the polymer quantities, i.e., solving a constitutive equation in an Eulerian frame of reference. Moreover, the accuracy of these simulations is limited by their need for artificial dissipation to stabilize the simulations.

To overcome these difficulties, one can simulate the polymer phase in a Lagrangian framework, which is well-suited for solving the hyperbolic polymer equations. The Lagrangian approach is characterized by tracking a large number of polymer molecules in the turbulent flow and computing the polymer stresses along their trajectories. This allows an exact description of the dynamics of single molecules and avoids any explicit artificial diffusion - a great advantage over the previous techniques. Moreover, more complex and accurate polymer models can be used to validate the constitutive models.

As a first step, this work attempts to uncover the mechanisms of polymer stretching in turbulent flows using various polymer models with realistic parameters. A topological methodology is applied to characterize the ability of the flow to stretch the polymers. It is found, using conditional statistics, that highly stretched polymer molecules have experienced a strong biaxial extensional flow between quasi-streamwise vortices in the near-wall regions. The extended polymers then relax in regions where the flow is mainly rotational located in and around the quasi-streamwise vortices.

In the second step, a novel numerical method is developed based on a Lagrangian approach to simulate drag reduction. This new method reproduces well all the characteristic features of drag reduced flows. However, a large discrepancy between Eulerian and Lagrangian calculations is found in flows with limited drag reduction. The Eulerian simulations show a much larger mean extension and damp the small scales. However, when the amount of drag reduction is increased, this discrepancy tends to reduce.

Acknowledgements

I would like to express my great appreciation to Professor Parviz Moin, as my adviser, for his wisdom, guidance, and encouragement during the course of this work. He has been a tremendous mentor for me. I also acknowledge Professor Eric S. G. Shaqfeh and Professor Sanjiva K. Lele for invaluable comments and discussions.

I would like to extend my heartfelt appreciation to Dr. Yves Dubief for his exceptional help which facilitated the completion of this work.

I sincerely thank all the Friction Drag Reduction group members. In particular, Prof. Godfried Mungal, Gianluca Iaccarino, Meng Wang, Chris White, Joe Hur, Costas Dimitropoulos, Mansoo Shin, Yongxi Xu, Vijay Somandepalli, John Paschkewitz. provided immeasurable contributions that were vital for the development of this project. I would also like to acknowledge my other friends and fellow graduate students who always encouraged me during my years at Stanford. My school life would not have been a pleasure without them.

I also recognize and appreciate the financial support of the Defense Advanced Research Projects Agency (DARPA), with Dr. Lisa Porter as manager.

Finally, I would like to thank my parents for their constant love. Thier steadfast support gave me the strength and patience to complete an often difficult and trying project.

Contents

List of Tables

List of Figures

Chapter 1

Introduction

The phenomenon of drag reduction by polymer additives has been known for over 50 years (Toms, 1948). In spite of intensive experimental, theoretical and computational studies, complete understanding of the phenomenon is still lacking. Very large drag reductions, up to 80% in some cases, have been observed with extremely dilute solutions of high molecular weight polymers in the parts per million range. These concentrations are far below those that result in a significant increase in shear viscosity, and therefore the drag reduction must be due to factors other than shearing forces.

Friction drag accounts for about 50% of the total drag a ship or submarine encounters. For such large vessels, the friction drag is dramatically increased by the turbulent nature of the flow surrounding them. Therefore, the possibility of controlling turbulent friction drag by injecting small amounts of polymeric material around a sea vessel could dramatically increase its efficiency, e.g. , higher cruise speed, longer range and larger payload.

Key changes in the turbulent structure under drag-reducing conditions indicates that the interactions between polymers and flow structures are at the heart of the mechanism of drag reduction. Therefore, it is instructive to investigate the phenomenon not only from a statistical approach but also to consider the turbulent structures from a more descriptive point a view. First, a few key characteristics of wall bounded turbulent flows will be reviewed in section 1.1. In section 1.2, our present understanding of polymer solution dynamics is presented, since it is a necessary step to elucidate the mechanisms associated with polymer drag reduction. Because polymer solutions are not the only way to achieve drag reduction, a brief description of other drag reduction methods is then given in section 1.3. Finally, previous studies on turbulent drag reduction by dilute polymer solutions are enumerated

and the current state of knowledge is described. In particular, section 1.3.1 summarizes the characteristic features of polymer drag reduction, while analytical and global studies are presented in section 1.3.2. This is followed by a review of numerical and experimental studies in section 1.3.3 and 1.3.4 respectively. The last two sections 1.4 and 1.5 of the chapter briefly describes the objectives and organization of this work.

1.1 Wall bounded turbulent flows

In a flow over a flat plate, the velocity of the fluid at the surface of the plate must vanish due to the fluid viscosity ν, which creates skin friction. The viscous effects are confined in a layer close to the solid surface called the viscous boundary layer. The thickness of this boundary layer depends on the Reynolds number, $Re = UL/\nu$ (U is a scale of variation of velocity in a length scale L), which represents the ratio of inertial and viscous forces.

In a wall bounded turbulent flow, it is evident that close to the wall, the viscosity ν and the wall shear stress τ_w are important parameters. The wall shear stress is defined by

$$\tau_w = \rho\nu \frac{\mathrm{d}U}{\mathrm{d}y}\bigg|_{y=0}, \tag{1.1}$$

where ρ is the density, y the distance from the wall in the wall-normal direction and U the mean velocity profile. From these quantities, one can define the viscous velocity and length scales that are appropriate in the near-wall region. These are the friction velocity,

$$u_\tau = \sqrt{\frac{\tau_w}{\rho}} \tag{1.2}$$

and the viscous length scale,

$$\delta_\nu = \nu\sqrt{\frac{\rho}{\tau_w}} = \frac{\nu}{u_\tau}. \tag{1.3}$$

While the Reynolds number based on the viscous scales, $Re = u_\tau \delta_\nu/\nu$, is identically unity, a friction Reynolds number can be defined by

$$Re^+ = \frac{u_\tau \delta}{\nu} = \frac{\delta}{\delta_\nu}, \tag{1.4}$$

where δ is some characteristic outer length.

The distance from the wall measured in viscous lengths (so called wall units) is denoted

by

$$y^+ = \frac{y}{\delta_\nu} = \frac{u_\tau y}{\nu}. \tag{1.5}$$

It is interesting to note that y^+ corresponds to a local Reynolds number, determining the relative importance of the viscous and turbulent processes. Based on y^+, different layers in the near-wall region have been identified (Pope, 2000). In the viscous sublayer, from the wall up to $y^+ \approx 5$, the Reynolds stress is negligible compared to the viscous stress. While there is a direct effect of molecular viscosity on the shear stress in the viscous wall region, which extends through $y^+ < 50$, this effect is negligible in the outer layer defined by $y^+ > 50$. The most vigorous turbulent activity is contained in the viscous wall region, where the production, dissipation, turbulent kinetic energy and anisotropy all achieve their peak values at y^+ less than 20.

Another division can be defined based on the mean velocity. The viscous sublayer is characterized by a linear relation between the distance from the wall and the velocity

$$U^+ = \frac{U}{u_\tau} = y^+, \tag{1.6}$$

while the so-called log-law region extending from $y^+ > 30$ to $y/\delta < 0.3$ is characterized by a logarithmic velocity profile

$$U^+ = \frac{1}{\kappa} \ln y^+ + B, \tag{1.7}$$

where $\kappa \approx 0.41$ and $B \approx 5.1$ have been determined experimentally. The two regions are connected by the buffer layer, which is a transition region between the viscosity-dominated and turbulence-dominated parts of the flow.

The near-wall region is also populated by quasi-coherent structures. They can be identified by flow visualization, conditional statistics or eduction schemes. In wall bounded flows, one can find low- and high-speed streaks, ejections and sweeps, and vortices, to name just a few (Kline *et al.*, 1967; Kline and Robinson, 1988; Robinson, 1991). The streaks are regions of the flow where the velocity is higher or lower than the mean velocity at a distance from the wall and are usually found very close to the wall. They interact in a self-sustaining way with the mean shear, and the transitory longitudinal vortices that, in their downward regions (sweeps), carry high momentum fluid to the wall, increasing the local skin friction there. The weaker upwelling of fluid (ejection) also carries low momentum fluid away from the wall, but the asymmetry between down-and-upwelling results in a net increase of

drag. These streamwise oriented structures are unsteady, and are thought to arise from secondary and inflectional instabilities of the primary flow. The secondary instabilities in turn support the three-dimensional streaks, leading to a picture in which turbulence is in a nonlinear dynamic statistically steady state. These quasi-coherent structures are important in explaining the mechanism of the regeneration cycle of the near-wall turbulence (Jimenez and Pinelli, 1999,), whose understanding is vital to achieving many engineering objectives.

1.2 Rheology of polymeric liquids

Polymer solutions are solutions of large macromolecules exhibiting a rich rheological behavior. They exhibit particularly strong viscoelastic effects because the molecules are long and easily distorted, even in rather slow flows. At high velocity, the polymer molecule is stretched to many times its undisturbed coiled state. Thus, a solution composed of stretchable molecules can be highly springy. On the other hand, fluids containing a high concentration of long polymer molecules become extremely viscous.

Research toward a molecular understanding of polymer solution dynamics in highly non-equilibrium flows has made tremendous recent advances, helped primarily by two separate occurrences: the development of efficient computer simulations of polymer molecules in flows, and the development of single molecule fluorescence microscopy. The latter has allowed researchers to examine in detail the dynamics of polymer chains in simple planar extensional and shear flows (Perkins *et al.*, 1995; Smith and Chu, 1998; Smith *et al.*, 1999; Babcock *et al.*, 2000; Smith *et al.*, 1996; Hur *et al.*, 2001*a*). Two important results have come from these studies. First, a wide spectrum of modes and time scales are present, even in a mono-dispersed sample, and second, each molecule acts individually in its dynamics such that small changes in configuration (e.g., those engendered by Brownian motion) can qualitatively change the configurational trajectory of a molecule and therefore its associated stress. This is the so-called *molecular individualism* of de Gennes (1997). The resulting wide distribution of polymer configurations has been well documented in both strong extensional flow (Larson *et al.*, 1997, 1999) and to a higher degree, in shear flows (Hur *et al.*, 2001*a*).

A parallel development is that of very detailed Brownian dynamic simulations of DNA molecules in flow (Hur *et al.*, 2001*b*; Larson *et al.*, 1997, 1999; Doyle *et al.*, 1997; Doyle and Shaqfeh, 1998; Doyle *et al.*, 1998; Hur *et al.*, 2000; Dimitrakopoulos, 2004). Earlier bead/spring models have been improved and supplanted by bead/rod models capable of

directly modeling the DNA molecule at the level of a Kuhn step, i.e., the smallest length of orientational persistence along the flexible backbone (Hur *et al.*, 2000). These were first examined using Kramers' chain simulations (Babcock *et al.*, 2000; Hur *et al.*, 2001*b*, 2000), but Evans and Shaqfeh (1996) have developed Kratky-Porod chain simulations, which include a bending energy for the chain and thus capture the worm-like nature of the DNA molecule (Marko and Siggia, 1991). New fast algorithms for the calculation of Brownian dynamics have allowed many hundreds of bead-springs or bead-rods to be included in steady and time-dependent linear flows (Babcock *et al.*, 2000; Kwan *et al.*, 2001). These simulations are fully predictive, involve no parameters that are not independently determined, and quantitatively predict the observed polymer dynamics. Both ensemble-averaged properties such as stress, in both time-dependent and steady flows, and configurational distributions - an indicator of the molecular individualism - can now be predicted from molecularly realistic models (Hur *et al.*, 2001*b*; Doyle *et al.*, 1997; Hur *et al.*, 2000; Li *et al.*, 2000).

Thus, there exists a hierarchy of molecular models which one can use to understand the dynamics of polymer molecules under non-equilibrium flow conditions (see Section 2). Bead-rod models are the most fine-grained that are usually considered in calculations of polymer solution dynamics. At the next level of coarse-graining are the bead-spring models, where the spring now represents a collection of rods which are presumably in a near-equilibrium configuration such that the elastic restoring force can be represented by a nonlinear spring. Recent calculations have shown that the dynamics of DNA can be well represented in extension (Larson *et al.*, 1999), shear (Hur *et al.*, 2000) and the start-up of shear flow (Hur *et al.*, 2001*a*) with between 10 and 20 nonlinearly coupled worm-like springs. Indeed based on the rule of thumb that at least 10-15 Kuhn steps are required to reproduce any of these nonlinear spring laws, a simulation of 10^6 MW (molecular weight) polyethyleneoxide (PEO) would require between 200 and 400 springs (Devanand and Selser, 1991). The most recent algorithms allow the accurate simulation of a 200 bead-spring chain, including ensemble-averaged stress and configuration distribution in extensional flow (Hur *et al.*, 2001*a*; Kwan *et al.*, 2001), over a wide range in Hencky strain in two hours on a single processor.

At the next level of coarse graining, a single nonlinear dumbbell can be used to represent the molecule. This model has been a work-horse for micro-macro simulation methods in complex flows where either particle tracking is used in CONNFFESSIT schemes (Oettinger and Laso, 1992; Laso and Oettinger, 1993) or small Brownian elements are employed in the Brownian configuration fields method (Hulsen *et al.*, 1997) to follow many such dumbbells

in a flow coupled to the solution of the velocity field. At the level of constitutive modeling, one may make further closure approximations and develop a constitutive equation for the continuum polymer stress. For dilute solutions, this leads to a class of Oldroyd, FENE-P or FENE-L models (Keunings, 1997; Lielens *et al.*, 1998). To overcome the shortcomings of the single mode models (Ghosh *et al.*, 1998), Ghosh *et al.* (2002) introduced a new model based on an adaptive length scale (ALS) to reproduce the fine scale physics of the Kramers chain.

There are only a few studies on the dynamics of a realistic polymer model in a stochastic flow field (Thiffeault, 2003; Eckhardt *et al.*, 2002; Chertkov, 2000), but these provide some insight into how a turbulent flow might engender large stretching and concomitant stress. Evans and Shaqfeh (1996) completed Brownian dynamics simulations of a Kratky-Porod chain in a steady, anisotropic Gaussian field and found large stress supported by only a fraction of the molecules in the configurational distribution. More recently the mechanism by which these molecules reach an extended state has been identified as a *burst* mechanism (Shaqfeh *et al.*, 1998) where a coiled molecule enters a region of uniaxial strain, becomes highly extended, and even though the strain does not persist, the molecule fails to relax before it samples another such region. This process creates an extended period of large stretching periodically marked by high stress levels.

1.3 Turbulent drag reduction

Skin-friction reduction in turbulent flow has been investigated by several different passive means such as riblets, large-eddy breakup devices, polymer additions or compliant walls, and by active control, which either modifies the velocity at the wall (blowing, suction, oscillation) or uses of magneto-hydro-dynamic (MHD) forces.

Among the passive means, the surface-mounted riblets have been shown to reduce drag most successfully (as large as 8%). Choi *et al.* (1993) performed a direct numerical simulation of turbulent flows over riblet-mounted surfaces. They observed an upward shift of the log-law for the mean velocity profile, while Reynolds shear stresses, velocity and vorticity fluctuations were decreased. They postulated that the riblets reduce drag by restricting the location of the near-wall streamwise vortices, such that only a limited area of the riblets is exposed to the downwash of high-speed fluid. Therefore, spacing between the riblets must be smaller than the diameter of the vortices.

Choi *et al.* (1994) have explored some concepts for active control of turbulent boundary layers. They could achieve up to 40% drag reduction by partially suppressing the coherent structures present in the near-wall region. Lim *et al.* (1998) investigated the effect of magnetic fluxes in conducting flows. They demonstrated that the induced electromagnetic force inhibits the motion of the streamwise vortices and reduces their strength. Skin-friction drag reduction in a turbulent pipe flow was studied experimentally by Choi and Graham (1998). They obtained up to 40% drag reduction by oscillating a section of the pipe in a circumferential direction.

Despite significant drag reduction, active control is limited by its complexity, energy input and the type of fluids in the case of the MHD. On the other hand, the use of riblets decreases drag by only a small amount and has geometrical constraints. Therefore, there is a strong practical motivation to study drag reduction by dilute concentrations of polymer additives.

1.3.1 Main features of polymer drag reduction

As mentioned above, one can observe very significant amounts of drag reduction with extremely dilute solutions of high molecular weight polymers. These concentrations are far below those that result in a significant increase in shear viscosity: in fact, measurement of any viscoelastic and/or non-Newtonian effects at these concentrations is extremely difficult and has eluded rheologists for some time. Yet the effect is striking and relatively easy to measure in pipes and channels by observing the macroscopic force balance.

The effects on the structure of fully developed wall turbulence has been observed by many experiments and simulations. Key structural changes include an increased spacing and coarsening of streamwise streaks, damping of small spatial scales, reduced streamwise vorticity, enhanced streamwise velocity fluctuations and reduced vertical and spanwise velocity fluctuations and Reynolds stresses. The drag reduction is also characterized by a parallel shift of the log-law portion of the mean velocity profile at Low Drag Reduction (LDR). At High Drag Reduction (HDR) one observes a change in the slope of the log-law (Warholic *et al.*, 1999). There exists a critical Weissenberg number (ratio of the polymer and flow time scales) for the onset of drag reduction, and mechanistic arguments indicate that the effect is the largest when the time scales of turbulence and polymer dynamics are commensurate.

Drag reducing agents encompass a wide range of microstructures including high molecular weight flexible polymers (primarily PEO and polyacrylamide (Sreenivasan and White, 2000; Luchik and Tiederman, 1988; Berman, 1986; Gyr and Bewersdorff, 1995)), semi-flexible polymers (e.g., Xanthan gum, Gyr and Bewersdorff (1995)) and even non-Brownian microfibers (Gyr and Bewersdorff, 1995; McComb and Chan, 1985; Moyls and Sabersky, 1978; Lee *et al.*, 1974). While they all provide drag reduction, the high molecular weight flexible polymers seem to out-perform the others in terms of reduction at a given concentration. Molecular understanding and design of turbulent drag reducing agents is still limited, despite numerous experimental studies.

A remarkable feature of drag reduction by polymers is the apparent existence of a Maximum Drag Reduction (MDR) asymptote (Virk *et al.*, 1967; Virk, 1975), i.e., there appears to be a limit to the degree of drag reduction possible which is independent of polymer molecular weight and structure. There is currently no theoretical explanation for the existence of the MDR, so it is unknown as to whether it represents a fundamental limiting form of the physical laws governing drag reduction, or whether it is empirical observation that, if understood, can be worked around in order to achieve even greater levels of drag reduction.

1.3.2 Analytical and global studies

According to Lumley (1969), the turbulence outside the viscous sublayer stretches the polymer chains at sufficiently large strain rates that leads to a higher effective viscosity in the turbulent region, and therefore an increase in the thickness of the viscous sublayer, while the viscosity in the viscous sublayer remains more or less that of the solvent since the polymer chains are not extended by the shear flow. Drag reduction is then observed since the velocity gradient at the wall decreases. For the polymers to have an effect on the flow, the characteristic relaxation time of a polymer molecule must be longer than the relevant Lagrangian turbulent time scale of the flow requiring almost fully stretched polymers in the buffer layer, which has been shown not to be the case (Ryskin, 1987).

Tabor and de Gennes (1986) contested this explanation and argued that polymers in turbulent flows exhibit elastic properties even at very low concentrations. Therefore, they can store up some of the cascading energy of turbulence. This energy is thus not dissipated by viscosity, and hence gives rise to an effective drag reduction. This theory also predicts the existence of a critical concentration below which drag reduction cannot be observed. In the

light of this theory, the onset of drag reduction and the maximum drag reduction asymptote have been recently re-visited by Sreenivasan and White (2000). Using scaling arguments, they suggested that when both the elastic energy stored by the polymers and the turbulent energy become comparable, the elastic energy interferes with the usual turbulent cascade mechanism. Therefore, the nonlinear action that generates small scales of turbulence is terminated at some scale larger than the Kolmogorov scale. This leads to increased buffer layer thickness and reduced drag. Moreover, the length scale at which the elastic and turbulent energies are comparable depends on the concentration of polymers. At very low concentration, this length scale is smaller than the Kolmogorov scale, and thus the polymers have no effect on the turbulence. This defines a minimum concentration for the onset of drag reduction. Based on similar arguments, they also interpret the maximum drag reduction phenomenon. According to them, the turbulence is modified in such a way that even the weakest rates of strain, characteristic of the large scales, render the polymer elastic energy comparable to the turbulent kinetic energy.

Many other studies have suggested plausible mechanisms for the phenomenon. By analyzing vorticity disturbances in axisymmetric elongational flow, Rabin and Zielinska (1989) showed that the enhancement of large-scale vorticity is a consequence of elastic energy storage by the polymer molecules, thus inhibiting the energy cascade toward the dissipative scales. Ryskin (1987) introduced the so-called *yo-yo* model, in which the polymer chain does not deform affinely with the fluid but unravels if the strain rate exceeds a critical value in extensional flows. During the unraveling process, the central portion produces large additional stresses by a dissipative mechanism. A peculiar aspect of this model is that it predicts a very large polymer effect during the transient deformation, i.e., when the stretching is only partial. Based on this theory, Thirumalai and Bhattacharjee (1996) and Bhattacharjee and Thirumalai (1991) combined a Langevin equation description of polymer solution with the randomly stirred turbulent model of Dominicis and Martin (1979). With this hydrodynamic model for turbulence in dilute polymer solutions they demonstrated that additives lead to an enhancement of the molecular viscosity at small scales, while at intermediate scales the effective viscosity is increased if the concentration of the polymer exceeds a minimum value. They also suggested that non-polymer solutes could also cause drag reduction, provided that cRe^2 is large enough (where c is the concentration of the polymer in the solvent and Re the Reynolds number). Using an Oldroyd-B model, Fouxon and Lebedev (2003) analytically established a power-law spectrum for the elastic turbulence, looking at both the high

Reynolds number turbulence of polymer solutions above the coil-stretch transition, and at small Reynolds numbers where chaotic flow is excited by elastic instabilities.

Benzi and Procaccia (2003) introduced a one-dimensional version of the FENE-P model with the aim of understanding in simple mathematical terms some of the prominent features associated with the phenomenon of drag reduction. They showed that the arguments concerning the turbulent cascade process proposed by de Gennes (1990) do not appear essential. Moreover, drag reduction is a phenomenon which involves energy containing modes rather than dissipative, small scale modes. Since an homogeneous increase in the effective viscosity should lead to drag enhancement rather than reduction, they suggested that it is the space dependence of the polymer stretching, and thus of the effective viscosity, which should be the source of drag reduction. Benzi *et al.* (2003) introduced a shell model for homogeneous viscoelastic flows which resembles the dynamical properties of the FENE-P equations. The observation of drag reduction demonstrates that boundary effects are not essential to capture the basic physics of the phenomenon. Moreover, they confirmed the previous results of Benzi and Procaccia (2003), showing that drag reduction is a property of large scales, which are therefore important for a quantitative theory. Hence, drag reduction cannot be reduced to a simple increase of the dissipation length. In a similar approach, Angelis *et al.* (2004) used a simple model with an effective viscosity growing linearly with the distance from the wall and showed that the decrease in Reynolds stress overwhelms the increase in viscosity, therefore reducing drag. The amount of drag reduction increases with the increase of the slope of the viscosity profile. They also showed that the behavior of the Reynolds stress and the velocity fluctuations in the elastic sublayer are in close correspondence with the full FENE-P model.

Despite many promising results, these different theoretical models fail to give any quantitative prediction of drag reduction. Moreover, they propose very different, and sometimes contradictory, mechanisms for the phenomenon. The more recent results seem to suggest that the spatial and temporal dependence of polymer stretching play an essential role in drag reduction. Therefore, it is obvious that a global analysis of the phenomenon cannot alone lead to a satisfactory theory of polymer drag reduction. Only a more in depth study of the local dynamics of the flow and polymer stretching can provide a conclusive explanation. A very powerful tool towards this goal is provided by numerical simulations.

1.3.3 Numerical simulations

In parallel to the experimental and theoretical investigations, many studies have been based on the numerical solution of the viscoelastic equations, in particular the FENE-P model. Beris and Sureshkumar (1996) were the first to do a direct numerical simulation of a viscoelastic turbulent channel flow and achieved drag reduction using a spectral code and different rheological models. They observed numerical instabilities developing in the conformation tensor shortly after it looses its positive-definiteness. These instabilities induced a break-down of the solution. This issue was addressed by adding a diffusive artificial term to the equations governing the polymer conformation tensor (Sureshkumar *et al.*, 1997). To compensate for the relatively low Reynolds number, $Re^+ = 125$, they simulating more elastic fluids than the ones encountered in drag reduction experiments. In later works, they investigated different models, the effects of the variations in elasticity and inertia, budgets of Reynolds stress, kinetic energy and streamwise enstrophy, and the influence of the artificial diffusion needed to stabilize the numerical simulation (Dimitropoulos *et al.*, 1998; Beris and Dimitropoulos, 1999; Dimitropoulos *et al.*, 2001). They showed that an increase of extensional viscosity induces a consistent decrease of Reynolds stress. The effect of the flow elasticity, which is associated with the reduction in the intensity of the velocity-pressure gradient correlations, leads to a redistribution of the turbulent kinetic energy among the streamwise, wall-normal and spanwise directions. Finally they demonstrated that the viscoelasticity reduces the production of streamwise enstrophy. Angelis *et al.* (2003) investigated the different modes of the velocity field in their spectral simulations. They found that the spatial profile of the most energetic modes was hardly changed between viscoelastic and Newtonian flows. As proposed in some previous theories, drag reduction is seen in the energy containing modes rather than the dissipative modes.

Min *et al.* (2001) investigated spatial discretization schemes used in finite difference methods to solve viscoelastic flows. They demonstrated that the traditional upwind difference and artificial diffusion schemes exhibit much more smeared stress fields that those obtained by higher-order upwind difference schemes. They introduced a *local* artificial diffusion to replace the traditional global diffusion, and demonstrated that their method is stable and accurate for highly extensional flows at relatively high Weissenberg numbers. In a later study, they interpreted the onset mechanism based on elastic theory and found that in order to show drag reduction, the relaxation time of the polymer molecules has to be long enough so that the energy stored in the very near-wall region is transported to, and released

in, the buffer and log layers (Min *et al.*, 2003). Using a finite difference method and the FENE-P model, Baron and Sibilla (1997) and Sibilla and Baron (2002) suggested that polymers can be effective in terms of drag reduction only if their relaxation time is comparable to the characteristic time of their convection in the wall-normal direction within near-wall turbulent structures. They argued that elongated polymers inhibit turbulence regeneration by opposing pressure redistribution from streamwise to cross-flow velocity fluctuations.

At about the same time, Ptasinski *et al.* (2003) and Dubief *et al.* (2004*b*) were the first to simulate the high drag reduction (HDR) regime, at which a change of the slope of the log-law in the mean velocity profile is observed. They demonstrated a very good agreement with experimental results using realistic values for the parameters describing the polymer. They further showed that the Reynolds shear stress is strongly reduced and compensated for partly by a polymer stress. A reduction of energy transfer from the streamwise direction to the other directions was also observed. Moreover, a substantial part of the energy production by the mean flow is transferred directly into the elastic energy of the polymers, which is subsequently dissipated by polymer relaxation. Dubief *et al.* (2005) used numerical experiments to isolate certain features of the interaction between polymers and turbulence. They found that polymers reduce drag by damping near-wall vortices and sustain turbulence by injecting energy into the streamwise velocity component in the very near-wall region. Those findings on the coherent storage and release of energy lead to a new autonomous regeneration cycle of polymer wall turbulence in the spirit of Jimenez and Pinelli (1999,). Their work was expanded by Dimitropoulos *et al.* (2005), who simulated the first viscoelastic turbulent boundary layer. They observed an initial development length, which is followed by a quasi-steady region where variations in drag reduction are weak. Based on their work, Paschkewitz *et al.* (2004) investigated drag-reduced channel and boundary layer flows by rigid fibers (Paschkewitz *et al.*, 2005*a*,*b*). Although the amount of drag reduction is much lower than in the flexible polymer case, they could show that elasticity is not necessary to reduce drag and demonstrated that all the flow features are similar to those of polymer drag-reduced flows. Based on their results, they proposed a mechanism for turbulent drag reduction by rigid fiber additives which is somewhat different from the one by flexible polymer molecules.

To avoid the complication brought by the randomness of a turbulent flow, Stone *et al.* (2002, 2004) investigated a polymer solution in plane Couette flow containing *exact coherent states* (ECS). Despite the simplicity of those flows, it was possible to reproduce all the main

features of polymer turbulent drag reduction. It was found that the polymer molecules become highly stretched in the streamwise streaks, then relax as they move from the streaks into and around the streamwise vortices. This relaxation of the polymer molecules produces a force that directly opposes the fluid motion in the vortices, weakening them.

Direct numerical simulations are very well-suited to assess the different models and to analyze the mechanisms of polymer drag reduction. However, the computational costs prevent simulation at high Reynolds numbers. Therefore, in order to solve complex engineering problems of interest, it is necessary to rely on other methods, such as Large Eddy simulations (LES) and the Reynolds Averaged Navier-Stokes (RANS) approaches. The traditional issues of closure of nonlinear terms are even more complicated in the case of viscoelastic flows since many new terms require closure models. Cruz *et al.* (2004) improved a previous model (Cruz and Pinho, 2003) based on a low Reynolds number $k-\epsilon$ model to compute the new viscoelastic stress term in the momentum equation. However, comparison with DNS of pipe flows showed a large overprediction of drag reduction. Leighton *et al.* (2003) developed a Reynolds-stress transport equation model for turbulent drag-reducing viscoelastic flows. Although the model could predict the mean velocity profile quite well, it relies on parameters which must be calibrated, and was not able to accurately reproduce the anisotropy of the turbulent normal stresses in the near-wall region. Dubief *et al.* (2004*a*) modified the $v^2 - f$ turbulence model introduced by Durbin (1995) and were able to accurately capture the behavior of the mean velocity profile for the low and high drag reduction regimes. Their model was derived from the current understanding of the mechanisms of near-wall turbulence in drag-reduced polymer flows.

While most of the progress made in understanding the mechanisms of polymer drag reduction stemmed from direct numerical simulations and experimental studies, other works approached the problem from a different point of view. Ahlrichs and Duenweg (1998) combined a lattice Boltzmann approach for the fluid and a continuum molecular dynamics model for the polymer chains to solve polymer-solvent systems. Similarly, Ispolatov and Grant (2002) relied on a lattice Boltzmann model for viscoelastic fluids, where elastic effects are taken into account within the framework of a Maxwell model. However, these approaches are limited to low Reynolds number flows and simple geometries, and thus are not practicable for engineering applications.

All the listed studies relied on an Eulerian framework to compute the polymer stress. However, this approach is limited in the number of polymer models which can be used since

it requires a constitutive model such as the FENE-P or Oldroyd-B. It is known that the Oldoyd-B model demonstrates unphysical behavior at large extensions, while the FENE-P model is based on a closure approximation.

The constraint on the models used in the Eulerian approach can be relaxed using the Brownian configuration fields (Oettinger *et al.*, 1997; Hulsen *et al.*, 1997). Another issue related to the Eulerian framework is the need for the addition of artificial dissipation to the constitutive equations to ensure that the conformation tensor associated with the polymer configuration remains positive definite. Because of the hyperbolic nature of the FENE-P equations, it is natural to rely on a Lagrangian framework to compute the quantities associated with the polymer phase. It should be stressed that most of the Lagrangian studies of turbulent polymer solutions are based on uncoupled simulations where only the flow impacts the polymers without any feed-back. Therefore, the flow remains Newtonian. This is evidently an important limitation, although many qualitative features can still be demonstrated.

Massah *et al.* (1993) and Massah and Hanratty (1997) were the first to investigate Lagrangian polymer molecules in a turbulent channel flow. They found that a coil-stretch transition takes place intermittently only in the buffer zone where extensional flows are strong enough to unravel the molecules, and the polymers tend to align at a 7° angle with the direction of mean flow. They also postulated that polymers cause drag reduction by altering the structure of the eddies that produce Reynolds stresses. Their findings were confirmed by Ilg *et al.* (2002), who compared the microscopic and macroscopic descriptions of polymer dynamics and demonstrated that the stretching of the polymers is characterized by a broad distribution of polymer extensions. Zhou and Akhavan (2003) have compared different models and shown that the dominant contributions to the polymer stress arise from patches of biaxial and uniaxial elongational flow encountered in the buffer layer. Stone and Graham (2003) demonstrated in a model of the turbulent buffer layer that stretching of the polymers is determined by the largest Lyapunov exponent for the velocity field and that polymers become highly stretched in the near-wall streaks and relax as they move into and around the streamwise vortex cores. It was demonstrated by Terrapon *et al.* (2003) that the FENE chain, the FENE dumbbell and the FENE-P models give qualitatively similar results. Terrapon *et al.* (2004) showed that the polymers that are stretched to a large fraction of their maximum extensibility have experienced a strong biaxial extensional flow in the near-wall regions around the quasi-streamwise vortices.

Unfortunately, all Lagrangian studies have been limited by the fact that the flow remains Newtonian since the extra polymer stress is not coupled with the flow. To overcome this difficulty, Halin *et al.* (1998) introduced the Lagrangian particle method (LPM) to compute the start-up flow between slightly eccentric rotating cylinders. They extended their method to the adaptive Lagrangian particle method (ALPM) (Gallez *et al.*, 1999; Wapperom *et al.*, 2000), where the local number of particles is adapted dynamically by creating and destroying particles to improve the efficiency and accuracy of their original method. However, only laminar flows have been computed with this method so far.

1.3.4 Experimental studies

In addition to the numerical studies, many experimental works have studied turbulent drag reduction by polymer additives since its first discovery by Toms (1948). Virk *et al.* (1967) were the first to demonstrate in a turbulent pipe flow the existence of a maximum drag reduction asymptote which is independent of polymer type and pipe diameter. They also determined that the onset of drag reduction occurs at a well-defined wall shear stress. Also for pipe flow, Achia and Thompson (1977) and Oldaker and Tiederman (1977) studied the effect of polymer additives on the near-wall turbulent structures and found that the addition of drag-reducing polymers suppresses the formation of streaks and the eruption of bursts. A recent experiment in pipe flow was performed by Ptasinski *et al.* (2001) who used laser-Doppler velocimetry (LDV) to measure turbulence statistics and the components of the total shear stress. They observed a thickening of the buffer layer and an increase in the slope of the logarithmic profile of the mean velocity. While the Reynolds stress is drastically reduced, it remains non-zero and an important contribution to the total shear stress comes from the polymer stress.

Luchik and Tiederman (1988) used LDV to measure velocity components in a drag-reduced channel flow. They observed a damping of the velocity fluctuations normal to the wall in the buffer region, an increase in average time between the so called bursts and an increase of the mean streak spacing. In a later work, Harder and Tiederman (1991) observed a reduction of the Reynolds shear stress, but the presence of the added polymer stress was only found at higher concentrations. In a different study, Warholic *et al.* (1999) observed approximatively zero Reynolds shear stresses in regimes close to maximum drag reduction over the whole cross section of the channel, but with an added polymer stress, contradicting the previous results. In subsequent work, Warholic *et al.* (2001) confirmed the

existence of a turbulent flow with zero Reynolds shear stress at maximum drag reduction using particle-image velocimetry (PIV). Many studies in channel flows have been mainly concentrated on cases with a homogeneous distribution of polymers, i.e., an ocean of polymer flowing through the channel. These flowfields are not practical, as applications involving external flows often use polymer solutions injected through the wall. Walker and Tiederman (1990) investigated the role of polymer this injection. They observed a general increase in the streamwise velocity fluctuations and an initial increase in the wall-normal velocity fluctuations and Reynolds shear stress due to the injection. However, the action of the polymer solution subsequently reduced the wall-normal velocity fluctuations and Reynolds shear stress significantly below the levels present in a Newtonian flow

Several studies have considered polymer drag reduction in turbulent boundary layers. Fontaine *et al.* (1972) combined LDV and concentration profile measurements by laser-induced-fluorescence techniques. They observed an immediate deceleration of the flow near the wall and a dramatic decrease of the vertical velocity fluctuations and Reynolds shear stress. These effects substantially relax with increasing streamwise distance from the injection slot, becoming similar to the effects observed for dilute homogeneous polymer flows. Petrie and Fontaine (1996) compared the effects of homogeneous drag-reducing polymer solutions using slot-injection. While effects of the homogeneous polymer are noticeable across the boundary layer, effects of injected-polymer are restricted to the near-wall region. Despite these differences, modifications of the near-wall region and the amount of drag reduction appear similar in both cases. These findings were confirmed by White *et al.* (2004) who performed PIV measurements in a turbulent boundary layer with polymer injection. They found a significant modification of the near-wall structure of turbulence, with a coarsening of the low-speed velocity streaks and a reduction in the number and intensity of near-wall vortical structures. They demonstrated, using planar laser-induced-fluorescence (PLIF), that polymers in the near-wall region are responsible for drag reduction (Somandepalli *et al.*, 2003; White *et al.*, 2005) and decomposed the friction drag into four dynamical contributions, following Fukagata *et al.* (2002). They also showed that polymer drag reduction is achieved by either an attenuation of the Reynolds stress or a reduction in the total stress gradient near the wall, or some combination of the two. Somandepalli *et al.* (2005) investigated the streamwise evolution of drag reduction in a turbulent boundary layer and observed three distinct regions: development, sustenance and depletion of drag reduction downstream of the additional injection, suggesting that injection in a fully turbulent flow

might be beneficial in maintaining a longer drag reduction region. Petrie *et al.* (2003) studied the effect of surface roughness on polymer drag reduction in a zero-pressure gradient flat-plate boundary layer, comparing both slot-injected polymers and a homogeneous polymer ocean. They observed that higher polymer concentration is required as roughness increases to achieve the same drag reduction, but for injection, the percentage of drag reduction on rough surfaces is often substantially larger than on smooth plates.

1.4 Objectives

Despite much progress made to elucidate the mechanisms of turbulent drag reduction by polymer additives, there are still many open questions remaining. A fundamental understanding of these mechanisms is required in order to develop predictive tools for practical applications. Moreover, direct numerical simulations are still limited by numerical issues, such as the need for artificial diffusion. The first objective of this work is to deepen the current knowledge of polymer stretching mechanisms in turbulent flows using accurate polymer models and Brownian dynamics. The second objective is to develop new numerical techniques to take advantage of the Lagrangian framework in order to overcome the numerical difficulties encountered by the traditional DNS methods used to simulate viscoelastic flows.

1.5 Thesis organization

Following the introduction presented in this chapter, the models and equations used to simulate viscoelastic flows are derived and described in chapter 2. Chapter 3 presents the numerical implementation chosen to solve those equations. Issues related to the advection of polymers are discussed from both the Eulerian and Lagrangian perspectives. In chapter 4, the numerical methods are validated in model problems, e.g., the inception of steady flows or the Taylor vortex cells. Results for the uncoupled simulations are presented in chapter 5. First, the different models are compared in a turbulent channel flow. Then the topological methodology and conditional statistics are introduced in order to elucidate the mechanisms of polymer stretching in both Newtonian and viscoelastic flows. Chapter 6 introduces the Lagrangian coupled simulations and compares both the Eulerian and Lagrangian approaches. The interaction between the polymer molecules and the turbulence structures is discussed and a mechanism for turbulent drag reduction by polymer additives is

proposed. Finally, the results are summarized in chapter 7, which also contains suggestions for future work.

1.6 Accomplishments

The following list summarizes the important contributions of this work:

- Development of a computer code using distributed-memory parallelism combining Eulerian flow calculation and Lagrangian particle tracking.
- Implementation of various polymer models in the particle tracking code.
- Development of an algorithm to transfer polymer information between Lagrangian and Eulerian frameworks.
- Demonstration of the qualitative similarities of different polymer models in turbulent flow.
- Identification of biaxial extensional flow as main contributor to polymer stretching.
- Identification of rotational flow as characteristic flow type during the polymer relaxation.
- First Lagrangian simulation of turbulent drag reduction.
- Identification of large discrepancies between Eulerian and Lagrangian simulations.
- Identification of the nonlinear advection term as the source of discrepancy due to the creation of small scales.
- Demonstration of better agreement between Eulerian and Lagrangian simulations in drag-reduced flows.

Chapter 2

Description of the models

The classical Navier-Stokes equations are extended to account for the additional stress created by the polymer molecules which needs to be modeled. This chapter will present the origin and derivation of different models used to represent the action of the polymers, followed by the incorporation of these models into the Navier-Stokes equations.

The section treating the polymer models is not intended to be exhaustive but aims at giving an overview of the different models often used and a brief esquisse of their derivation. For a more complete treatment of their derivation and implied assumptions, the reader is refered to the book by Bird *et al.* (1987). In general, each model relies on a force balance for a single molecule in its specific configuration and leads to an expression for the polymer stress tensor. One usually is interested in the average stress over all configurations, which requires the average to be taken over a large number of realizations. This technique is called Brownian dynamics. In some cases it is possible to derive directly an expression for the average stress and in some other cases a closure approximation is required to obtain the constitutive equation. Both the Brownian dynamics and the constitutive equation approaches are used. The former is computationally much more expensive since a large number of realizations is needed to obtain a converged average value, but it allows the use of much more accurate models. The latter is much cheaper but subject to some closure approximations.

The incorporation of these models into the Navier-Stokes equations can follow two different paths. While the Navier-Stokes equations themselves are cast in an Eulerian frame, the computation of the polymer stress through the aforementioned models can either be done in the same Eulerian frame or in a Lagrangian frame, for which a particle tracking

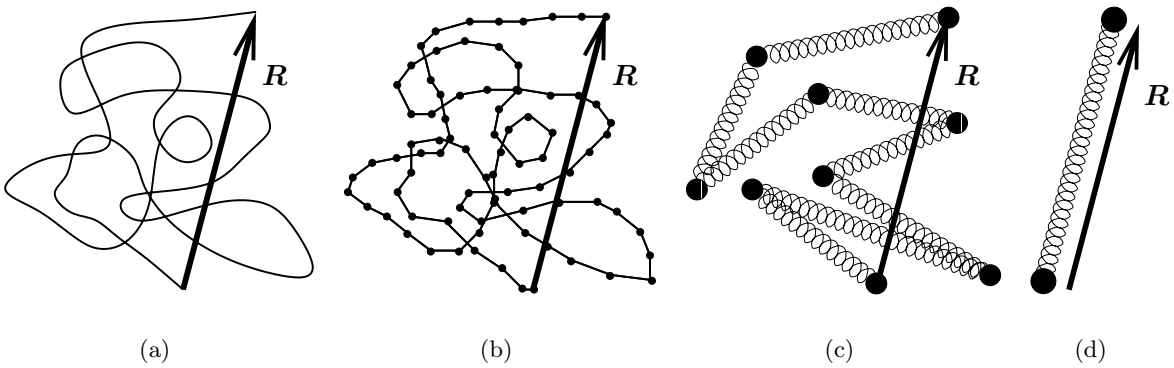

Figure 2.1: Coarse graining; (a) polymer chain, (b) bead-rod chain, (c) bead-spring chain, (d) dumbbell.

algorithm is needed. This work focuses mainly on the Lagrangian approach but both will be described in section 3.4.

2.1 Polymer models and Brownian Dynamics

A polymer molecule consists of long sequences of identical chemical units called monomers. Typical polymers used for drag reduction are linear macromolecules such as polystyrene or polyethylene. Since these macromolecules are in general very flexible, they permit rotational motions of one bond about another, so that a large number of configurations is accessible.

Because the polymer molecules in solutions are long and flexible, they can be easily distorted and stretched by the flow (see Fig. 2.1 (a)). Therefore, polymeric liquids often demonstrate strong viscoelastic properties.

2.1.1 A large range of scales

While the polymer molecules are much larger than the solvent molecules they are also much smaller that the smallest scale found in a turbulent flow, i.e. the viscous or Kolmogorov scale. Therefore, in order to simulate turbulent flows of such solutions, continuum/mesoscopic simulations are used. The derivation of micro-structural models is based on the coarse graining from an atomistic level to a mesoscopic level. The first level corresponds to the bead-rod description (see Fig. 2.1 (b)) which consists of N_K beads of mass m and friction coefficient ζ connected by $N_K - 1$ rigid rods of length b_K. The beads serve as

interaction points with the solvent and the massless rods act as rigid constraints in the chain that keep every bead at a constant distance b_K away from its neighboring beads. b_K is often referred as a Kuhn length while N_K is the number of Kuhn steps, giving a contour length of $L = (N_K - 1)b_K$. Further coarse graining leads to the bead-spring chain description (see Fig. 2.1 (c)) which assumes that a number of bead-rods can be replaced by an entropic spring. Finally, in the most coarse-grained approximation, the internal structure of the chain is neglected and the whole molecule is represented by a single dumbbell (Hermans, 1943; Fraenkel, 1952) with an entropic spring (see Fig. 2.1 (d)).

2.1.2 The freely jointed bead-rod chain model

In the freely jointed bead-rod chain model, or Kramer's chain (Kramers, 1944), the configuration distribution is represented by a random walk; that is, the polar angles θ_i and ϕ_i for the ith link in the chain are completely random and independent of the previous and next link. The probability of finding the ith link in a small range around θ_i and ϕ_i is then given by

$$\psi_{i,\mathrm{eq}}(\theta_i, \phi_i)\mathrm{d}\theta_i\mathrm{d}\phi_i = \frac{1}{4\pi}\sin\theta_i\mathrm{d}\theta_i\mathrm{d}\phi_i, \tag{2.1}$$

and the configurational distribution function for the entire chain at equilibrium by

$$\psi_{\mathrm{eq}}(\theta^{N_K-1}, \phi^{N_K-1}) = \left(\frac{1}{4\pi}\right)^{N_K-1}\prod_{i=1}^{N_K-1}\sin\theta_i. \tag{2.2}$$

The probability distribution function of the end-to-end vector $\boldsymbol{R}$ is then

$$P_{\mathrm{eq}}(\boldsymbol{R}) = \int\int\delta\left(\boldsymbol{R} - b_K\sum_i \boldsymbol{u}_i\right)\psi_{\mathrm{eq}}\mathrm{d}\theta^{N_K-1}\mathrm{d}\phi^{N_K-1}, \tag{2.3}$$

where δ is the delta function and $\boldsymbol{u}_i$, the unit vector in the direction of the ith link. Now, if N_K is large and the end-to-end distance is smaller than about $0.5L$, one can approximate the previous expression by

$$P_{\mathrm{eq}}(\boldsymbol{R}) = \left(\frac{3}{2\pi(N_K-1)b_K^2}\right)^{3/2}\mathrm{e}^{-3R^2/2(N_K-1)b_K^2}. \tag{2.4}$$

This is known as the Gaussian distribution for the end-to-end vector of the freely jointed chain. Therefore, one obtains for the equilibrium mean-square end-to-end distance $\langle R^2\rangle_0$ of

the molecule

$$\begin{aligned}\langle R^2\rangle_{\mathrm{eq}} &= \int R^2 P_{\mathrm{eq}}(\boldsymbol{R})\mathrm{d}\boldsymbol{R} \\ &= \int_0^{2\pi}\int_0^{\pi}\int_0^{\infty} R^2\left(\frac{3}{2\pi(N_K-1)b_K^2}\right)^{3/2} \mathrm{e}^{-3R^2/2(N_K-1)b_K^2} R^2\sin\theta\mathrm{d}r\mathrm{d}\theta\mathrm{d}\phi \\ &= Lb_K = (N_K-1)b_K^2.\end{aligned} \tag{2.5}$$

The average tension $\boldsymbol{F}^{(c)}$ in the polymer chain at constant temperature T is given by the change in the Helmholtz free energy A

$$\boldsymbol{F}^{(c)} = \frac{\partial A}{\partial \boldsymbol{R}}. \tag{2.6}$$

At equilibrium at temperature T, the free energy is given as

$$A = U - TS = -kT\ln\Omega, \tag{2.7}$$

where U is the internal energy, S the entropy, k the Boltzmann constant and Ω is the partition function which is proportional to the configuration distribution function P_{eq}. Hence, the Helmholtz free energy of the polymer chain with end-to-end vector $\boldsymbol{R}$ is

$$A(\boldsymbol{R}) = A^{(0)} - kT\ln P_{\mathrm{eq}}(\boldsymbol{R}). \tag{2.8}$$

Therefore, the average tension in a polymer chain for large values of N_K and for $|\boldsymbol{R}| < 1/2L$ is

$$\boldsymbol{F}^{(c)}(\boldsymbol{R}) = \frac{3kT}{(N_K-1)b_K^2}\boldsymbol{R} = H\boldsymbol{R}, \tag{2.9}$$

which corresponds to a linear spring force law with $H = 3kT/(N_K-1)b_K^2$ as the Hookean spring constant. As stated above, this is only valid for small extensions. In reality, the spring must stiffen with increasing extension. Some more realistic force laws have been proposed:

- Inverse Langevin Force Law (Treloar, 1975):

$$F^{(c)}(R) = \frac{kT}{a}\mathcal{L}^{-1}\left[\frac{R}{(N_K-1)b_K}\right], \tag{2.10}$$

  where $\mathcal{L}(x) = (\coth x) - x^{-1}$.

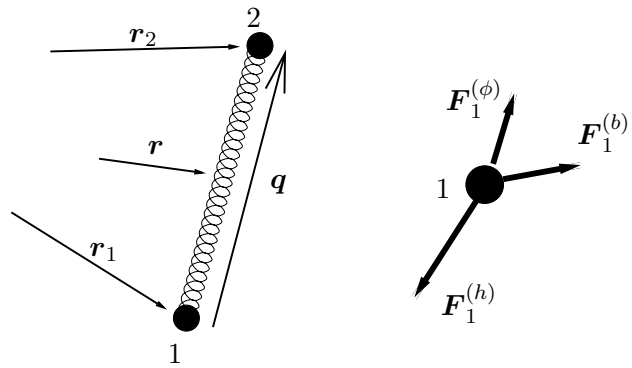

Figure 2.2: Elastic dumbbell

- Warner Force Law (Warner, 1972):

$$F^{(c)}(R) = \frac{3kTR/(N_K-1)b_K^2}{[1-(R/(N_K-1)b_K)^2]}. \tag{2.11}$$

Note that both laws give an infinite force in the limit of when the magnitude of the end-to-end vector tends to its maximum value, $(N_K-1)b_K$.

2.1.3 The general dumbbell model

A dumbbell model idealizes the polymer molecule as a spring dumbbell (Fraenkel, 1952; Hermans, 1943), i.e., two beads, each of mass m, joined by a non bendable spring as illustrated in Fig. 2.2. It is a very crude representation of a polymer molecule and does not have any internal degrees of freedom. Nonetheless, it is orientable and stretchable and can therefore reproduce many of the rheological properties of dilute solutions of polymers. Each dumbbell model is then characterized by a specific spring force law.

Equations of motion

Each bead is presumed to experience the following three forces (see Fig. 2.2):

- the *hydrodynamic drag force* $\boldsymbol{F}^{(h)}$ representing the drag experienced by the bead as it moves through the solute;
- the *Brownian force* $\boldsymbol{F}^{(b)}$ due to the thermal fluctuations in the solution;
- the *entropic force* or *spring force* $\boldsymbol{F}^{(\phi)}$ which tends to bring the polymer molecule back into a coiled configuration.

With the assumption that the inertial term can be neglected, the equation of motion for each bead becomes a simple force balance:

$$\boldsymbol{F}_\nu^{(h)} + \boldsymbol{F}_\nu^{(b)} + \boldsymbol{F}_\nu^{(\phi)} = \boldsymbol{0} \qquad (\nu = 1, 2). \tag{2.12}$$

The hydrodynamic drag force is proportional to the difference between the bead velocity $\dot{\boldsymbol{r}}_\nu$ and the velocity $\boldsymbol{u}(\boldsymbol{r}_\nu)$ of the solution at bead ν:

$$\boldsymbol{F}_\nu^{(h)} = \zeta(\boldsymbol{u}(\boldsymbol{r}_\nu) - \dot{\boldsymbol{r}}_\nu), \tag{2.13}$$

where ζ is the friction coefficient. Moreover, it is assumed that the flow field is homogeneous, i.e., the velocity gradients do not change appreciably over a distance comparable to the size of the polymer molecule. Therefore, the local velocity can be written as

$$\boldsymbol{u}(\boldsymbol{r}_\nu) = \boldsymbol{u} \pm \nabla\boldsymbol{u} \cdot \frac{\boldsymbol{q}}{2}, \tag{2.14}$$

where $\boldsymbol{u}$ and $\nabla\boldsymbol{u}$ are the velocity, and velocity gradient tensor at the location of the center of mass of the polymer molecule and $\boldsymbol{q} = \boldsymbol{r}_1 - \boldsymbol{r}_2$ is the end-to-end vector.

After some non-trivial algebra, the contribution of the Brownian motion can be written in the form $\boldsymbol{F}_\nu^{(b)} = -kT(\partial \ln\Psi/\partial\boldsymbol{q}_\nu)$ where the configuration-space distribution function $\Psi(\boldsymbol{r}_1, \boldsymbol{r}_2, t) = n\psi(\boldsymbol{q}, t)$.

Finally the spring force $\boldsymbol{F}^{(\phi)}$ resulting from the intra-molecular potential is given by

$$\boldsymbol{F}_\nu^{(\phi)} = -\frac{\partial}{\partial\boldsymbol{r}_\nu}\phi, \tag{2.15}$$

which is equal and opposite for each bead. Therefore, we can define a new connector force $\boldsymbol{F}^{(c)} = \boldsymbol{F}_1^{(\phi)} = -\boldsymbol{F}_2^{(\phi)}$.

By adding and subtracting the equation of motion (2.12) for each bead, one gets an equation of motion for the center of mass $\boldsymbol{r} = (\boldsymbol{r}_1 + \boldsymbol{r}_2)/2$ and one for the dumbbell connector vector $\boldsymbol{q}$:

$$\boxed{\begin{aligned} \frac{\mathrm{d}\boldsymbol{r}}{\mathrm{d}t} &= \boldsymbol{u}, \\ \frac{\mathrm{d}\boldsymbol{q}}{\mathrm{d}t} &= \nabla\boldsymbol{u} \cdot \boldsymbol{q} - \frac{2kT}{\zeta}\frac{\partial}{\partial\boldsymbol{q}}\ln\psi - \frac{2}{\zeta}\boldsymbol{F}^{(c)}, \end{aligned}} \tag{2.16}$$

where the diffusion of the center of mass of the polymer molecule has been neglected.

Constitutive equation

The time-evolution of the probability density $\psi(\boldsymbol{q}, t)$ is given by the Fokker-Planck

$$\frac{\partial \psi}{\partial t} = -\frac{\partial}{\partial \boldsymbol{q}}(\dot{\boldsymbol{q}}\psi), \tag{2.17}$$

which becomes using Eq. (2.16)

$$\frac{\partial \psi}{\partial t} + \left(\nabla \boldsymbol{u} \cdot \boldsymbol{q}\frac{\partial}{\partial \boldsymbol{q}}\psi\right) = \frac{2kT}{\zeta}\left(\frac{\partial}{\partial \boldsymbol{q}}\frac{\partial}{\partial \boldsymbol{q}}\psi\right) + \frac{2}{\zeta}\left(\frac{\partial}{\partial \boldsymbol{q}}\boldsymbol{F}^{(c)}\psi\right). \tag{2.18}$$

Multiplying Eq. (2.18) with any function $\chi(\boldsymbol{q})$ and integrating over all the configuration space leads to an equation for $\langle\chi\rangle = \int \chi(\boldsymbol{q})\psi(\boldsymbol{q})\mathrm{d}q^3$. In particular, if $\chi(\boldsymbol{q}) = \boldsymbol{q}\boldsymbol{q}$, the equation of change for the configuration tensor $\langle\boldsymbol{q}\boldsymbol{q}\rangle$ becomes

$$\boxed{\frac{\mathrm{d}}{\mathrm{d}t}\langle\boldsymbol{q}\boldsymbol{q}\rangle - \nabla\boldsymbol{u}\cdot\langle\boldsymbol{q}\boldsymbol{q}\rangle - \langle\boldsymbol{q}\boldsymbol{q}\rangle\cdot\nabla\boldsymbol{u}^{\dagger} = \frac{4kT}{\zeta}\boldsymbol{\delta} - \frac{4}{\zeta}\langle\boldsymbol{q}\boldsymbol{F}^{(c)}\rangle,} \tag{2.19}$$

where $\boldsymbol{\delta}$ is the identity matrix and † represents the transpose. If the system is at equilibrium, i.e., no flow, Eq. (2.19) gives

$$\langle\boldsymbol{q}\boldsymbol{F}^{(c)}\rangle_{\mathrm{eq}} = kT\boldsymbol{\delta}. \tag{2.20}$$

Stress tensor

The total stress tensor of a polymer solution is assumed to be the sum of a contribution from the solvent and another resulting from the presence of polymer molecules

$$\boldsymbol{\sigma} = \boldsymbol{\sigma}_s + \boldsymbol{\sigma}_p \tag{2.21}$$

$$= (p_s\boldsymbol{\delta} + \boldsymbol{\tau}_s) + (p_p\boldsymbol{\delta} + \boldsymbol{\tau}_p) \tag{2.22}$$

$$= p\boldsymbol{\delta} + \boldsymbol{\tau}, \tag{2.23}$$

where $p = p_s + p_p$ is the isotropic pressure, $\boldsymbol{\tau} = \boldsymbol{\tau}_s + \boldsymbol{\tau}_p$ is the part of the total stress tensor which is zero at equilibrium and $\boldsymbol{\delta}$ is the identity matrix.

If one assumes a Maxwellian velocity distribution, Kramers' (Kramers, 1944) form for

the polymeric stress tensor is obtained

$$\boxed{\begin{aligned}\boldsymbol{\sigma}_p &= n\langle \boldsymbol{q}\boldsymbol{F}^{(c)}\rangle - 2nkT\boldsymbol{\delta},\\ \boldsymbol{\tau}_p &= n\langle \boldsymbol{q}\boldsymbol{F}^{(c)}\rangle - nkT\boldsymbol{\delta},\end{aligned}} \tag{2.24}$$

where n is the number of dumbbells per unit volume. The stress is composed of the contribution from the intermolecular potential and the contribution due to the Brownian motion.

Brownian Dynamics

In a Brownian dynamics simulation (Bird and Wiest, 1995; Laso and Oettinger, 1993), the Brownian force $\boldsymbol{F}^{(b)}$ is represented by a random variable with the following properties

$$\langle F_i^{(b)}\rangle = 0, \tag{2.25}$$

$$\langle F_i^{(b)}(t)F_j^{(b)}(t+\mathrm{d}t)\rangle = 2kT\zeta\delta_{ij}\delta_D(\mathrm{d}t) \approx \frac{2kT\zeta\delta_{ij}}{\mathrm{d}t}, \tag{2.26}$$

where $delta_D(x)$ is the Dirac delta function. If one uses a Hookean spring law (see Eq. 2.9) and introduces the 3-dimensional Wiener process $\hat{\boldsymbol{W}}$, Eq. (2.16) can be written as:

$$\boxed{\mathrm{d}\boldsymbol{q} = \left(\nabla\boldsymbol{u}\cdot\boldsymbol{q} - \frac{2}{\zeta}H\boldsymbol{q}\right)\mathrm{d}t - \sqrt{\frac{2kT}{\zeta}}\mathrm{d}\hat{\boldsymbol{W}}_t,} \tag{2.27}$$

where the increment $\mathrm{d}\hat{\boldsymbol{W}}_t = \hat{\boldsymbol{W}}_{t+\mathrm{d}t} - \hat{\boldsymbol{W}}_t$ is a Gaussian random variable with zero mean and variance $\mathrm{d}t$ and is independent of any other increment.

To determine the stress tensor as defined in Eq. (2.24) requires an average over all possible configurations of the end-to-end vector $\boldsymbol{q}$. Therefore, many realizations must be computed from Eq. (2.27) in order to obtain good statistics.

2.1.4 The Oldroyd-B model

The Oldroyd-B model is characterized by a linear or Hookean force law as found in Eq. (2.9). Therefore, it is also limited by the same assumptions as those of Section 2.1.2.

Non-dimensionalization

One can introduce the dimensionless end-to-end vector $\hat{\boldsymbol{q}} = \sqrt{\frac{H}{kT}}\boldsymbol{q}$. Moreover, since two different time scales are present, i.e., the flow and the polymer time scales, it is possible to use two different dimensionless times t^f and $t^p = t/\lambda_H$, where $\lambda_H = \zeta/4H$ is the longest relaxation time of the polymer molecule. The superscript ^{f} and ^{p} denote quantities non-dimensionalized by the flow and polymer times respectively. The two times are related to each other by the Weissenberg number $Wi = \frac{t^f}{t^p}$. The dimensionless stress depends also on the time scale chosen for the non-dimensionalization:

$$\boldsymbol{\tau}_p^p = \frac{\boldsymbol{\tau}_p}{nkT}, \qquad \boldsymbol{\tau}_p^f = \frac{1}{Wi}\boldsymbol{\tau}_p^p.$$

Equations

With these new definitions, Eq. (2.16) becomes

$$\frac{\mathrm{d}\hat{\boldsymbol{q}}}{\mathrm{d}t^p} = Wi \cdot \nabla \boldsymbol{u}^f \cdot \hat{\boldsymbol{q}} - \frac{1}{2}\hat{\boldsymbol{q}} - \frac{1}{2}\frac{\partial}{\partial \hat{\boldsymbol{q}}}\ln\psi, \tag{2.28}$$

and Eq. (2.27)

$$\boxed{\begin{aligned} &\mathrm{d}\hat{\boldsymbol{q}} = \left(Wi \cdot \nabla \boldsymbol{u}^f \cdot \hat{\boldsymbol{q}} - \frac{1}{2}\hat{\boldsymbol{q}}\right)\mathrm{d}t^p - \sqrt{\frac{1}{2}}\mathrm{d}\hat{\boldsymbol{W}}_{t^p} \\ &\text{or} \\ &\mathrm{d}\hat{\boldsymbol{q}} = \left(\nabla \boldsymbol{u}^f \cdot \hat{\boldsymbol{q}} - \frac{1}{2\,Wi}\hat{\boldsymbol{q}}\right)\mathrm{d}t^f - \sqrt{\frac{1}{2\,Wi}}\mathrm{d}\hat{\boldsymbol{W}}_{t^f}. \end{aligned}} \tag{2.29}$$

The polymeric stress tensor can then be written as

$$\hat{\boldsymbol{\tau}}_p = \langle \hat{\boldsymbol{q}}\hat{\boldsymbol{q}} \rangle - \boldsymbol{\delta}, \tag{2.30}$$

and combined with Eq. (2.19), it leads to a constitutive equation for the polymeric stress (Larson, 1999):

$$\boxed{\frac{\mathrm{d}}{\mathrm{d}t^f}\boldsymbol{\tau}_p^f - \nabla \boldsymbol{u}^f \cdot \boldsymbol{\tau}_p^f - \boldsymbol{\tau}_p^f \cdot \nabla \boldsymbol{u}^{f\dagger} + \frac{1}{Wi}\left(\boldsymbol{\tau}_p^f - \boldsymbol{\delta}\right) = 0.} \tag{2.31}$$

The closed form of the constitutive equation is only possible because of the linearity of the force law implied by the Oldroyd-B model. However, as it was mentioned earlier, such a

spring law is only valid for smaller extensions since the model permits infinite extension which leads to an unphysical behavior at large extensions.

2.1.5 The FENE dumbbell model

To overcome this aforementioned problem, other spring force laws have been proposed as was already mentioned in section 2.1.2. In particular, the Warner force law was used to approximate the Inverse Langevin function (see Eq. (2.10-2.11))

$$\boldsymbol{F}^{(c)} = \frac{H\boldsymbol{q}}{1 - q^2/q_0^2}, \tag{2.32}$$

where the extensibility parameter q_0 determines the maximum extension of the polymer molecule (Peterlin, 1961). For small extensions, Eq. (2.32) exhibits the expected linear behavior of the Hookean spring and a finite length q_0 in the limit of an infinite force. Springs obeying this force law are often called FENE (Finitely Extensible Nonlinear Elastic) springs. If one introduces the Warner force law with the dimensionless extensibility parameter $b = Hq_0^2/kT$ into Eq. (2.29), the FENE dumbbell model is obtained:

$$\boxed{\mathrm{d}\hat{\boldsymbol{q}} = \left(\nabla \boldsymbol{u}^f \cdot \hat{\boldsymbol{q}} - \frac{\hat{\boldsymbol{q}}}{2\,Wi\left(1 - \frac{\hat{q}^2}{b}\right)}\right)\mathrm{d}t^f - \sqrt{\frac{1}{2\,Wi}}\mathrm{d}\hat{\boldsymbol{W}}_{t^f}.} \tag{2.33}$$

The calculation of the stress must be modified accordingly

$$\boldsymbol{\tau}_p^f = \frac{1}{Wi}\left\langle \frac{\boldsymbol{q}\boldsymbol{q}}{1 - \hat{q}^2/b} - \boldsymbol{\delta}\right\rangle. \tag{2.34}$$

2.1.6 FENE-P

For a nonlinear force law like the FENE spring, one cannot define a closed constitutive equation as derived for the Hookean spring in section 2.1.3, since the term $\langle \boldsymbol{q}\boldsymbol{F}^{(c)}\rangle$ in Eq. (2.19) cannot be expressed directly as a function of $\langle \boldsymbol{q}\boldsymbol{q}\rangle$. However, if one approximates the configuration-dependent nonlinear factor in the FENE spring force by a self-consistently averaged term called the FENE-P spring force, Eq. (2.19) can be closed and reads in the

its non-dimensional form

$$\boxed{\frac{\mathrm{d}}{\mathrm{d}t^f}\langle\hat{\boldsymbol{q}}\hat{\boldsymbol{q}}\rangle = \nabla\boldsymbol{u}^f\cdot\langle\hat{\boldsymbol{q}}\hat{\boldsymbol{q}}\rangle + \langle\hat{\boldsymbol{q}}\hat{\boldsymbol{q}}\rangle\cdot\nabla\boldsymbol{u}^{f\dagger} - \frac{1}{Wi}\left(\frac{\langle\hat{\boldsymbol{q}}\hat{\boldsymbol{q}}\rangle}{1-\mathrm{tr}\langle\hat{\boldsymbol{q}}\hat{\boldsymbol{q}}\rangle/b} - \boldsymbol{\delta}\right),} \tag{2.35}$$

where $\mathrm{tr}\langle\hat{\boldsymbol{q}}\hat{\boldsymbol{q}}\rangle$ is the trace of the configuration tensor $\langle\hat{\boldsymbol{q}}\hat{\boldsymbol{q}}\rangle$.

2.1.7 Brownian FENE-P

The Brownian FENE-P is a combination of the FENE and FENE-P models. It relies on Eq. (2.33) where the term $\hat{q}^2$ of the spring force is replaced by the trace of the conformation tensor $\langle\hat{\boldsymbol{q}}\hat{\boldsymbol{q}}\rangle$ from Eq. (2.35):

$$\boxed{\mathrm{d}\hat{\boldsymbol{q}} = \left(\nabla\boldsymbol{u}^f\cdot\hat{\boldsymbol{q}} - \frac{\hat{\boldsymbol{q}}}{2\,Wi\,(1-\mathrm{tr}\langle\hat{\boldsymbol{q}}\hat{\boldsymbol{q}}\rangle/b)}\right)\mathrm{d}t^f - \sqrt{\frac{1}{2\,Wi}}\mathrm{d}\hat{\boldsymbol{W}}_{t^f}.} \tag{2.36}$$

Since the spring force is computed from the average conformation, some realizations can exceed the maximum extension.

2.1.8 The bead-spring chain models

The dumbbell model is oversimplified since it accounts for polymer-solvent interaction only at two points. It is therefore natural to consider a more realistic model which contains N_s+1 beads and N_s corresponding springs (see Fig. 2.1 *c*). The derivation of the equations of motion for the bead-spring chain model are a simple generalization of the equations derived in section 2.1.3. With similar assumptions, a force balance leads to the equation for the center of mass of the molecule and the equations for each connecting vector $\boldsymbol{q}_\nu$ between beads ν and $\nu+1$:

$$\frac{\mathrm{d}\boldsymbol{r}}{\mathrm{d}t} = \boldsymbol{u}, \tag{2.37}$$

$$\frac{\mathrm{d}\boldsymbol{q}_\nu}{\mathrm{d}t} = \nabla\boldsymbol{u}\cdot\boldsymbol{q}_\nu - \frac{1}{\zeta}\sum_{k=1}^{N_s}A_{\nu k}\left(kT\frac{\partial}{\partial\boldsymbol{q}_k}\ln\psi + \boldsymbol{F}_k^{(c)}\right), \tag{2.38}$$

where $A_{\nu k}$ are the elements of the Rouse matrix defined as

$$A_{ij} = \begin{cases} 2 & \text{if } i = j, \\ -1 & \text{if } i = j \pm 1, \qquad i, j = 1, ..., N_s \\ 0 & \text{otherwise.} \end{cases} \tag{2.39}$$

The diffusion equation corresponding to Eq. (2.18) becomes

$$\frac{\partial \psi}{\partial t} = -\sum_{\nu=1}^{N_s} \frac{\partial}{\partial \boldsymbol{q}_\nu} \left((\nabla \boldsymbol{u} \cdot \boldsymbol{q}_\nu)\psi - \frac{1}{\zeta} \sum_{k=1}^{N_s} A_{\nu k} \left[kT \frac{\partial}{\partial \boldsymbol{q}_k} \psi + \boldsymbol{F}_k^{(c)} \psi \right] \right), \tag{2.40}$$

which can be used to find $\boldsymbol{\xi} = \left\langle \sum_j \sum_k C_{jk} \boldsymbol{q}_j \boldsymbol{q}_k \right\rangle$ (Hassager and Bird, 1972)

$$\frac{\mathrm{d}\boldsymbol{\xi}}{\mathrm{d}t} - \nabla \boldsymbol{u} \cdot \boldsymbol{\xi} - \boldsymbol{\xi} \cdot \nabla \boldsymbol{u}^\dagger = -\frac{2}{\zeta} \left\langle \sum_k \boldsymbol{F}_k^{(c)} \boldsymbol{q}_k \right\rangle + \frac{2kT}{\zeta} N_s \boldsymbol{\delta}, \tag{2.41}$$

where C_{jk} is the Kramer's matrix

$$C_{jk} = \begin{cases} i(N_s + 1 - j)/(N_s + 1) & \text{if } i \leq j, \\ j(N_s + 1 - i)/(N_s + 1) & \text{if } j \leq i, \qquad i, j = 1, ..., N_s, \end{cases} \tag{2.42}$$

which gives at equilibrium

$$\sum_{k=1}^{N_s} \left\langle \boldsymbol{F}_k^{(c)} \boldsymbol{q}_k \right\rangle_{\text{eq}} = N_s kT \boldsymbol{\delta}. \tag{2.43}$$

In a similar way, we find for the stress tensor

$$\boldsymbol{\tau}_p = n \sum_{k=1}^{N_s} \langle \boldsymbol{q}_k \boldsymbol{F}_k^{(c)} \rangle - n N_s kT \boldsymbol{\delta}. \tag{2.44}$$

The bead-spring chain with Hookean springs

In the case of Hookean springs, the model is called a Rouse chain (Rouse, 1953). Since the model is linear, one can find a constitutive equation for the different stress components

$$\boldsymbol{\tau}_p^f = \sum_{k=1}^{N_s} \boldsymbol{\tau}_{pk}^f, \tag{2.45}$$

where each normal-mode stress contribution satisfies

$$\frac{\mathrm{d}}{\mathrm{d}t^f}\boldsymbol{\tau}_{pk}^f - \nabla\boldsymbol{u}^f\cdot\boldsymbol{\tau}_{pk}^f - \boldsymbol{\tau}_{pk}^f\cdot\nabla\boldsymbol{u}^{f\dagger} + \frac{1}{Wi\hat{\lambda}_k}\left(\boldsymbol{\tau}_{pk}^f - \boldsymbol{\delta}\right) = 0. \tag{2.46}$$

The relaxation times λ_k depend on the eigenvalues a_k of the Rouse matrix:

$$\lambda_k = \frac{\zeta/2H}{a_k} = \frac{\zeta/2H}{4\sin^2(k\pi/2(N_s+1))}, \tag{2.47}$$

$$\hat{\lambda}_k = \frac{1}{2\sin^2(k\pi/2(N_s+1))}, \tag{2.48}$$

which reduces, as expected, to the previously derived result of Eq. (2.31) in the dumbbell case since the dimensionless relaxation time $\hat{\lambda} = \hat{\lambda}_1 = 1$.

Moreover, if the hydrodynamic interactions among the various beads in one chain are also included, one finds the Zimm model (Zimm, 1956).

Relaxation time and stress

While there exists only one relaxation time $\lambda = \lambda_H$ for a dumbbell, the bead-spring chain model incorporates internal modes, each associated with a relaxation time. Therefore, it is not obvious which polymer time should be used in the definition of the Weissenberg number, which is the ratio of polymer and flow times. Different relaxation times can be used, i.e., the zero-shear relaxation time, the Rouse relaxation time (see Eq. (2.48)) or the longest relaxation time $\hat{\lambda}$ (Somasi *et al.*, 2002). For all the following results and calculations, the longest relaxation time was chosen, which is the time the slowest relaxation mode takes to recoil from a full extension. It can be computed by examining the long time relaxation of the stress of an ensemble of chains starting with initial configuration in which every chain is fully stretched in the x-direction. $\hat{\lambda}$ is then given by the inverse of the slope of the tangent as illustrated in Fig. 2.3. The longest relaxation time for different parameter values is summarized in table 2.1.

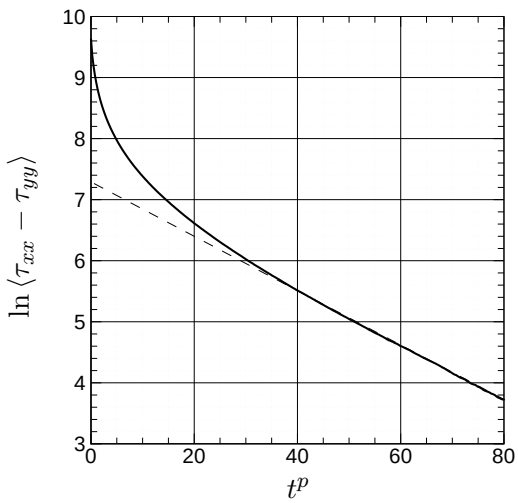

Figure 2.3: Calculation of the longest relaxation time for a FENE chain with $N_s = 10$ and $b = 3600$.

Table 2.1: Longest relaxation times.

$N_s = 10$	$b = 3600$	$\hat{\lambda} = 21.6$
$N_s = 5$	$b = 3600$	$\hat{\lambda} = 7.2$
$N_s = 5$	$b = 10000$	$\hat{\lambda} = 7.4$
$N_s = 5$	$b = 900$	$\hat{\lambda} = 6.66$

The bead-spring chain with FENE springs

With a nonlinear spring force, one gets the FENE multi-chain model which reads in its Brownian dynamics form:

$$\boxed{\begin{aligned} \mathrm{d}\hat{\boldsymbol{q}}_\nu = &\left(\nabla \boldsymbol{u}^f \cdot \hat{\boldsymbol{q}}_\nu - \frac{1}{4}\sum_{k=\nu-1}^{\nu+1} A_{\nu k} \frac{\hat{\boldsymbol{q}}_k}{Wi\hat{\lambda}\left(1-\frac{\hat{q}_k^2}{b_s}\right)}\right)\mathrm{d}t^f \\ &+\sqrt{\frac{1}{2\,Wi\hat{\lambda}}}\left(\mathrm{d}\hat{\boldsymbol{W}}_{t^f}^{\nu+1} - \mathrm{d}\hat{\boldsymbol{W}}_{t^f}^{\nu}\right), \qquad \nu = 1...N_s \end{aligned}} \tag{2.49}$$

where $\hat{\lambda}$ is the longest relaxation time and b_s corresponds to the individual maximum extension parameter of each spring. It is related to the the maximum extension of a FENE dumbbell through:

$$b_s = \frac{b}{N_s} = \frac{H_s Q_0^2}{N_s kT}, \tag{2.50}$$

where $H_s = HN_s$.

2.2 Turbulent flow and particle tracking

2.2.1 Modified Navier–Stokes equations

We are interested in the flow of dilute solution of polymers. It is assumed in this work that the polymer concentration is uniform. The polymer effects are modeled via an additional term, the polymer body force, which is the divergence of the polymer stress tensor $\boldsymbol{\tau}_p^f$,

$$\boxed{\frac{\partial \boldsymbol{u}}{\partial t} + \boldsymbol{u}\nabla\boldsymbol{u} = -\nabla p + \frac{\beta}{Re}\nabla^2\boldsymbol{u} + \frac{1-\beta}{Re}\nabla\cdot\boldsymbol{\tau}_P^f,} \tag{2.51}$$

where β is the ratio of the solvent viscosity ν to the total viscosity and consequently depends on the concentration of polymers and $\boldsymbol{\tau}_P$ is the Eulerian polymer stress as opposed to the Lagrangian polymer stress $\boldsymbol{\tau}_p$. Simulations are performed in a minimal channel (Jimenez and Moin, 1991,) at a constant mass flow. The Reynolds number is defined as $Re = U_c h/\nu$, where U_c is the centerline velocity of the corresponding Poiseuille flow and h is the half height of the channel. This non-dimensionalization also defines the flow time scale mentioned in section 2.1.4.

2.2.2 Particle tracking

Most viscoelastic simulations of polymer drag reduction assume that the polymer phase is a continuum and therefore use an Eulerian approach. In that case the time derivative in each constitutive equation for the stress must be regarded as a total time derivative. However, this work adopts the Lagrangian point of view, i.e., single polymer molecules are tracked individually in an Eulerian flow simulation. The first equation of (2.16) governs the evolution of the particle positions. The integration of the polymer molecules trajectories assumes that the molecule center-of-mass motion is characterized by no inertia and an infinite Peclet number. Therefore, these trajectories represent an exact Lagrangian description of the flow. The equation for the position of their center of mass can be rewritten:

$$\boxed{\frac{\mathrm{d}\boldsymbol{x}_p}{\mathrm{d}t} = \boldsymbol{u}_p(\boldsymbol{x}_p),} \tag{2.52}$$

where $\boldsymbol{u}_p$ is the velocity of the polymer molecule at its position $\boldsymbol{x}_p$ which needs to be interpolated from the velocity field given by the Eulerian flow calculation.

Chapter 3

Numerical implementation

Chapter 2 introduced different models which can be used to describe viscoelastic flows of dilute polymer solutions. In addition, it was mentioned that the usual Navier-Stokes equations need to be modified to account for the effect of the polymers. This chapter focuses on the numerical implementation of the aforementioned equations. In the first part, the numerical algorithms for specific polymer models are presented. Although many polymer models have been described previously, this work focuses on three Brownian models, i.e., the FENE and FENE-P dumbbells and the FENE bead-spring chain, and on one constitutive model, the FENE-P.

The numerical implementation used to solve the modified Navier-Stokes equations is discussed in section 3.2, followed by the presentation of the particle tracking algorithm. The chapter concludes with the discussion of the computation of the Eulerian polymer stress in both the Eulerian and Lagrangian frameworks. The related issue of the advection in the Eulerian approach is also mentioned.

3.1 Algorithm for polymer stress

3.1.1 FENE dumbbell model

To advance Eq. (2.33) from time t_n^f to t_{n+1}^f, a second-order semi-implicit predictor-corrector algorithm is used (Oettinger, 1996). The predictor step is explicit, while the corrector step treats the spring force term semi-implicitly.

Predictor step

$$\hat{\boldsymbol{q}}_* = \hat{\boldsymbol{q}}_n + \left(\nabla \hat{\boldsymbol{u}}_n^f \cdot \hat{\boldsymbol{q}}_n - \frac{\hat{\boldsymbol{q}}_n}{2\,Wi\,(1-\hat{q}_n^2/b)}\right) \mathrm{d}t^f - \frac{1}{\sqrt{2\,Wi}} \mathrm{d}\hat{\boldsymbol{W}}_n. \tag{3.1}$$

Corrector step

$$\begin{aligned} &\left(1 + \frac{\mathrm{d}t^f}{4\,Wi\left(1-\hat{q}_{n+1}^2/b\right)}\right) \hat{\boldsymbol{q}}_{n+1} = \hat{\boldsymbol{q}}_n + \\ &\frac{1}{2}\left(\nabla \hat{\boldsymbol{u}}_{n+1}^f \cdot \hat{\boldsymbol{q}}_* + \nabla \hat{\boldsymbol{u}}_n^f \cdot \hat{\boldsymbol{q}}_n - \frac{\hat{\boldsymbol{q}}_n}{2\,Wi\,(1-\hat{q}_n^2/b)}\right) \mathrm{d}t^f - \frac{1}{\sqrt{2\,Wi}} \mathrm{d}\hat{\boldsymbol{W}}_n, \end{aligned} \tag{3.2}$$

where $\mathrm{d}\hat{\boldsymbol{W}}_n$ is a three-dimensional Gaussian random variable with mean zero and variance $\mathrm{d}t^f$. Let's refer to the known right hand side of this equation, $\hat{\boldsymbol{F}}_*$:

$$\left(1 + \frac{\mathrm{d}t^f}{4\,Wi\left(1-\hat{q}_{n+1}^2/b\right)}\right) \hat{\boldsymbol{q}}_{n+1} = \hat{\boldsymbol{F}}_*. \tag{3.3}$$

This equation cannot be directly solved because it is a vector equation and in the left hand side, the norm of the unknown vector is also needed. To avoid this difficulty, we square the equation, where the square of a vector is understood to be the scalar product with itself. Eventually we take the square root and solve for the norm $\hat{q}_{n+1}$.

$$\left(1 + \frac{\mathrm{d}t^f}{4\,Wi\left(1-\hat{q}_{n+1}^2/b\right)}\right) \hat{q}_{n+1} = ||\hat{\boldsymbol{F}}_*|| = \hat{F}_*. \tag{3.4}$$

Rearranging, we get a third order equation

$$\hat{q}_{n+1}^3 - \hat{F}_* \hat{q}_{n+1}^2 - b\left(1 + \frac{\mathrm{d}t^f}{4\,Wi}\right) \hat{q}_{n+1} + \hat{F}_* b = 0, \tag{3.5}$$

for which a closed solution exists. We define $A = -\hat{F}_*$, $B = -b\left(1 - \frac{\mathrm{d}t^f}{4\,Wi}\right)$ and $C = \hat{F}_* b$. We can now rewrite the equation $x^3 + Ax^2 + Bx + C = 0$ into its normal form $y^3 + 3Py + 2Q = 0$ using the transformation $y = x + \frac{A}{3}$. and the coefficients:

$$2Q = \frac{2A^3}{27} - \frac{AB}{3} + C, \qquad 3P = B - \frac{A^2}{3}. \tag{3.6}$$

The discriminant is defined as $D = P^3 + Q^2$, and since the coefficients are all real and both

P and D are negative, we get the solutions:

$$y_1 = -2R\cos\beta, \qquad y_{2,3} = 2R\cos\left(\beta \pm \frac{\pi}{3}\right), \tag{3.7}$$

where $R = (\text{sgn } Q)\sqrt{|P|}$ and $\beta = \frac{1}{3}\arccos(Q/R^3)$.

Using the root $\hat{q}_{n+1}$ in Eq. (3.3) and solving it for the elements of $\hat{\boldsymbol{q}}_{n+1}$, we finally find the end-to-end vector:

$$\hat{\boldsymbol{q}}_{n+1} = \frac{\hat{\boldsymbol{F}}_*}{\left(1 + \frac{\mathrm{d}t^f}{4\,Wi\left(1-\hat{q}_{n+1}^2/b\right)}\right)}. \tag{3.8}$$

Finally the polymer stress is computed with Eq. (2.34) by averaging over many realizations.

3.1.2 FENE-P model

As mentioned in chapter 2, instead of averaging over different realizations, one can also solve directly for a conformation tensor $\langle\hat{\boldsymbol{q}}\hat{\boldsymbol{q}}\rangle$ and therefore obtain an expression for the average stress. Eq. (2.35) for the evolution of this conformation tensor consists of six equations due to the symmetry of the tensor. To integrate these equations, we use an iterative implicit scheme based on the scheme used for the FENE model. The spring force is treated explicitly at each step of the iteration and the stretching term is semi-implicit. The first step computes the trace of the tensor, which is used in the second step to calculate the spring force for each component of the tensor.

In index notation, Eq. (2.35) can be written as

$$\partial_{t^f}\langle\hat{q}_i\hat{q}_j\rangle = \partial_k u_i^f\langle\hat{q}_k\hat{q}_j\rangle + \langle\hat{q}_i\hat{q}_k\rangle\partial_k u_j^f - \frac{1}{Wi}\left(\frac{\langle\hat{q}_i\hat{q}_j\rangle}{1-\langle\hat{q}_i\hat{q}_i\rangle/b} - \delta_{ij}\right), \tag{3.9}$$

where $\partial_{t^f} = \frac{\partial}{\partial t^f}$ and $\partial_k = \frac{\partial}{\partial x_k}$.

Trace of the conformation tensor $\langle\hat{q}_i\hat{q}_j\rangle$

We obtain an equation for the trace by adding the three equations corresponding to $i = j$:

$$\partial_{t^f}\langle\hat{q}_i\hat{q}_i\rangle = \partial_k u_i^f\langle\hat{q}_k\hat{q}_i\rangle + \langle\hat{q}_i\hat{q}_k\rangle\partial_k u_i^f - \frac{1}{Wi}\left(\frac{\langle\hat{q}_i\hat{q}_i\rangle}{1-\langle\hat{q}_i\hat{q}_i\rangle/b} - 3\right) \tag{3.10}$$

and if we define $R_{ij} = \partial_k u_i^f \langle \hat{q}_k \hat{q}_i \rangle + \langle \hat{q}_i \hat{q}_k \rangle \partial_k u_i^f$ to be the stretching term, we get:

$$\partial_{t^f} \langle \hat{q}_i \hat{q}_i \rangle = R_{ii} - \frac{1}{Wi} \left(\frac{\langle \hat{q}_i \hat{q}_i \rangle}{1 - \langle \hat{q}_i \hat{q}_i \rangle / b} - 3 \right). \tag{3.11}$$

We introduce now a new variable, $\chi = 1 - \langle \hat{q}_i \hat{q}_i \rangle / b$, so that the trace becomes $\langle \hat{q}_i \hat{q}_i \rangle = b(1-\chi)$. The equation for the trace can be converted into an equation for the new variable χ:

$$-b \frac{\mathrm{d}\chi}{\mathrm{d}t^f} - R_{ii} + b \frac{1-\chi}{Wi\chi} - \frac{3}{Wi} = 0, \tag{3.12}$$

which can be rewritten as

$$\chi \frac{\mathrm{d}\chi}{\mathrm{d}t^f} + \frac{\chi R_{ii}}{b} + \frac{\chi - 1}{Wi} + \frac{3\chi}{Wib} = 0. \tag{3.13}$$

The time derivative is then discretized at $n+1$

$$\chi \frac{\mathrm{d}\chi}{\mathrm{d}t^f} \approx \frac{\chi_{n+1}^2 - \chi_{n+1}\chi_n}{\mathrm{d}t^f} \tag{3.14}$$

Using this last relation, we obtain a polynomial equation of the second degree

$$\chi_{n+1}^2 + \left[R_{ii,*} \frac{\mathrm{d}t^f}{b} - \chi_n + \frac{3\mathrm{d}t^f}{b\,Wi} + \frac{\mathrm{d}t^f}{Wi} \right] \chi_{n+1} - \frac{\mathrm{d}t^f}{Wi} = 0, \tag{3.15}$$

where $R_{ii,*}$ is the stretching term computed with the approximation $\langle \hat{q}_i \hat{q}_j \rangle_*$ from the previous iteration. The two solutions are

$$\chi_{n+1} = -\frac{\beta}{2} \pm \frac{\sqrt{\beta^2 + 4\mathrm{d}t^f / Wi}}{2}, \tag{3.16}$$

where

$$\beta = R_{ii,*} \frac{\mathrm{d}t^f}{b} - \chi_n + \frac{3\mathrm{d}t^f}{b\,Wi} + \frac{\mathrm{d}t^f}{Wi}. \tag{3.17}$$

The trace of the tensor $\langle \hat{q}_i \hat{q}_j \rangle$ may not be greater than the extensibility parameter b, so that χ must be greater than 0. Therefore, the only valid solution is

$$\chi_{n+1} = -\frac{\beta}{2} + \frac{\sqrt{\beta^2 + 4\mathrm{d}t^f / Wi}}{2}. \tag{3.18}$$

Individual components of the conformation tensor $\langle \hat{q}_i \hat{q}_j \rangle$

Having the trace, the temporal discretization of Eq. 3.9 can be solved now for the individual components

$$\langle \hat{q}_i \hat{q}_j \rangle_{n+1} = \frac{\langle \hat{q}_i \hat{q}_j \rangle_n + (R_{ij,*} + \delta_{ij}/Wi)\mathrm{d}t^f}{1 + \mathrm{d}t^f/(Wi\chi_{n+1})}, \tag{3.19}$$

where $R_{ij,*}$ is the stretching term computed with the approximation $\langle \hat{q}_i \hat{q}_j \rangle_*$. This process is repeated iteratively until convergence to treat the stretching terms implicitly. The first iteration uses the conformation tensor $\langle \hat{q}_i \hat{q}_j \rangle_n$ at step n and the velocity gradients at step $n+1$ to compute $R_{ij,*}$, then the subsequent steps use the new value of the conformation tensor $\langle \hat{q}_i \hat{q}_j \rangle_{n+1}$. The iteration is performed until the difference between two iterations is smaller than a desired convergence value ϵ.

The presented algorithm is a robust numerical method to solve the FENE-P equation, ensuring that the trace never exceeds its maximal value b. The time step can be chosen so that the positive components of the conformation tensor $\langle \hat{q}_i \hat{q}_i \rangle$ are always greater than 0. If an arbitrary time step is chosen, a clipping method can be used to avoid negative values of the diagonal elements of $\langle \hat{q}_i \hat{q}_i \rangle$.

3.1.3 Brownian FENE-P model

To compute the extension vector $\hat{\boldsymbol{q}}$ of the Brownian FENE-P model (see Eq. (2.36)), the same scheme as for the FENE equations is used, but using the trace of the conformation tensor $\langle \hat{q}_i \hat{q}_j \rangle_{ii}$ calculated with the above algorithm for the spring force. The predictor step is

$$\hat{\boldsymbol{q}}_* = \hat{\boldsymbol{q}}_n + \left(\nabla \hat{\boldsymbol{u}}_n^f \cdot \hat{\boldsymbol{q}}_n - \frac{\hat{\boldsymbol{q}}_n}{2\,Wi\left(1 - \frac{\langle \hat{q}_i \hat{q}_i \rangle_{n+1}}{b}\right)} \right) \mathrm{d}t^f - \frac{1}{\sqrt{2\,Wi}} \mathrm{d}\hat{\boldsymbol{W}}_n. \tag{3.20}$$

The corrector step can be written as

$$\begin{aligned} &\left(1 + \frac{\mathrm{d}t^f}{4\,Wi\left(1 - \frac{\langle \hat{q}_i \hat{q}_i \rangle_{n+1}}{b}\right)}\right) \hat{\boldsymbol{q}}_{n+1} = \hat{\boldsymbol{q}}_n + \\ &\frac{1}{2}\left(\nabla \hat{\boldsymbol{u}}_{n+1}^f \cdot \hat{\boldsymbol{q}}_* + \nabla \hat{\boldsymbol{u}}_n^f \cdot \hat{\boldsymbol{q}}_n - \frac{\hat{\boldsymbol{q}}_n}{2\,Wi\left(1 - \frac{\langle \hat{q}_i \hat{q}_i \rangle_{n+1}}{b}\right)} \right) \mathrm{d}t^f - \frac{1}{\sqrt{2\,Wi}} \mathrm{d}\hat{\boldsymbol{W}}_n \end{aligned} \tag{3.21}$$

Unlike the scheme for the FENE model, Eq. (3.21) can be solved directly since $\langle \hat{q}_i \hat{q}_i \rangle$ is already known. However, this implies that Eq. (2.35) needs to be solved first.

3.1.4 FENE springs model

We use a similar semi-implicit predictor-corrector scheme as introduced by Somasi *et al.* (2002) to solve for $\hat{\boldsymbol{q}}_\nu$. In the predictor step, $\hat{\boldsymbol{q}}_{\nu,n}$ is explicitly updated to obtain $\hat{\boldsymbol{q}}_{\nu,*}$ as

$$\begin{aligned}\hat{\boldsymbol{q}}_{\nu,*} = \hat{\boldsymbol{q}}_{\nu,n} &+ \left(\nabla \hat{\boldsymbol{u}}_n^f \cdot \hat{\boldsymbol{q}}_{\nu,n} + \frac{1}{4\,Wi\hat{\lambda}}(\hat{\boldsymbol{F}}^{(c)}_{\nu-1,n} - 2\hat{\boldsymbol{F}}^{(c)}_{\nu,n} + \hat{\boldsymbol{F}}^{(c)}_{\nu+1,n})\right) \mathrm{d}t^f \\ &+ \frac{1}{\sqrt{2\,Wi\hat{\lambda}}}\left(\mathrm{d}\hat{\boldsymbol{W}}_{\nu+1,n} - \mathrm{d}\hat{\boldsymbol{W}}_{\nu,n}\right),\end{aligned} \tag{3.22}$$

where $\hat{\boldsymbol{F}}^{(c)}_{\nu,n} = \frac{\hat{\boldsymbol{q}}_\nu}{(1-||\hat{\boldsymbol{q}}_\nu||^2/b_s)}$ is the spring force for the νth segment at time t_n^f.

In the first corrector step, the spring forces $\bar{\boldsymbol{F}}^{(c)}$ for segments ν and $\nu-1$ are treated implicitly when solving for the approximation $\bar{\boldsymbol{q}}_\nu$ such that

$$\begin{aligned}\bar{\boldsymbol{q}}_\nu + \frac{\mathrm{d}t^f}{2\,Wi\hat{\lambda}}\bar{\boldsymbol{F}}^{(c)}_\nu = \hat{\boldsymbol{q}}_{\nu,n} &+ \left(\frac{1}{2}(\nabla \hat{\boldsymbol{u}}_{n+1}^f \cdot \hat{\boldsymbol{q}}_{\nu,*} + \nabla \hat{\boldsymbol{u}}_n^f \cdot \hat{\boldsymbol{q}}_{\nu,n}) + \frac{1}{4\,Wi\hat{\lambda}}(\bar{\boldsymbol{F}}^{(c)}_{\nu-1} + \hat{\boldsymbol{F}}^{(c)}_{\nu+1,n})\right) \mathrm{d}t^f \\ &+ \frac{1}{\sqrt{2\,Wi\hat{\lambda}}}\left(\mathrm{d}\hat{\boldsymbol{W}}_{\nu+1,n} - \mathrm{d}\hat{\boldsymbol{W}}_{\nu,n}\right),\end{aligned} \tag{3.23}$$

which upon rearrangement results in the following cubic equation for the magnitude of $\bar{\boldsymbol{q}}_\nu$ for each νth spring in the chain

$$|\bar{\boldsymbol{q}}_\nu|^3 - R|\bar{\boldsymbol{q}}_\nu|^2 - b_s\left(1 + \frac{\mathrm{d}t^f}{2\,Wi\hat{\lambda}}\right)|\bar{\boldsymbol{q}}_\nu| + b_s R = 0 \tag{3.24}$$

where R is the magnitude of the right hand side vector of Eq. (3.23). This equation has one unique solution between 0 and $\sqrt{b_s}$, and thus by choosing this root, we can ensure that $|\bar{\boldsymbol{q}}_\nu|$ is never greater than $\sqrt{b_s}$.

In the final corrector step, again the spring forces for segments ν and $\nu-1$ are treated

implicitly, while the spring force for segment $\nu+1$ is obtained from step 2

$$\begin{aligned}\hat{\boldsymbol{q}}_{\nu,n+1} + \frac{\mathrm{d}t^f}{2\,Wi\hat{\lambda}}\hat{\boldsymbol{F}}^{(c)}_{\nu,n+1} &= \hat{\boldsymbol{q}}_{\nu,n} \\ &+ \left(\frac{1}{2}(\nabla\hat{\boldsymbol{u}}^f_{n+1}\cdot\bar{\boldsymbol{q}}_\nu + \nabla\hat{\boldsymbol{u}}^f_n\cdot\hat{\boldsymbol{q}}_{\nu,n}) + \frac{1}{4\,Wi\hat{\lambda}}(\hat{\boldsymbol{F}}^{(c)}_{\nu-1,n+1} + \bar{\boldsymbol{F}}^{(c)}_{\nu+1})\right)\mathrm{d}t^f \\ &+ \frac{1}{\sqrt{2\,Wi\hat{\lambda}}}\left(\mathrm{d}\hat{\boldsymbol{W}}_{\nu+1,n} - \mathrm{d}\hat{\boldsymbol{W}}_{\nu,n}\right)\end{aligned} \tag{3.25}$$

The above equation results in a cubic equation similar to the previous one. Once every $\hat{\boldsymbol{q}}_{\nu,n+1}$ is known, the residual ϵ is calculated as the difference between the solutions $\bar{\boldsymbol{q}}_\nu$ and $\hat{\boldsymbol{q}}_{\nu,n+1}$

$$\epsilon = \sqrt{\sum_{\nu=1}^{N_s}\left(\hat{\boldsymbol{q}}_{\nu,n+1} - \bar{\boldsymbol{q}}_\nu\right)^2} \tag{3.26}$$

If this residual is greater than a specified tolerance (e.g., 10^{-6}), $\hat{\boldsymbol{q}}_{\nu,n+1}$ is copied onto $\bar{\boldsymbol{q}}_\nu$ and step 3 is repeated until convergence.

3.2 Algorithm for the Navier–Stokes equations

The flow solver uses classical second-order central finite differences on a staggered grid. In the first step, the polymer stress for the chosen polymer model is computed from both the solution at the previous time-step and the actual velocity field, which is subsequently advanced. The time advancement scheme of the velocity field relies on a semi-implicit fractional step method (Kim and Moin, 1985). The Newtonian viscous stress in the wall-normal direction is advanced in time with the Crank-Nicolson scheme, while all other terms in Eq. (2.51) are advanced with a third-order Runge-Kutta (RK3) method:

$$\frac{u_i^{(*)} - u_i^{(l-1)}}{\mathrm{d}t} = -\gamma_l N_i^{(l-1)} - \zeta_l N_i^{(l-2)} + \alpha_l\left(L_i^{(l)} + L_i^{(l-1)} + T_i^{(l)} + T_i^{(l-1)}\right), \tag{3.27}$$

$$\partial_k\partial_k\phi = \frac{1}{\alpha_l \mathrm{d}t}\partial_k u_k^{(*)}, \tag{3.28}$$

$$u_i^{(l)} = u_i^{(*)} - \alpha_l \mathrm{d}t\partial_i\phi, \tag{3.29}$$

where N, L and T are respectively the non-linear, diffusive and polymer terms. The index l is the sub-step of the Runge Kutta scheme, and γ_l, ζ_l and α_l are the corresponding coefficients: $\gamma_1 = 8/15$; $\zeta_1 = 0$; $\alpha_1 = 4/15$; $\gamma_2 = 5/12$; $\zeta_2 = -17/60$; $\alpha_2 = 1/15$; $\gamma_3 = 3/4$;

$\zeta_3 = -5/12$; $\alpha_3 = 1/6$. To maintain good resolution, the polymeric stress derivatives are calculated with a non-dissipative fourth-order compact scheme while the other gradients are computed with a second-order finite difference scheme (Min *et al.*, 2001).

3.3 Particle tracking

Solving Eq. (2.52) requires the computation of the velocity, $\boldsymbol{u}^p$, of the center-of-mass of the polymer molecule at its location, $\boldsymbol{x}^p$. Since the velocity field is computed in an Eulerian frame, it needs to be interpolated at the location $\boldsymbol{x}^p$ from the computational grid. The problem of the interpolation has already been extensively studied and it has been shown that a linear interpolation produces less accurate results than higher order schemes (Yeung and Pope, 1988; Kontomaris *et al.*, 1992). The method of choice is the cubic spline, which produces smooth velocity and velocity gradients over the grid cells. However, it cannot ensure a divergence free velocity gradient tensor inside the cells. In this study, the trilinear, the tricubic spline and a higher order interpolation (based on a Taylor expansion) have been tested. No significant differences have been found between results obtained from these schemes and therefore the trilinear interpolation was chosen, since it is faster than the other two methods and it preserves the zero divergence condition inside the cells. The relative insensitivity of the results on the interpolation scheme can be explained by the fact that the flow field calculation itself is based on a second order scheme while all other studies which showed that the trilinear interpolation performs poorly used spectral methods. A brief summary of these interpolation schemes can be found in appendix A.

In the uncoupled case, the polymer equations are solved on a smaller time scale than the time scale of the flow field calculation. Therefore, the velocity at the intermediate time steps is obtained by linearly interpolating two consecutive flow fields in time. The particle itself is advanced using a second order Runge-Kutta scheme. A fourth order scheme has also been tested, but the results are similar.

In the coupled case, both the flow and the polymer equations are advanced simultaneously. Therefore, the same third-order Runge-Kutta scheme is used to advance the particles as the one used for the flow.

3.4 Polymer stress and the problem of advection

As stated in the previous chapter, the polymer stress can be computed in either an Eulerian or a Lagrangian framework. Although this work is based on the Lagrangian approach, it is interesting to consider the Eulerian approach as well, in order to understand the challenges which arise when solving the FENE-P equations.

3.4.1 Eulerian framework

All the previous studies have relied on the Eulerian method to solve the equations for the polymer phase. However, they all faced similar numerical issues which arise from the advection term of the FENE-P equations casted in the Eulerian framework:

$$\frac{\partial}{\partial t^f}\langle\hat{\boldsymbol{q}}\hat{\boldsymbol{q}}\rangle + \boldsymbol{u}\cdot\nabla\langle\hat{\boldsymbol{q}}\hat{\boldsymbol{q}}\rangle = \nabla\boldsymbol{u}^f\cdot\langle\hat{\boldsymbol{q}}\hat{\boldsymbol{q}}\rangle + \langle\hat{\boldsymbol{q}}\hat{\boldsymbol{q}}\rangle\cdot\nabla\boldsymbol{u}^{f\dagger} - \frac{1}{Wi}\left(\frac{\langle\hat{\boldsymbol{q}}\hat{\boldsymbol{q}}\rangle}{1-\mathrm{tr}\langle\hat{\boldsymbol{q}}\hat{\boldsymbol{q}}\rangle/b} - \boldsymbol{\delta}\right). \tag{3.30}$$

One can notice that the second term on the left-hand side of Eq. (3.30) represents the advection of the configuration tensor by the flow. However, Eq. (3.30) does not contain any diffusive terms. In reality diffusion takes place, but at much smaller scales than the Kolmogorov scale. Typically, the Schmidt number $Sc = \nu/\kappa$ associated with drag reducing polymers is of the order of 10^6, where ν is the kinematic viscosity of the solution and κ is the diffusion coefficient. As it was shown by Batchelor (1959), when $Sc \gg 1$ the spectrum of the advected quantity decreases with a slope of -1 beyond the Kolmogorov scale. Therefore, at high Schmidt numbers the convected quantity still possesses energy at very small scales. This is exactly the case for the FENE-P equation. The absence of any diffusion implies that the energy cut-off scale tends to infinity. This means that it is impossible to compute a true Direct Numerical Simulation (DNS) of the polymer phase, and that numerical artifices are needed to ensure a stable computation on the chosen mesh.

The advection problem explains why all the previous simulations needed to add a so-called Artificial Dissipation (AD) term. Studies having opted for a spectral-like approach used a Global Artificial Diffusion (GAD) (Beris and Sureshkumar, 1996; Beris and Dimitropoulos, 1999; Dimitropoulos *et al.*, 2001), while it is possible to introduce a Local Artificial Diffusion (LAD) in studies based on finite differences (Min *et al.*, 2001; Dubief and

Lele, 2001). With this AD, Eq. (3.30) becomes

$$\begin{aligned}\frac{\partial}{\partial t^f}\langle\hat{\boldsymbol{q}}\hat{\boldsymbol{q}}\rangle + \boldsymbol{u}\cdot\nabla\langle\hat{\boldsymbol{q}}\hat{\boldsymbol{q}}\rangle =& \nabla\boldsymbol{u}^f\cdot\langle\hat{\boldsymbol{q}}\hat{\boldsymbol{q}}\rangle + \langle\hat{\boldsymbol{q}}\hat{\boldsymbol{q}}\rangle\cdot\nabla\boldsymbol{u}^{f\dagger} \\ &- \frac{1}{Wi}\left(\frac{\langle\hat{\boldsymbol{q}}\hat{\boldsymbol{q}}\rangle}{1-\mathrm{tr}\langle\hat{\boldsymbol{q}}\hat{\boldsymbol{q}}\rangle/b} - \boldsymbol{\delta}\right) + AD.\end{aligned} \tag{3.31}$$

This artificial diffusion was historically introduced to avoid a loss of positive- definitiveness of the configuration tensor $\langle\hat{\boldsymbol{q}}\hat{\boldsymbol{q}}\rangle$. However, the influence of this additional term is not fully understood. Although activation of AD is very limited in high-drag reduction regimes (HDR), this is not the case at low-drag reduction (LDR) and during the transient phase. Moreover, even at HDR, the impact of inadequate resolution of the polymer phase is totally unknown.

The Eulerian method is in general constrained to using constitutive equations and is therefore limited in its accuracy. However, the constraint can be relaxed if one relies on the Brownian Configuration Fields method (Oettinger *et al.*, 1997; Hulsen *et al.*, 1997).

3.4.2 Lagrangian framework and the modified Adaptive Lagrangian Particle Method

Because of the nature of the Lagrangian approach, the aforementioned problem can be avoided. However, the polymer stress in the Lagrangian framework is only known at the particles' location by solving the polymer equations with any algorithm discussed in section 3.1, and a method is needed to transfer this information back to the Eulerian grid in order to advance the flow in time. Such a transfer between the Lagrangian and Eulerian frameworks was already needed to compute the particles' velocity and velocity gradient tensor from the Eulerian flow field as explained previously in section 3.3. This transfer of the polymer stress is not needed in the uncoupled case but is necessary in order to simulate drag reduction. One method which can be applied is a modified version of the Adaptive Lagrangian Particle Method (ALPM) (Halin *et al.*, 1998; Gallez *et al.*, 1999; Wapperom *et al.*, 2000).

The basic idea of the ALPM is to compute the polymer stress at the center of a cell of the mesh from the particles within this cell. This implies that a minimum number of particles need to be present in each grid cell. In a uniform mesh, one could simply seed a large enough number of particles at the beginning of the simulation and since the particles

are Lagrangian tracers, there should statistically always be a minimum number of particles in each cell since the particles tend to have a uniform volume distribution. However, if the mesh is non-uniform, the initial number of particles needed to ensure a good particle distribution in each grid cell is constrained by the smallest cells. This implies that in the bigger cells a very large number of particles might be present, which causes a huge increase in computation time. Moreover, the bigger cells are usually located where less resolution is needed. To overcome this issue, one can constrain the number of particles within each cell between a minimum (to ensure good resolution to compute the cell value) and a maximum value (to avoid computation costs and load unbalance in parallel computation).

While the main idea behind the ALPM is trivial, the implementation turns out to be more complicated. Namely, the constraint on the number of particles implies that particles need to be created in some cells and destroyed in others. Therefore, one has to develop an algorithm for the creation and destruction of particles and for the calculation of the cell value of the polymer stress.

Computation of the cell value of the polymer stress

The original ALPM by Gallez *et al.* (1999) uses a least-squares fit of trilinear interpolation of the Lagrangian stress values within the cell to compute the cell stress value. However, the flow Gallez *et al.* (1999) investigated was the start-up flow between two highly eccentric rotating cylinders at very low Reynolds number. The flow was smooth enough to lead to a very smooth polymer stress distribution. In the case of a turbulent channel flow, the distribution of the polymer stress over the particles within a cell is very broad due to the strong turbulent mixing and the presence of small scales. The use of a least-squares fit turned out to be impossible because it led to unphysical values, i.e. negative components of the diagonal of the polymer stress tensor $\boldsymbol{\tau}_P$.

Therefore, the method chosen was to do a cell average of the Lagrangian stress $\boldsymbol{\tau}_{p,i}$ to obtain the Eulerian stress $\boldsymbol{\tau}_P$

$$\boldsymbol{\tau}_P = \frac{1}{N_{\text{cell}}} \sum_{i=1}^{N_{\text{cell}}} \boldsymbol{\tau}_{p,i}, \tag{3.32}$$

where N_{cell} is the actual number of particles within the cell.

Other methods could be developed but this one has the advantages of being very simple and preserves the positiveness of the diagonal elements of the tensor.

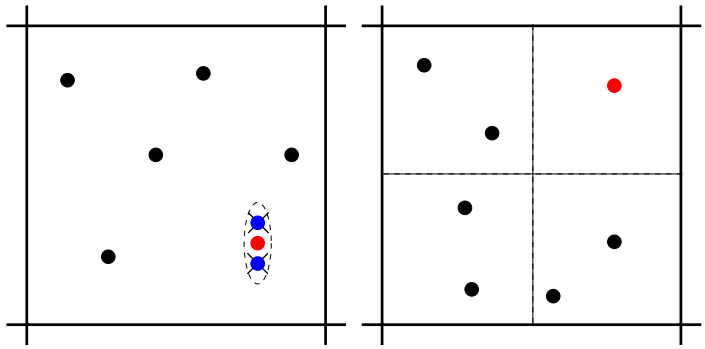

(a) Destruction (b) Creation

Figure 3.1: Schematic of the creation and destruction of particles within a cell.

Destruction of particles

If the number N_{cell} of particles within the cell is greater than the maximum number of particles, $N_{\text{cell},max}$, the two closest neighbors are found and replaced by one particle at mid-distance of them. The new particle is given the average stress of the two it replaces. This is schematically illustrated in Fig. 3.1. The procedure is repeated iteratively until the number of particles in the cell is equal to the maximum number of particles allowed.

Creation of particles

If too few particles are present in a cell, new ones need to be created. The first step is to determine the quadrant (in three dimension) of the cell with the least number of particles and to randomly define the position of the new particle as depicted in Fig. 3.1. Different options are available to assign the value of the polymer stress to the newly created particle. One can give it for instance the mean cell value or use a trilinear interpolation using the neighbor cell values to determine the polymer stress at the location of the new particle. Both methods have been implemented.

Obviously the creation and destruction of particles induces an uncontrolled diffusion. But the nature and level of this diffusion can be investigated in the uncoupled simulations. Moreover, one has the freedom to choose the bounds for the number of particles.

Chapter 4

Validation of the numerical methods

The previous chapter introduced the algorithms used to solve the equations presented in chapter 2. This chapter focuses on the validation of the implementation of these algorithms. First, the polymer models are tested in simple flows and results are compared to those found in the literature. Then the accuracy of the particle tracking scheme is illustrated by sample trajectories and the comparison of the Lagrangian and Eulerian statistics. Finally, the modified Adaptive Lagrangian Particle Method is validated in a model flow, i.e., the Taylor vortex cells.

4.1 Polymer solution in simple flows

A very good test case to validate the numerical method for the polymer stress calculation is simple shear and elongational flows. As a first step, both the FENE and FENE-P models are investigated, i.e., Eq. (2.33) are solved numerically using 50000 realizations and the stress is then computed as an ensemble average over all realizations. The time step ranges from $\mathrm{d}t = 0.001$ to $\mathrm{d}t = 0.005$, depending on the Weissenberg number. The results for the dimensionless shear viscosity, $\langle \tau_{xy} \rangle / Wi$, and the first normal stress coefficient, $\langle \tau_{xx} - \tau_{yy} \rangle / Wi^2$, in a shear flow are shown in Fig. 4.1 and 4.2 while the dimensionless elongational viscosity $\langle \tau_{xx} - \tau_{yy} \rangle / Wi$ in an elongational flow is shown in Fig. 4.3. Each case was computed for different Weissenberg numbers and maximum extensibility parameter, b. The results compare very well with published data (Herrchen and Oettinger, 1997) (not shown).

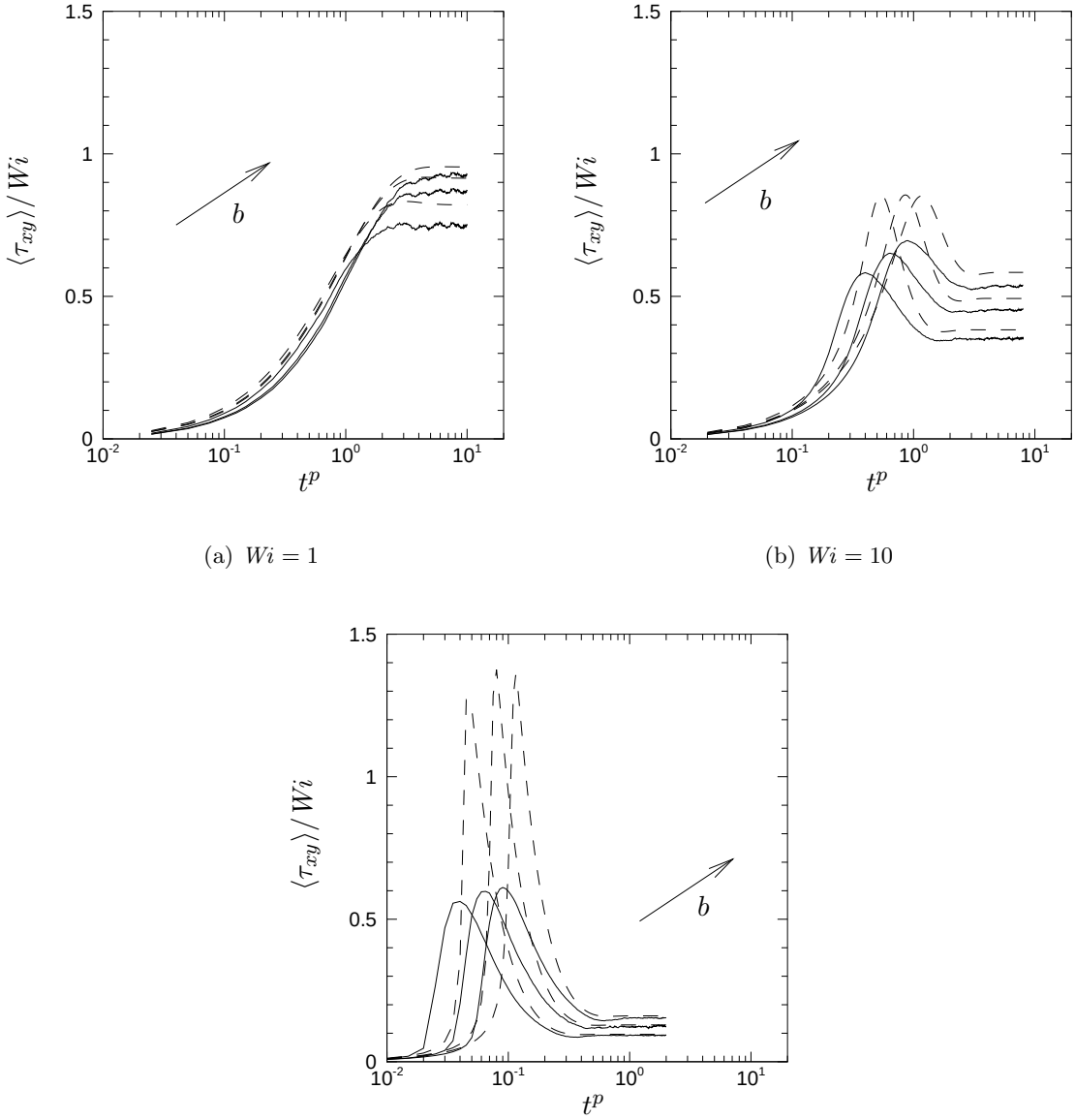

(a) $Wi = 1$

(b) $Wi = 10$

(c) $Wi = 100$

Figure 4.1: Dimensionless viscosity in shear flow for the FENE (——) and FENE-P (– – –) models at different Wi for $b = 20, 50$ and 100.

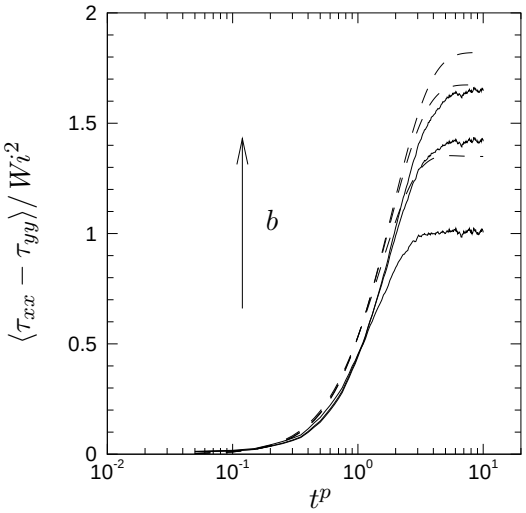

(a) $Wi = 1$

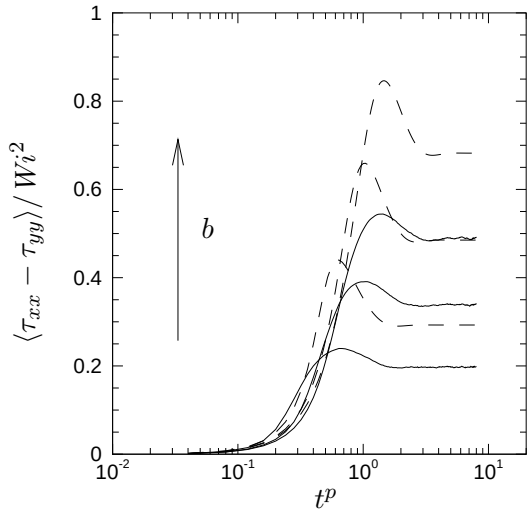

(b) $Wi = 10$

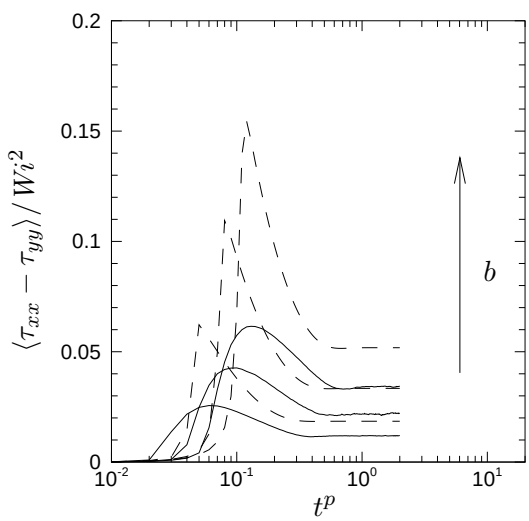

(c) $Wi = 100$

Figure 4.2: Dimensionless first normal stress coefficient in shear flow for the FENE (——) and FENE-P (– – –) models at different Wi for $b = 20, 50$ and 100.

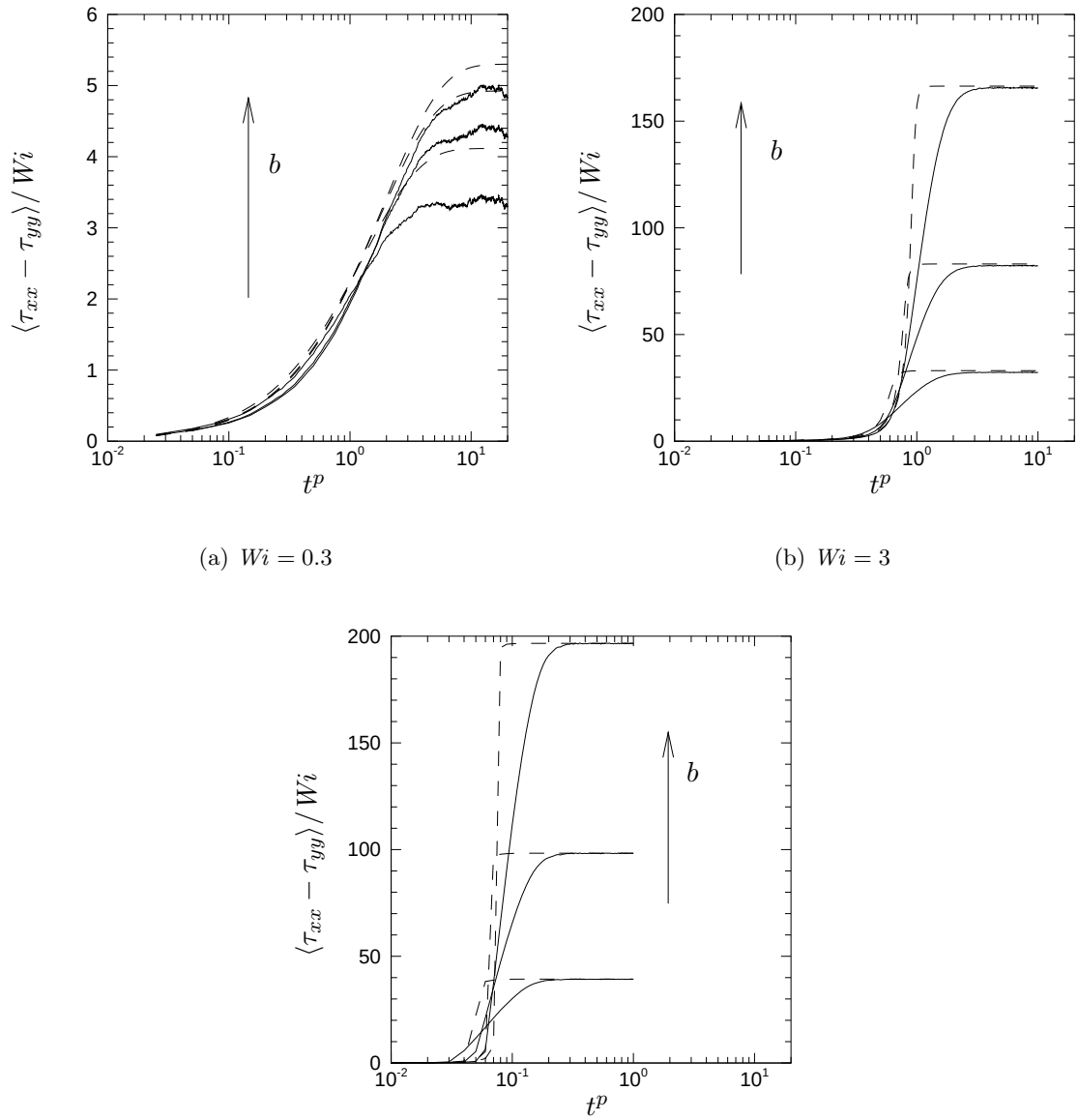

(a) $Wi = 0.3$

(b) $Wi = 3$

(c) $Wi = 30$

Figure 4.3: Dimensionless elongational viscosity in elongational flow for the FENE (——) and FENE-P (– – –) models at different Wi for $b = 20, 50$ and 100.

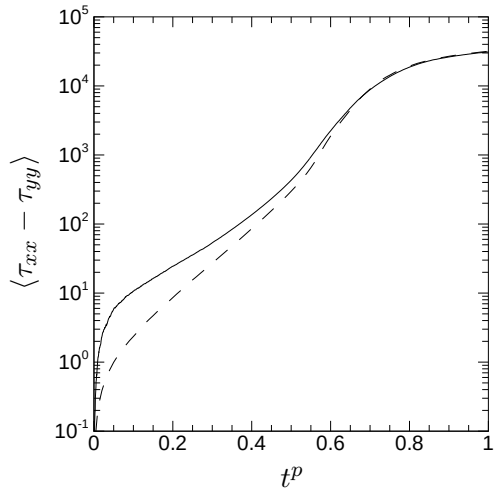

Figure 4.4: First normal stress difference in elongational flow at $Wi = 6$ for $b = 3600$. FENE 10 springs (——) and FENE dumbbell (– – –).

In the case of shear flow, both models exhibit an overshoot at increasing shear rates before reaching their steady value. The maxima in the viscosity and in the first normal stress coefficient occur at a later time with increasing b. The value of these maxima as well as the steady values also increase with b. It is interesting to note that the discrepancy between the FENE and FENE-P models increases with the Weissenberg number. This is also a well documented feature of the FENE-P model and suggests that the FENE-P model might not be adequate to represent correctly the polymer phase for drag reduction. The discrepancy is also noticeable in the case of inception of elongational flow. There, the FENE-P model reaches its steady value at much earlier time than the FENE model. However, it has the great advantage of being a constitutive equation, which explains why all of the previous works on polymer drag reduction were based on the FENE-P model.

In a similar way, the FENE bead-spring chain model (see Eq. 2.49) is compared to the FENE dumbbell model. The results for the first normal stress in an elongational flow are shown in Fig. 4.4. One can notice that the steady values agree very well, but as it has already been observed, the transient phase demonstrates a much larger stress in the case of a multi-mode simulation. This is well known (Ghosh *et al.*, 2001) and accurately reproduced here. This discrepancy is caused by the fact that the FENE model accounts for only one relaxation mode and suggests that representation of internal modes might be important to

accurately simulate polymer drag reduction.

4.2 Newtonian turbulent flow and particle tracking

In order to validate the particle tracking and flow solver algorithms, one can compare the flow statistics obtained from both approaches. Moreover, sample trajectories of particles are also analyzed. Results are obtained from the simulation of a channel flow at constant mass flux in a minimal channel (Jimenez and Moin, 1991,) for a Reynolds number $Re = Uh/\nu = 7500$, where U is the corresponding center line velocity of the Poiseuille flow, h is the half height of the channel and ν is the kinematic viscosity. The flow time scale is therefore defined as $t^f = h/U$. The channel is periodic in the x- and z-directions and has dimension $\pi h \times 2h \times h$. The simulation has been carried out on a grid of $64 \times 129 \times 32$ points giving a Reynolds number in wall units of $Re^+ = u_\tau h/\nu = 318$ (where the friction velocity $u_\tau = 0.042$) so that $\Delta x^+ = 15.9$, $\Delta y^+ = 0.3 - 13$ (the grid is non-uniform in the wall-normal direction) and $\Delta z^+ = 9.9$. Finally a constant time step of $\Delta t^f = 0.001$ was chosen, ensuring a CFL number much smaller than one. To achieve converged statistics, a large number of particles were needed. In this case, $N_p = 10^5$ particles homogeneously distributed were used with each of them having a different trajectory.

4.2.1 Comparison of Eulerian and Lagrangian statistics

In order to validate the particle tracking algorithm, one can compare flow statistics obtained from classical Eulerian statistics and from the Lagrangian calculation. To compute Lagrangian statistics, one groups the particles in layers as a function of the distance from the wall y^+ and computes the mean value for each of the layers. Results for the velocity statistics are shown in Fig. 4.5. The agreement for the mean streamwise velocity U^+ is very good. The very small discrepancy is mainly due to the averaging introduced by the binning used for the Lagrangian statistics. The agreement is also very good for the Root Mean Square (rms) values of the velocity fluctuations, although the Lagrangian statistics tend to show slightly smaller values. This is most probably due to the way the statistics are computed, and to a lesser extent to the low pass filtering characteristics of the trilinear interpolation scheme. But overall one can conclude that the Lagrangian and Eulerian statistics are in very good agreement.

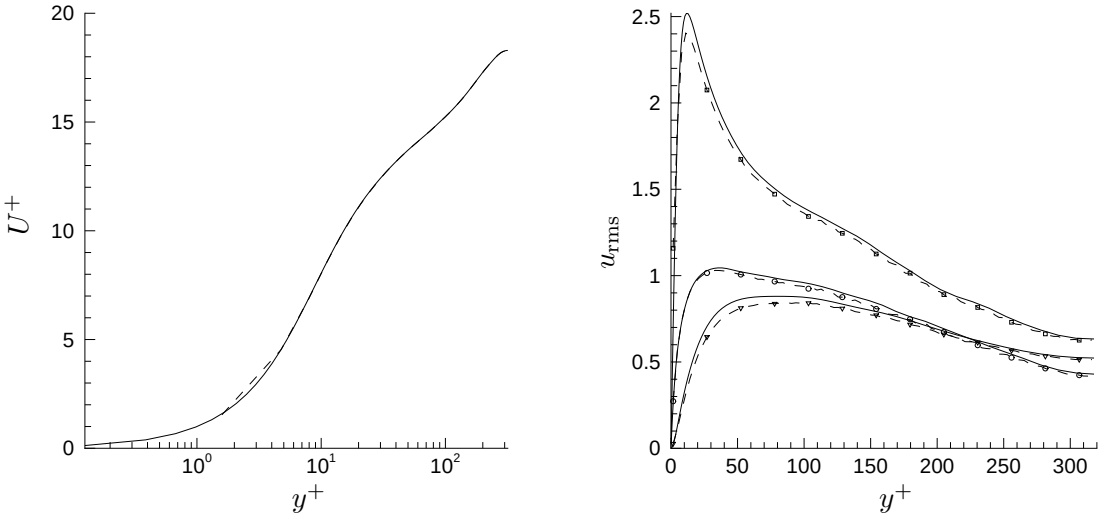

(a) Mean streamwise velocity

(b) Rms of velocity fluctuations

Figure 4.5: Velocity statistics for Lagrangian (– – –) and Eulerian (——) simulations in a channel flow at constant mass flow and $Re = 7500$. □: u (streamwise), ▽: v (wall-normal) and ○: w (spanwise).

4.3 Advection of a passive scalar in a Taylor vortex cell

In order to validate the Lagrangian method described in section 3.4.2, the advection of a passive scalar in a Taylor vortex cell is considered. This model problem is of the same hyperbolic nature as the FENE-P equation as discussed in section 3.4.1. However, it has no source terms, which makes it easier to analyze. Moreover, the two-dimensional flow field $\boldsymbol{u}$ is known analytically so that only the passive scalar equation

$$\frac{\partial c}{\partial t} + \boldsymbol{u}\frac{\partial c}{\partial \boldsymbol{x}} = 0 \tag{4.1}$$

needs to be solved for the scalar value $c(x, y, t)$, thus allowing a direct comparison between different numerical approaches.

4.3.1 Taylor-Green vortex and problem formulation

The Taylor-Green vortex is an exact solution of the Navier-Stokes equations consisting of a two-dimensional array of counter-rotating vortices (Taylor and Green, 1937). The analytical solution is given on the periodic domain $(0, 0) \leq (x, y) \leq (2\pi, 2\pi)$ by

$$u = F(t) \sin x \cos y, \tag{4.2}$$

$$v = -F(t) \cos x \sin y, \tag{4.3}$$

$$p = -\frac{1}{4} F^2(t) \left(\cos 2x + \sin 2y\right), \tag{4.4}$$

where u and v are the velocities in the x and y directions, respectively, and p is the pressure. The time dependence is given by the function $F(t) = F_0 \exp(-2\nu t)$, thus in the inviscid case ($\nu = 0$) the flow becomes time-independent. The streamlines are shown in Fig. 4.6 (a). One can see that each of the four cells are independent. Moreover, the streamlines are closed loops. Therefore, it is expected that the passive scalar only travels along these loops. F_0 was chosen arbitrarily to be unity so that the velocity is bounded by -1 and 1.

We seek a solution to Eq. 4.1 given the inviscid flow described by Eq. 4.2. While the velocity field is steady, the passive scalar will develop in time from the chosen initial condition

$$c_0(x, y) = c(x, y, t = 0) = \sin(y) \tag{4.5}$$

shown in Fig. 4.6 (b). The problem is 2π-periodic in both the x and y directions. While

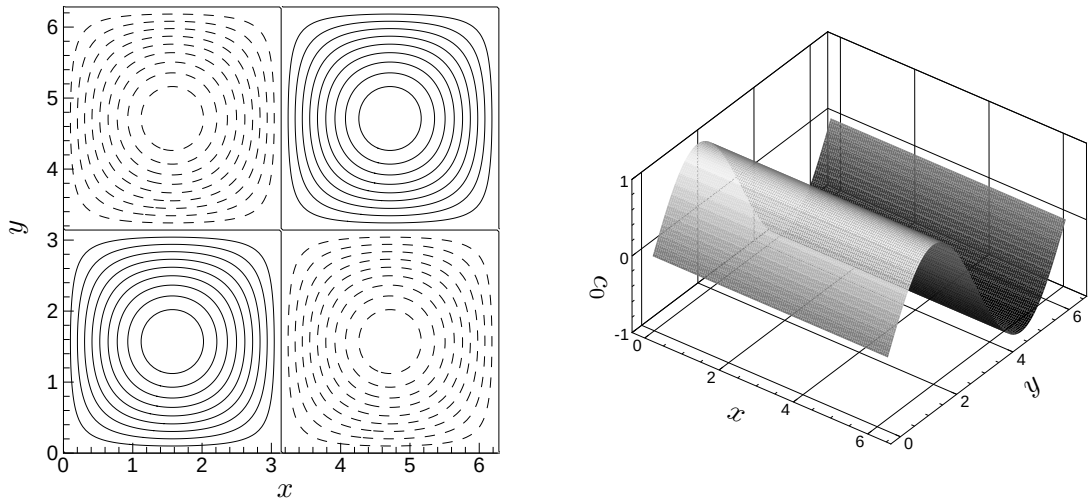

(a) Streamlines

(b) Initial distribution of passive scalar

Figure 4.6: Streamlines of a Taylor-Green vortex cell and initial distribution of the passive scalar $c_0(x, y)$.

c contains only one wave number in the y direction, in its initial distribution, it will be redistributed by the flow and higher wave numbers will be created through the convective term in Eq. 4.1.

4.3.2 Spectral analysis

The system being completely 2π-periodic and because the initial condition is real, symmetric in the x direction and antisymmetric in the y direction, one can assume a solution to the problem of the form

$$c(x, y, t) = \sum_{m=0}^{\infty} \sum_{n=1}^{\infty} \hat{c}_{m,n}(t) \cos mx \sin ny, \tag{4.6}$$

and substitute it into Eq. 4.1. After some algebra, one finds a system of coupled ordinary differential equations (ODE) of infinite dimension:

$$\begin{aligned} 4\frac{\mathrm{d}\hat{c}_{m,n}}{\mathrm{d}t} &= (m-n)\hat{c}_{m+1,n+1} + (m+n)\hat{c}_{m+1,n-1} \\ &\quad - (m+n)\hat{c}_{m-1,n+1} - (m-n)\hat{c}_{m-1,n-1}, \end{aligned} \tag{4.7}$$

with the initial condition

$$\hat{c}_{m,n}(t=0) = \begin{cases} 1 & \text{if } m=0,\, n=1, \\ 0 & \text{otherwise.} \end{cases} \tag{4.8}$$

It can be noticed that because the wave number (m, n) depends only on the corner values $(m+1, n+1)$, $(m-1, n+1)$, $(m+1, n-1)$ and $(m-1, n-1)$, every $\hat{c}_{m,n}$ where m and n are either both even or odd will remain zero.

From Eq. 4.7, one can see that the initial energy contained in a lower wave number diffuses through the convective term to higher wave numbers. Moreover, since the assumed solution is an infinite series (see Eq. 4.6), there is no cut-off wave number in the spectrum. With increasing time, smaller scales will contain increasingly more energy. This represents an enormous challenge for any numerical simulation, since the smallest scales resolved will be determined by the finite grid. Yet it is an interesting and insightful test for any numerical method aiming at solving the FENE-P equation.

To evaluate the different numerical methods, it is useful to monitor the conserved quantities. If one integrates Eq. 4.1 over the whole volume and uses the Gauss theorem, using the periodicity of the boundary conditions, the conservation law for the passive scalar, c, is obtained:

$$\frac{\partial}{\partial t}\int_V c \mathrm{d}V = 0. \tag{4.9}$$

Similarly, if one multiplies Eq. 4.1 by c before the volume integration, the conservation of c squared is obtained

$$\frac{\partial}{\partial t}\int_V \frac{1}{2}c^2 \mathrm{d}V = 0, \tag{4.10}$$

if the flow is divergence free, which is the case here.

4.3.3 Discretization of the velocity field

While the velocity field is known analytically, Eq. 4.1 needs to be solved on a discrete grid. In order to ensure the conservation properties of traditional schemes, it is necessary to enforce the zero divergence condition discretely. However, this condition is not satisfied by the analytical velocity field. Therefore, one has to discretize the flow field on the discrete grid (x_i, y_j).

If one defines $\boldsymbol{u}^*_{i,j}$ and $\boldsymbol{u}_{i,j}$ to be the analytical and discretized velocity at the location

(x_i, y_j), respectively, it is clear that

$$\partial_x u^*_{i,j} + \partial_y v^*_{i,j} = 0 \neq \delta_x u^*_{i,j} + \delta_y v^*_{i,j}, \tag{4.11}$$

where ∂ and δ are the continuous and discretized operators, respectively. However, one can apply a projection method identical to the one used in the traditional fractional steps method (Le and Moin, 1991), i.e., one corrects the divergent velocity field through a so-called pressure correction Φ

$$u_{i,j} = u^*_{i,j} - \delta_x \Phi, \tag{4.12}$$

$$v_{i,j} = v^*_{i,j} - \delta_y \Phi, \tag{4.13}$$

where Φ satisfies the Poisson equation

$$\delta_x^2 \Phi + \delta_y^2 \Phi = \delta_x u^*_{i,j} + \delta_y v^*_{i,j}. \tag{4.14}$$

It can be verified that the new discretized velocity is indeed divergence free by applying the divergence operator to Eq. 4.12. In the case where the discretized operator is a standard central finite difference operator of second order, one has to solve a linear system of equations, which can easily be done.

4.3.4 Comparison of different numerical methods

In order to evaluate the different numerical methods considered in this work, Eq. 4.1 is solved on a 128^2 grid using a 3rd order Runge-Kutta time advancement. Both the ALPM (see section 3.4.2) and the traditional Eulerian method are compared. The grid is chosen to be uniform in both directions. Two different Eulerian approaches are investigated: the traditional second order finite difference with the convective term in the skew-symmetric form, and the higher order upwind compact scheme introduced by Min *et al.* (2001) and modified by Dubief and Lele (2001).

4.3.5 Lagrangian solution

In order to validate the ALPM, it is necessary to investigate every source of numerical errors, i.e., the time integration, the interpolation scheme, the number of particles, the resolution

of the grid and the creation/destruction algorithm. The following parameters are chosen as the basic case for comparison. The time integration is performed with the aforementioned third order Runge-Kutta method and a time step of $\mathrm{d}t = 10^{-2}$, the grid is uniform and contains 128 points in each direction, the velocity of each particle is interpolated from the discretized flow field with a trilinear scheme, and each cell initially contains $N = 20$ particles. Moreover, the number of particles per grid cell is not constrained, so particles do not need to be created or destroyed. In order to compare the different solutions, the 'energy', $1/2c^2$, is recorded as a function of time up to $t_{\mathrm{fin}} = 100$. Moreover, a one-dimensional profile of the solution c through the one of the four vortices is plotted as a function of x at time $t = 50$ and location, $y = \pi/2$.

In order to visualize the solution, a three-dimensional view of c at $t = 50$ is shown in Fig. 4.7. The solution was computed with the same parameters as the base case but on a 256^2 grid. One can see the four different cells each corresponding to a vortex. As expected the solution shows a symmetry and antisymmetry between the different cells.

As mentioned above, the total energy of the physical system should be conserved but the spectral analysis showed that energy transfers from the larger scales to the smaller ones. In the Lagrangian method, the transfer of information, i.e. c, from the particles to the Eulerian grid involves a cell average

$$c_e = \sum_{n_{\mathrm{cell}}} c_p / n_{\mathrm{cell}}, \tag{4.15}$$

where c_p and c_e are the passive scalar values at the particle locations and at the cell centers of the Eulerian grid respectively. If no creation or destruction occur, the total energy $1/2c_p^2$ over all particles remains constant. However, the scales which are smaller than the ones resolved by the mesh will contain increasingly more energy with time, which is lost by the averaging involved in the transfer from Lagrangian to Eulerian mesh.. Therefore, the resolved energy $1/2c_e^2$ is expected to decrease with time, the missing energy being contained in the unresolved scales. This is well illustrated by Fig. 4.8(a), where the total energy $1/2c_p^2$ contained in the particles remains constant while the resolved energy $1/2c_e^2$ decreases.

The time integration is validated by reducing the time step by a factor of 10 to $\mathrm{d}t = 10^{-3}$. Both the time evolution of the energy and the solution are compared to the base case and shown in Fig. 4.8. One can observe that the solutions are identical, demonstrating the accuracy of the time integration.

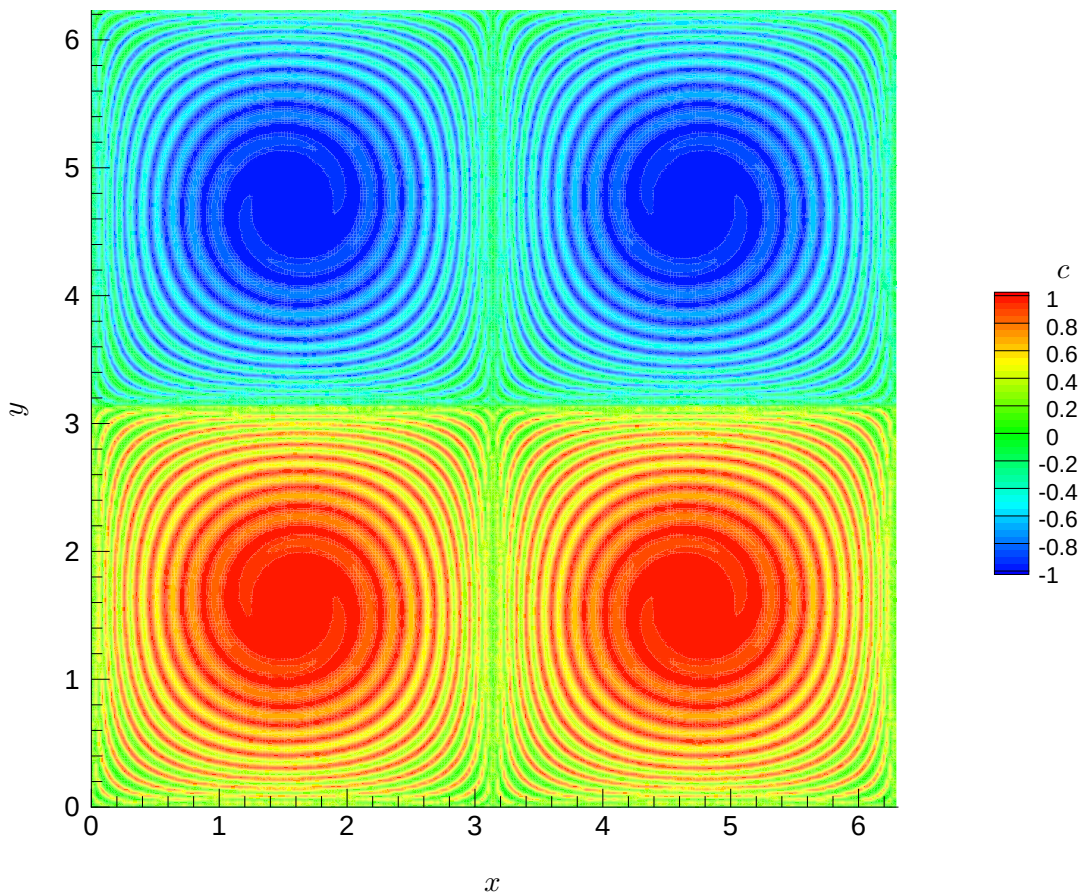

Figure 4.7: Solution of the passive scalar equation in the Taylor-Green vortex at $t = 50$ on a 256^2 grid and $N = 20$ initial particles per cell without creation or destruction.

The spatial interpolation scheme of the velocity is validated by comparing the results given by the base case to a simulation where the velocity is computed directly from the analytical expression. One can see in Fig. 4.9 that both results compare almost exactly.

While the initial number of particles per cell chosen in the base case is somehow arbitrary, an increase of the number of particles does not change the solution dramatically, as illustrated in Fig. 4.10. One can observe a very small change in the energy evolution and some small quantitative differences at a few points, particularly at the edge of the vortex. However, the general features of the solution are well captured and a good quantitative agreement is observed.

When the solution is computed on a finer mesh, smaller scales can be resolved. Therefore, the energy content of these scales is also captured leading to a higher total resolved energy. This is illustrated in Fig. 4.11. As expected, the solution exhibits higher levels of fluctuations. However, if the more resolved solution is filtered onto the coarser grid, one obtains almost exactly the same coarser solution. Moreover, the energy of the filtered solution corresponds to that of the base case. This is a powerful property of the Lagrangian method in the case of a linear problem, i.e., the lack of resolution of the small scales does not impact the computation of the larger ones. A refinement of the mesh only adds new information without altering the already known solution.

Although the mesh is in this case uniform, it is interesting to evaluate the diffusion induced by the creation and destruction of particles. Therefore, the base case is compared to the solution obtained when the number of particles within a cell is constrained. Results for the creation of particles based on the mean value of the cell are shown for different bounds in Fig. 4.12, while the results obtained from the interpolation of the neighbour cells are shown in Fig. 4.13. One observes that the tighter the bounds are, the more diffusive the solution is. This can be expected since tight bounds implies a larger number of particles destroyed and created. However, it is interesting to note that the general qualitative characteristics of the solution are conserved if the number of particles in a cell is not too constrained. Moreover, it seems that the creation method based on the mean value of the cell gives better results then the interpolation method (see section 3.4.2) and is less diffusive, at least in this simple case.

It is also important to note that the maximum and minimum values of the scalar c, i.e., 1 and -1, are conserved with the Lagrangian method. This is a great property of the method which is not, in general, shared by Eulerian methods.

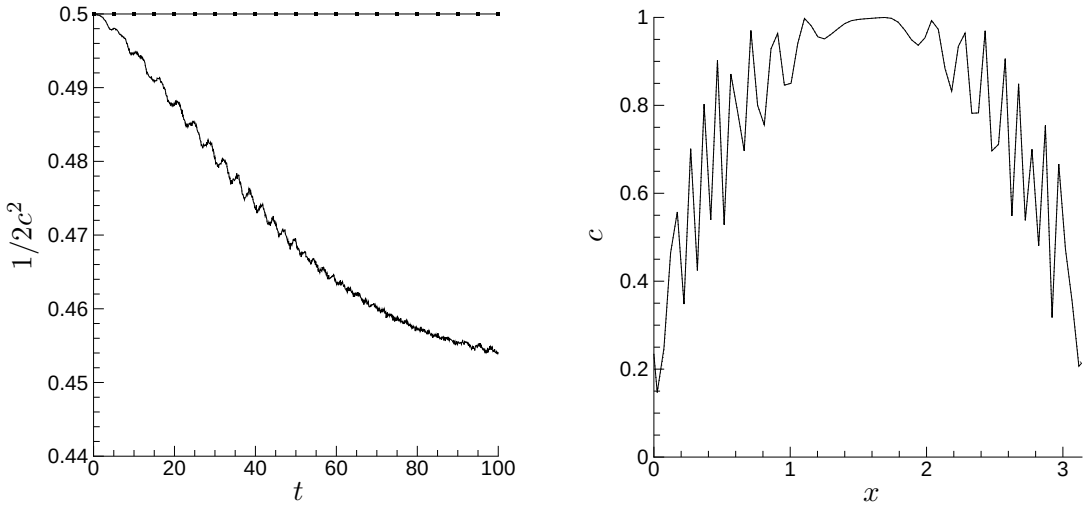

(a) Energy $1/2c^2$

(b) Passive scalar c

Figure 4.8: Comparison of the resolved energy $1/2c_e^2$ as a function of time and the passive scalar value c as a function of x at $y = \pi/2$ and $t = 50$ for both $\mathrm{d}t = 10^{-3}$ $(\cdots)$ and $\mathrm{d}t = 10^{-2}$ (——) velocity and $N = 20$ initial particles per cell without creation or destruction. Symbols represent the total energy $1/2c_p^2$ contained in the particles.

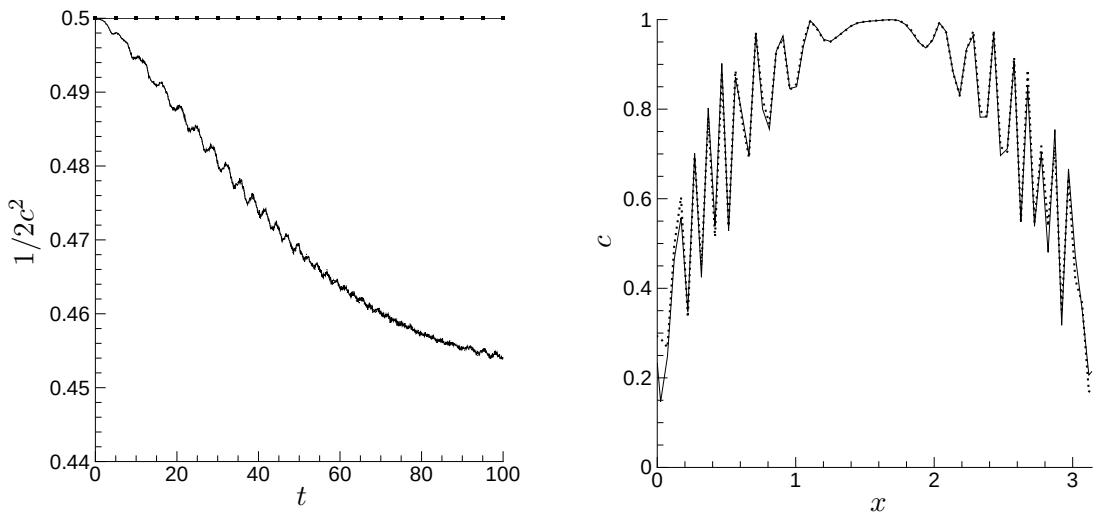

(a) Energy $1/2c^2$

(b) Passive scalar c

Figure 4.9: Comparison of the resolved energy $1/2c_e^2$ as a function of time and the passive scalar value c as a function of x at $y = \pi/2$ and $t = 50$ for both the analytical $(\cdots\cdot)$ and interpolated (——) velocity and $N = 20$ initial particles per cell without creation or destruction. Symbols represent the total energy $1/2c_p^2$ contained in the particles.

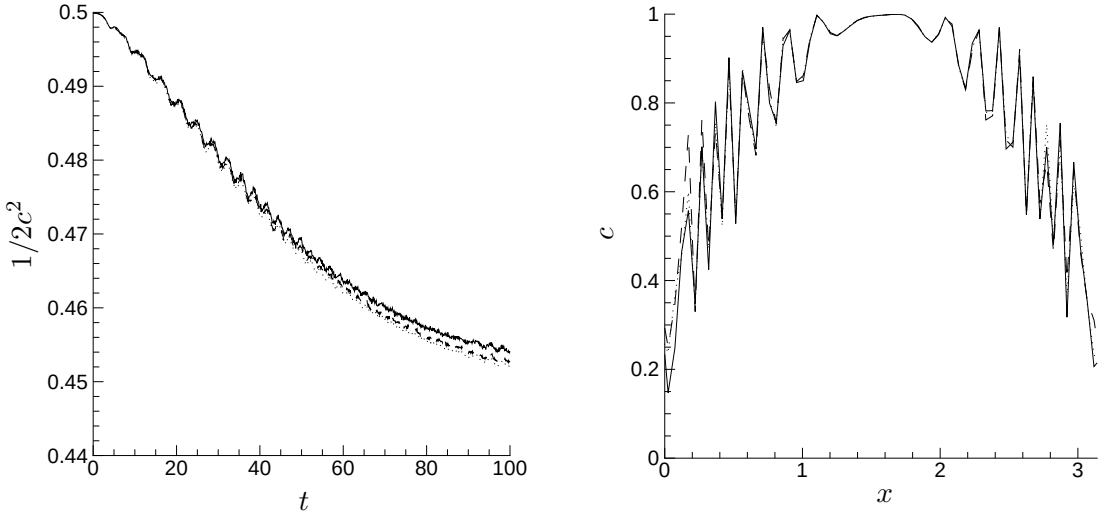

(a) Energy $1/2c^2$

(b) Passive scalar c

Figure 4.10: Comparison of the resolved energy $1/2c_e^2$ as a function of time and the passive scalar value c as a function of x at $y = \pi/2$ and $t = 50$ for $N = 20$ (——), $N = 40$ (– – –) and $N = 80$ ($\cdots$) initial particles per cell without creation or destruction.

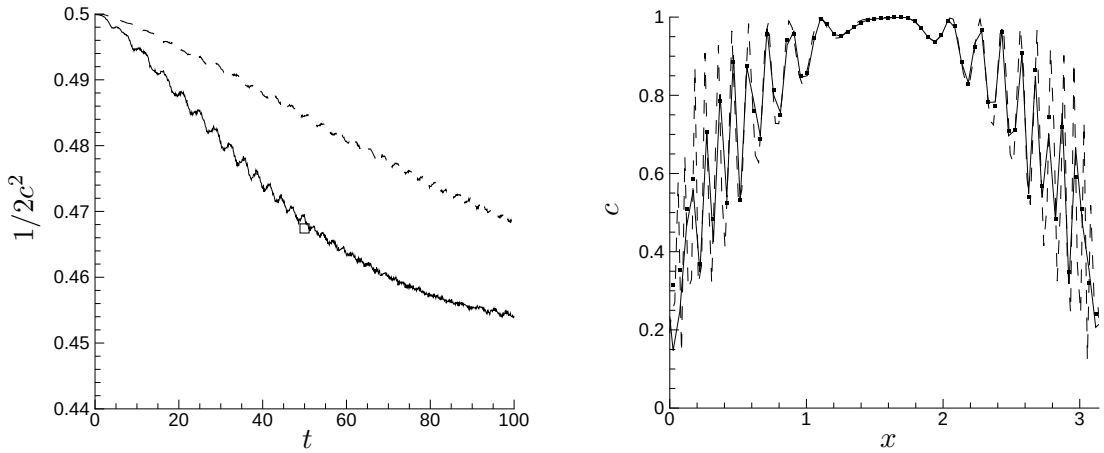

(a) Energy $1/2c^2$

(b) Passive scalar c

Figure 4.11: Comparison of the resolved energy $1/2c_e^2$ as a function of time and the passive scalar value c as a function of x at $y = \pi/2$ and $t = 50$ for $N = 20$ initial particles per cell and a 128^2 (——) and a 256^2 (– – –) grid. The symbols □ correspond to the solution of the finer mesh filtered onto the coarser.

4.3.6 Eulerian solution

In this section the Lagrangian method is compared to the more traditional Eulerian methods. The first method considered is a centered 2nd order finite difference scheme. Because of the advective nature of the equation, it is expected that a central scheme will perform poorly, which it indeed does. Therefore, an artificial diffusion is added to the equation

$$\frac{\partial c}{\partial t} + \boldsymbol{u}\boldsymbol{\nabla} c - \kappa \boldsymbol{\nabla}^2 c = 0 \tag{4.16}$$

to control large oscillations. The convective term is discretized using the skew-symmetric form (Morinishi *et al.*, 1998) in order to have an energy conservative scheme. However, since the total energy $1/2c^2$ is conserved, the energy which should cascade to the smaller, unresolved scales actually remains in the resolved ones. Therefore, an unphysical amplification of larger scales is observed. This results in an unphysical increase of the maximum and minimum values of c, which can only be controlled by the addition of artificial diffusion. Results with different diffusion coefficients κ are compared in Fig. 4.14. One can see that

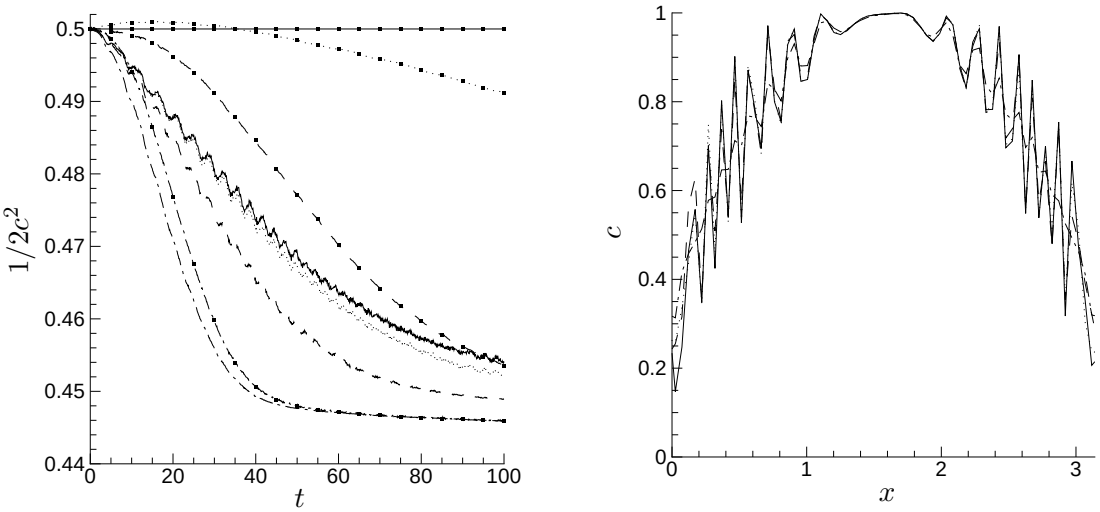

(a) Energy $1/2c^2$

(b) Passive scalar c

Figure 4.12: Comparison of the resolved energy $1/2c_e^2$ as a function of time and the passive scalar value c as a function of x at $y = \pi/2$ and $t = 50$ for $N = 20$ initial particles per cell and $N_{min,max} = (0, \infty)$ (——), $N_{min,max} = (10, 30)$ ($\cdots$), $N_{min,max} = (15, 25)$ (– – –) and $N_{min,max} = (18, 22)$ (–·–). The creation of new particles is based on the mean value of c in the cell. Symbols represent the total energy $1/2c_p^2$ contained in the particles.

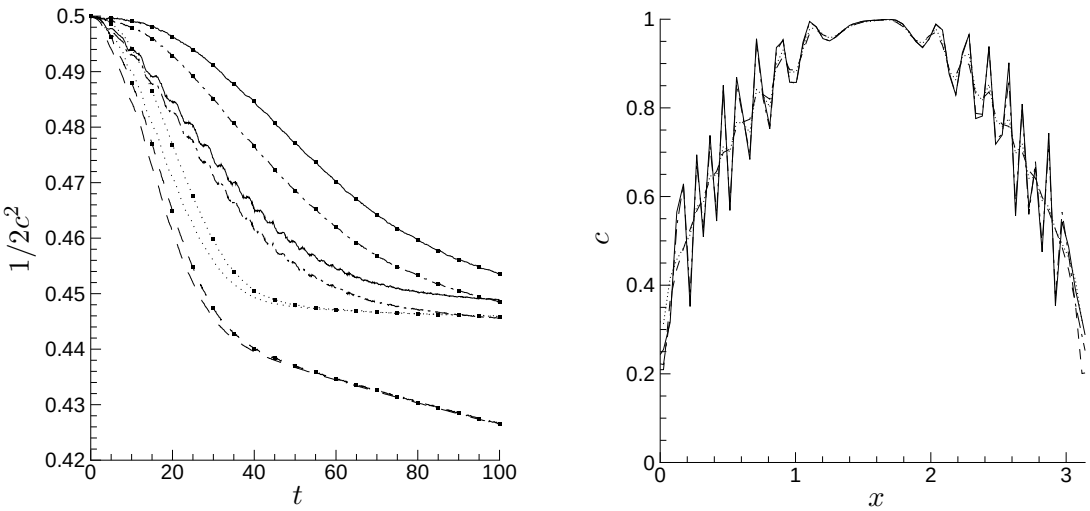

(a) Energy $1/2c^2$

(b) Passive scalar c

Figure 4.13: Comparison of the resolved energy $1/2c_e^2$ as a function of time and the passive scalar value c as a function of x at $y = \pi/2$ and $t = 50$ for $N = 20$ initial particles per cell. Creation based on the mean cell value: $N_{min,max} = (15, 25)$ (——), $N_{min,max} = (18, 22)$ $(\cdots)$; creation based on the interpolation of the mean value of the neighbour cells: $N_{min,max} = (15, 25)$ $(-\cdot-)$, $N_{min,max} = (18, 22)$ $(---)$. Symbols represent the total energy $1/2c_p^2$ contained in the particles.

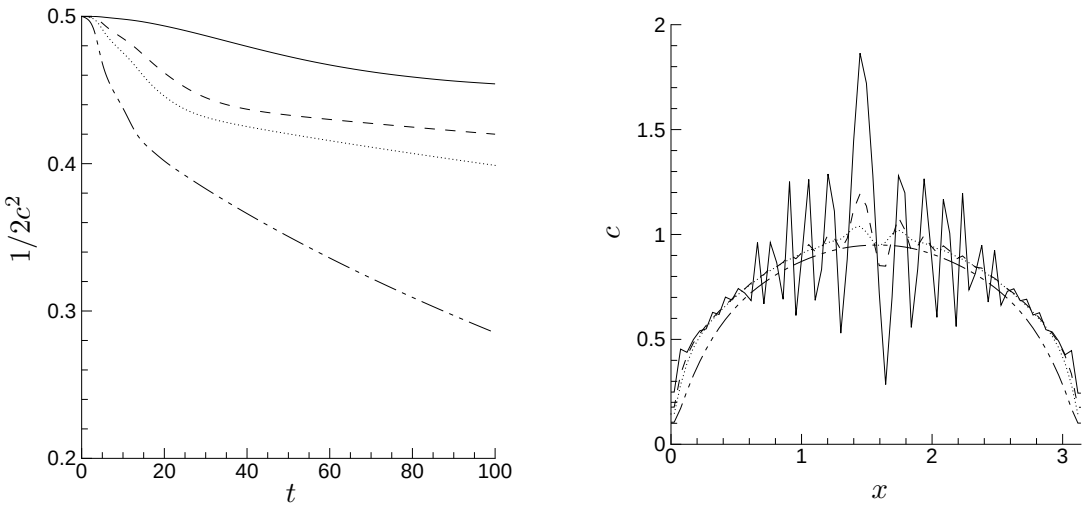

(a) Energy $1/2c^2$

(b) Passive scalar c

Figure 4.14: Comparison of the resolved energy $1/2c_e^2$ as a function of time and the passive scalar value c as a function of x at $y = \pi/2$ and $t = 50$ for the centered finite difference method and different diffusion coefficient. $\kappa = 10^{-5}$: ——, $\kappa = 10^{-4}$: $---$ and $\kappa = 2 \cdot 10^{-4}$: $\cdots$, $\kappa = 10^{-3}$: $-\cdots-$.

with a very small diffusion, the solution still exhibits an overshoot of the maximum values and large oscillations. This is even true for $\kappa = 10^{-4}$, which leads to a larger energy loss than the Lagrangian method. If κ is increased, the solution becomes much smoother and remains within the bounds, but does not show any of the small scales present in the physical solution.

Another scheme investigated is the modified upwind compact scheme introduced by Min *et al.* (2003) and modified by Dubief and Lele (2001) to solve the FENE-P equation. Artificial dissipation is not needed in this case due to the dissipative nature of any upwind scheme. It is important to notice that the advective term is discretized using the convective form. The use of the skew-symmetric form would not ensure energy conservation since the upwind character of the scheme induces dissipation; moreover, the velocity field is discretely divergence free with respect to a central finite difference scheme but not with the compact scheme. The results found are compared to the Lagrangian base case in Fig. 4.15. One can see that the scheme is much more diffusive than the Lagrangian method, even when

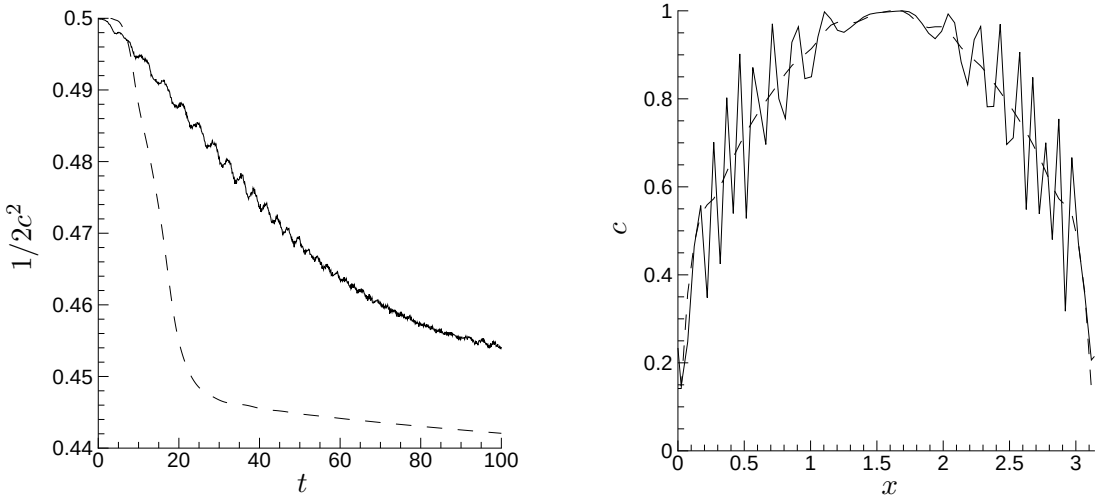

(a) Energy $1/2c^2$

(b) Passive scalar c

Figure 4.15: Comparison of the resolved energy $1/2c_e^2$ as a function of time and the passive scalar value c as a function of x at $y = \pi/2$ and $t = 50$ for the upwind compact scheme (– – –) and the Lagrangian method (——) with $N = 20$ initial particles per cell and no creation or destruction.

creation and destruction of particles is implemented (see Fig. 4.12 and 4.12). Moreover, the solution is much smoother and does not replicate accurately the small scales found with the Lagrangian method. If a finer mesh is used (see Fig. 4.16), smaller scales are captured in the center of the vortex but not on its sides.

4.3.7 Discussion

The advection of a passive scalar in a Taylor-Green vortex cell is a very valuable model problem since it exhibits similar characteristics to the FENE-P model in a flow. The validation of the Lagrangian method shows that the method is naturally adequate for this type of problem. It surpasses the traditional Eulerian methods in terms of accuracy, stabiltity and robustness. It is important to emphasize that the Lagrangian method is much more expensive in terms of computation cost on a given mesh. However, to reach the same accuracy as the Lagrangian method, the Eulerian requires a much finer mesh, and thus becomes more computationally expensive.

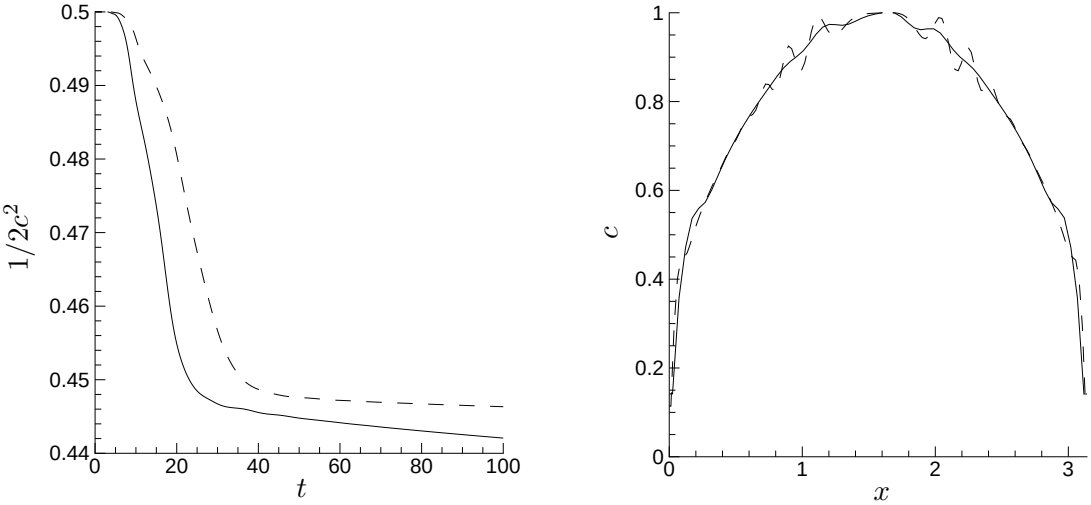

(a) Energy $1/2c^2$

(b) Passive scalar c

Figure 4.16: Comparison of the resolved energy $1/2c_e^2$ as a function of time and the passive scalar value c as a function of x at $y = \pi/2$ and $t = 50$ for the upwind compact scheme on a 128^2 grid (——) and a 256^2 grid (– – –).

The principal disadvantage of the Lagrangian method is the uncontrolled diffusion introduced by the creation and destruction of particles. However, as was demonstrated above, this diffusion does not alter significantly the qualitative behaviour of the solution. Moreover, the diffusion can be reduced by larger bounds on the minimum and maximum number of particles within each cell. Another disadvantage is the non-smoothness of the solution.

While the Lagrangian approach produces great results in this simple model problem, it can be questioned whether it is also well suited for the polymer drag reduction case. The first issue is that the velocity field is much less smooth than the Taylor-Green vortex, and thus the velocity and velocity gradient interpolations will introduce more significant diffusion. Moreover, the mesh used to solve the channel flow is in general not uniform, thus increasing the need for creation and destruction of particles, which again increases the diffusion. Yet in light of the previous results, it should be expected that the Lagrangian method will outperform the Eulerian approach. Also note that the advection of a passive scalar is an extreme case since the value of each particle only depends on its initial value. Therefore, the solution is strongly history dependent, while in the polymer case, the stretching term depends on the local velocity gradient, rendering the solution much less history dependent. It can be expected that the error introduced at particle creation decreases with time.

Chapter 5

One-way coupling calculations

Before simulating drag reduced flows, it is of interest to first consider uncoupled simulations, i.e., simulations where the polymer dynamics is driven by the flow but where the polymer stress does not couple back to it. Therefore, the flow is not modified by the polymers. This allows a very good comparison of the different polymer models and a better understanding of the mechanisms of polymer stretching in turbulent flow. Moreover, the algorithm is simpler and therefore less sensitive to numerical issues since one does not need to implement the complete ALPM introduced in section 3.4.2.

In this chapter we first provide a comparison of different polymer models. Then the topological methodology is introduced to explain the mechanisms of polymer stretching. Finally, conditional statistics are used to test the hypothesis made using the topological methodology approach.

5.1 Comparison of polymer models

Because in an uncoupled simulation the flow is not modified by the polymers, a single polymer molecule will experience exactly the same flow history, independently of the model chosen. This allows a more precise comparison of the models. This comparison is obtained in a channel flow identical to the one used in section 4.2 but on a slightly finer grid, i.e. $96 \times 151 \times 64$ points, giving a Reynolds number in wall units of $Re^+ = 290$ (Terrapon *et al.*, 2003). To achieve converged statistics, a large number of particles is needed. In this case, $N_p = 10^5$ particles were used with each of them having a different trajectory. The extensibility parameter was chosen to be $b = 3600$ in order to simulate real molecules. Other

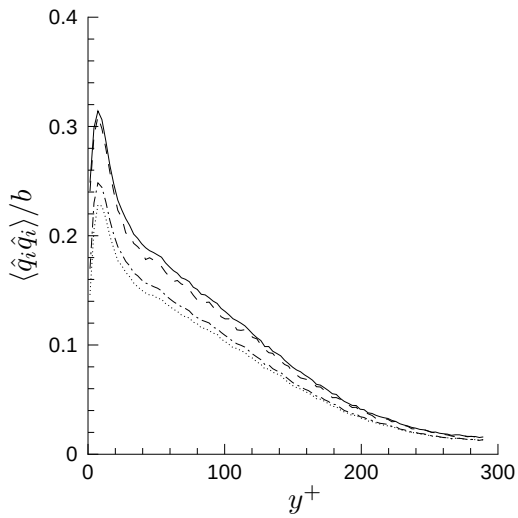

Figure 5.1: Comparison of the mean square extension $\langle \hat{q}_i \hat{q}_i \rangle / b$ as a function of the distance y^+ from the wall for different polymer models with $b = 3600$ and $Wi = 3$. FENE-P: ——; Brownian FENE-P: – – –; FENE: – . –; FENE bead-spring chain with $N_s = 5$: · · · ·.

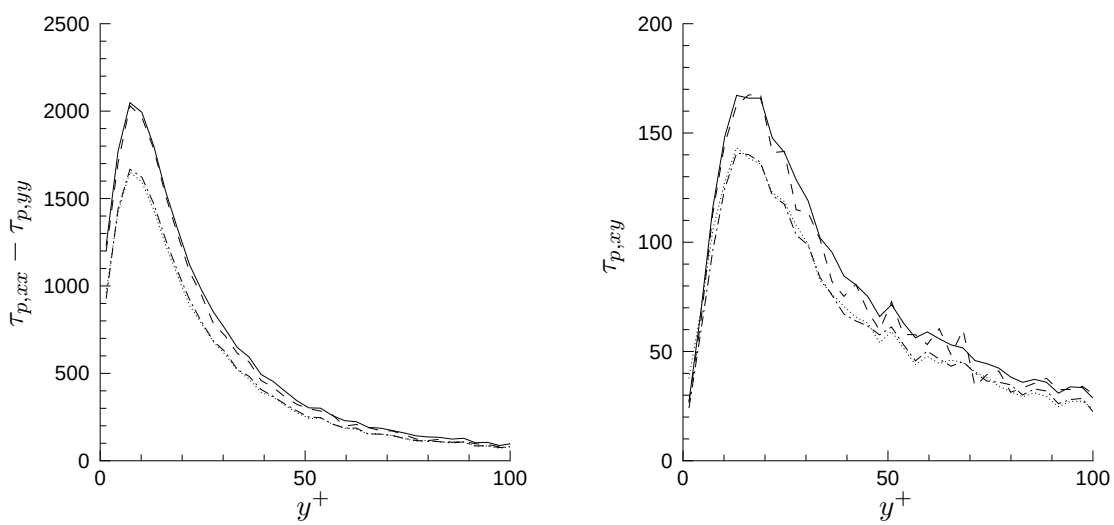

(a) First normal stress $\tau_{p,xx} - \tau_{p,yy}$

(b) Shear stress $\tau_{p,xy}$

Figure 5.2: Comparison of the polymer stress in the near-wall region for different polymer models with $b = 3600$ and $Wi = 3$. FENE-P: ——; Brownian FENE-P: – – –; FENE: – . –; FENE bead-spring chain with: · · · ·.

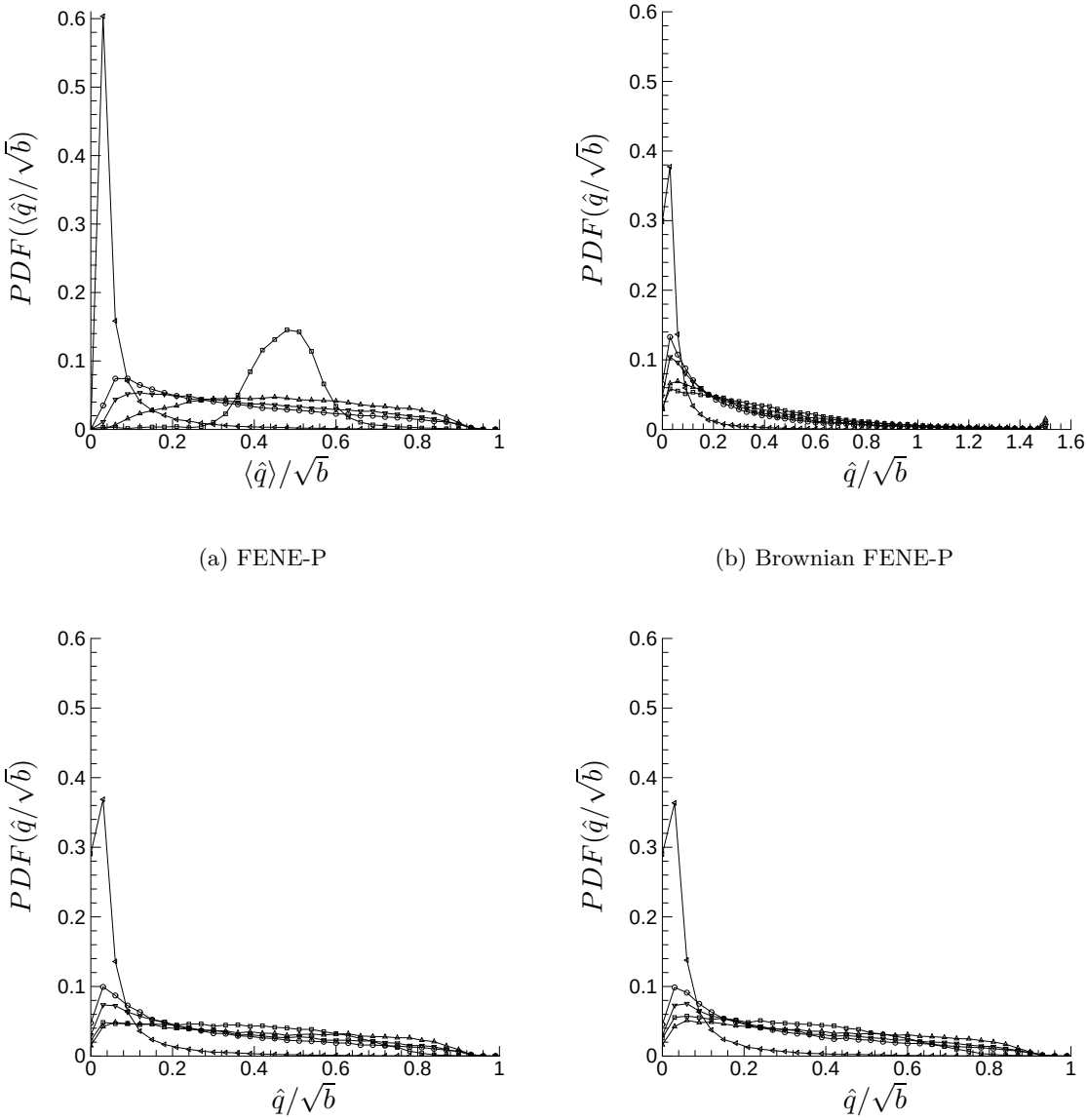

(a) FENE-P

(b) Brownian FENE-P

(c) FENE

(d) FENE bead-spring chain ($N_s = 5$)

Figure 5.3: Probability Density Function of the extension $\hat{q}/b$ for different polymer models at different distances y^+ from the wall. $\square$: $0.0 \leq y^+ \leq 2.9$; $\triangle$: $11.6 \leq y^+ \leq 14.5$; $\triangledown$: $26.2 \leq y^+ \leq 29.1$; $\circ$: $52.3 \leq y^+ \leq 55.2$; $\triangleleft$: $287.8 \leq y^+ \leq 290.7$.

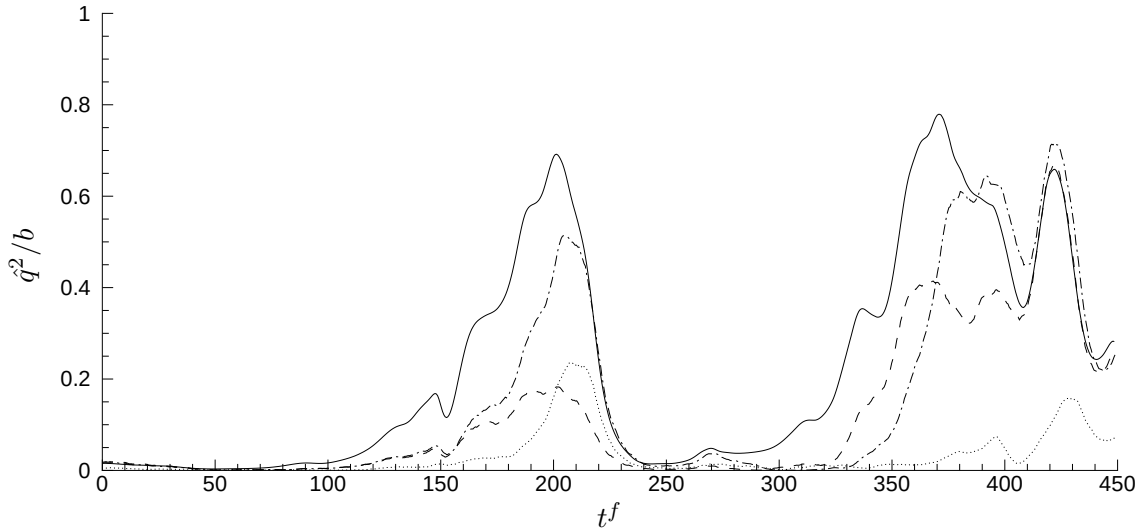

Figure 5.4: Comparison of the extension history of a single particle for different polymer models with $b = 3600$ and $Wi = 3$. FENE-P: ——; Brownian FENE-P: – – –; FENE: – . –; FENE bead-spring chain with $N_s = 5$: · · · ·.

calculations were also performed with $b = 900$ and $b = 10000$, which gave qualitatively similar results. The polymer models used are the FENE-P, the Brownian FENE-P, the FENE and the FENE bead-spring chain models. The bead-spring chain used had 5 springs corresponding to 5 relaxation modes. In all simulations we used $Wi = 3$ corresponding to a Weissenberg number based on the wall shear $Wi^+ = \lambda_H u_\tau/\nu = 34$.

The sensitivity of the results on different parameters was investigated. The mesh was refined, the time step was decreased and the number of particles was increased, but no significant alteration of the results was found.

Figure 5.1 shows the mean square extension $\langle \hat{q}_i \hat{q}_i \rangle$ non-dimensionalized by the maximum extensibility parameter b as a function of the distance y^+ from the wall. It can be seen that all models give qualitatively the same profile. The FENE-P models give a higher extension, which can be expected from the results shown in section 4.1. The identical behavior is shown in Fig. 5.2 for the first normal stress, $\tau_{p,xx} - \tau_{p,yy}$, and shear stress $\tau_{p,xy}$. One can conclude from these results that internal modes don't seem to be very important to capture the dynamics of the polymer. Moreover, the FENE-P model gives a good qualitative approximation of more realistic models (FENE, bead-spring chain), although it tends to overpredict extension and stress.

One can observe that the main action of the polymers is confined to a region near the wall (approximatively $0 \leq y^+ \leq 100$) with a maximum extension and stress at a distance $y^+ = 10 - 20$. This can be expected since it is more or less the location of the quasi-streamwise vortices which are a major player in the coil-stretch transition of polymer molecules, as will be demonstrated in a subsequent section.

The Probability Density Function (PDF) of the extension $\hat{q}/\sqrt{b}$ at different distances from the wall (see Fig. 5.3) demonstrates again a very good qualitative agreement between the different models (except for Fig. 5.3(a)). However, it should be noticed that higher extensions than allowed (i.e., $\sqrt{b}$) are seen for the Brownian FENE-P model. This is explained by the fact that the spring force is controlled by the average extension computed from the FENE-P model, but individual realizations can overshoot this value. On the other hand, the FENE-P model demonstrates a much narrower distribution close to the wall. This is expected since the FENE-P model already describes the average conformation of the polymer molecules and not single individual realizations. The flow near the wall corresponds approximatively to a simple shear flow. Therefore, the FENE-P model should give a very sharp distribution centered around its analytical value for a simple shear flow, which for the considered parameters is $\hat{q}/\sqrt{b} = 0.5$. Since the flow is only approximatively a simple shear flow near the wall, the actual distribution of the constitutive FENE-P model is broader because of flow fluctuations. However, as soon as the particles are away from the wall, the distribution becomes very broad. One can conclude that the broad distribution of the extension in the near-wall region is mainly due to the different flow types present there. It is therefore very instructive to investigate the constitutive FENE-P model since one could otherwise conclude that the broad distribution shown by the FENE model is only due to the Brownian term, as it is in the case for a simple shear flow. In the center of the channel, most of the chains are in a coil state.

A comparison of the different models along the same trajectory for a given particle is shown in Fig. 5.4. One can see that despite a very different history, each model reacts qualitatively similarly to the same events. But it is clear that on an individual basis, the actual extension history of a realization can vary greatly.

5.2 Topological methodology

It was found in the previous section that the main action of the polymers takes place in the near-wall region. However, the exact mechanisms associated with the coil-stretch transition of a polymer are not clear yet. Therefore, it is instructive to analyze in depth the FENE model. As mentioned in chapter 2, the second term on the right hand side of Eq. (2.33) corresponds to the spring force which tends to bring back the polymer molecule to its coil configuration. It opposes the tendency of the flow to stretch the polymer and therefore ensures a bounded extension. Its nonlinearity becomes important when it approaches its maximal extension. The third term on the right hand side of Eq. (2.33) represents the Brownian motion and has a zero mean. This term only adds a stochastic character to the dynamics and becomes less important at high Wi. Thus the stretching of a polymer molecule is mainly driven by the first term on the right hand side of Eq. (2.33), unless the polymer is sitting near regions of simple shear flow where Brownian motion and advection balance in the configuration dynamics.

The use of the topological methodology introduced by Chong *et al.* (1990) is motivated by the analogy of Eq. (2.33) and the equation for the flow patterns at a critical point

$$\frac{\mathrm{d}\boldsymbol{y}}{\mathrm{d}t} = \nabla \boldsymbol{u} \cdot \boldsymbol{y}, \tag{5.1}$$

where $\boldsymbol{y}$ determines the shape of the local flow field seen by an observer traveling with a fluid particle (like the polymer molecules in this case) and $\nabla \boldsymbol{u}$ is the velocity gradient tensor. Equation (5.1) would represent the trajectories of the dumbbell beads in the absence of the spring and Brownian forces. Indubitably the entropic and Brownian forces alter these dynamics, but since the spring force only constrains the stretching of the molecule, the unraveling of the polymer molecule is driven by the first term on the right hand side of Eq. (2.33). Therefore, it is very instructive to analyze this term in more detail.

The topological methodology is based on the solutions of Eq. (5.1) rewritten in its canonical form. The flow topologies of an incompressible flow can then be classified according to the eigenvalues of the velocity gradient tensor (Chong *et al.*, 1990; Blackburn *et al.*, 1996)). These eigenvalues define the three dimensional flow type seen by a polymer molecule at its location. For an incompressible flow the eigenvalues, σ, are obtained as solutions of the characteristic equation

$$\sigma^3 + Q\sigma + R = 0, \tag{5.2}$$

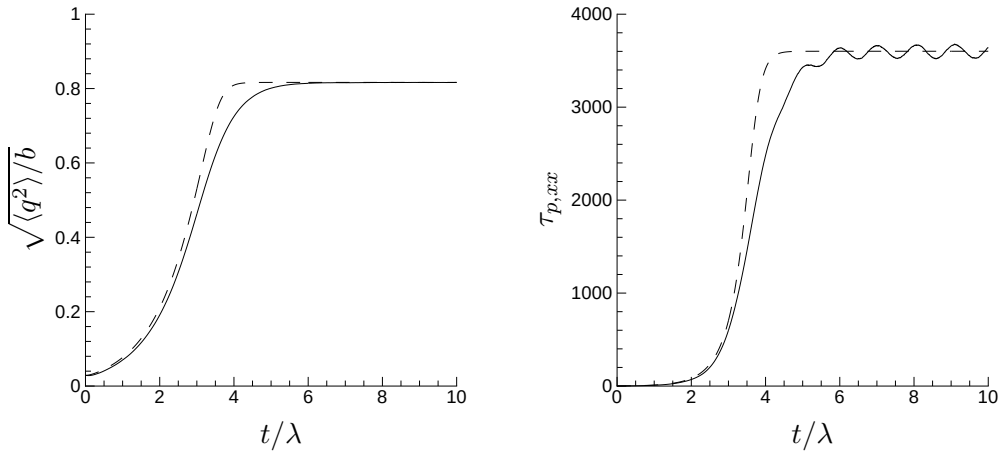

(a) Extension (b) Stress

Figure 5.5: Normalized extension (a) and stress (b) for a flow $Wi = 3$ with $Q = 0.5$, $R = 1.25$ and $D = 10.67$, corresponding to the eigenvalues $\sigma_{1,2} = 0.5 \pm \mathrm{i}$ and $\sigma_3 = -1$; FENE: ——, FENE-P: – – –.

with the tensor invariants Q and R given by

$$Q = -\frac{1}{2}\mathrm{tr}\left((\nabla \boldsymbol{u})^2\right), \tag{5.3}$$

$$R = -\det(\nabla \boldsymbol{u}). \tag{5.4}$$

The nature of the eigenvalues is determined by the discriminant, $D = (27/4)R^2 + Q^3$. $D > 0$ gives rise to one real and two complex-conjugate eigenvalues, $D < 0$ gives three real distinct eigenvalues, and $D = 0$ corresponds to three real eigenvalues, of which two are equal. A further classification can be made according to the values of Q and R (see Fig. 2 in Blackburn *et al.* (1996)), e.g. , Q measures the difference between rotation and strain of the local flow. One can think of the imaginary part of the eigenvalues as a measure of the local rotational character of the flow, whereas the real part quantifies its extensional character, i.e., a negative/positive real part indicates respectively a compression/extension in the corresponding direction. Note that this classification does not give any information on the axis of extension/compression or on the planes of rotation, which are in general not orthogonal.

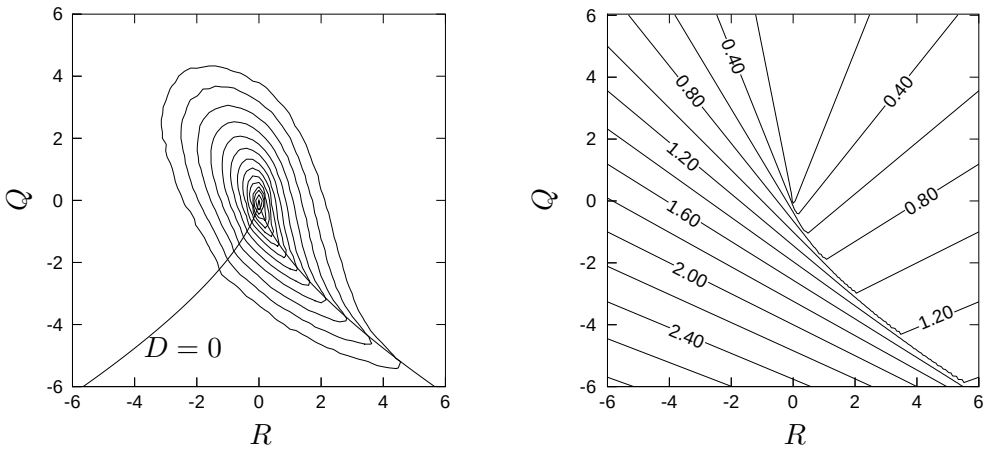

(a) (b)

Figure 5.6: (a) PDF plots of Q *vs.* R in the buffer layer (exponential scale from $3.5 \cdot 10^{-5}$ to 0.16); (b) isosurfaces of σ^* as a function of Q and R.

It was postulated that the coil-stretch transition of a polymer molecule in a three-dimensional steady flow is determined by the positive real eigenvalues of the velocity gradient tensor (de Gennes, 1974). However, because the sum of the eigenvalues vanishes in an incompressible flow due to the continuity condition, a compression axis/plane is always associated with an extension plane/axis. Thus, in the case of $D > 0$, even if the real eigenvalue is negative (compression), the real part of the two other complex conjugate eigenvalues is positive. Therefore, the motion induced by these complex eigenvalues involves both rotation from their imaginary parts and an extensional character dictated by their real parts. It follows that a flow with $D > 0$ and $R > 0$ in a (Q, R) plot (implying a negative real eigenvalue and two complex-conjugate eigenvalues with positive real parts) will unravel the polymer molecule at a sufficiently high Weissenberg number, as illustrated in Fig. 5.5. In this particular case, the stretching does not occur along a specific direction but in the rotation plane associated with the complex-conjugate eigenvalues. This phenomenon is well illustrated in Fig. 5.5 (b) where the stress computed with the FENE model shows an oscillating behavior, characteristic of the rotation of the polymer molecules. It should be noticed though, that this oscillating behavior is only visible if a small number of particles are used (here $N_p = 2000$). When a large number of particles is used, this behavior is

averaged out.

This shows that the stretching of the polymer is driven by the extensional character of the flow quantified by the positive real part of the eigenvalues. From this topological analysis, one can conclude that a polymer molecule will only fully unravel if it experiences a flow with a strong extensional character, i.e., one of the eigenvalues of the local velocity gradient tensor has a large positive real part. Accordingly, we introduce

$$\sigma^* \equiv \max_i \left(\mathrm{Re}(\sigma_i)\right), \tag{5.5}$$

as a measure of the ability of the flow to stretch the polymer molecule.

A similar analysis for the two-dimensional case has already been proposed by Hur *et al.* (2002), who examined the percentage of straining relative to the vorticity. According to this analysis, a shear flow can be seen as a limiting case, since it does not show a real coil-stretch transition but rather a tumbling dynamic as demonstrated by Smith *et al.* (1999) and Hur *et al.* (2001*b*). This tumbling is caused by the Brownian motion, which displaces extended molecules out of the extensional axis toward the compression axis, leading to a recoil of the molecule. Such tumbling dynamics can also be expected in a three dimensional case when the compression and extension axes are very close to each other.

These previous considerations are only based on the start-up of steady flows. In a turbulent flow, the velocity gradient tensor constantly changes with time, so that the application of the above analysis becomes more complicated. Not only the flow type is important but also its duration. Even a strong flow will not unravel a polymer molecule if it does not last long enough. Therefore, these considerations motivate the analysis of the flow topologies in a turbulent channel flow. Blackburn *et al.* (1996) have shown that the joint probability distribution function of Q and R has a characteristic teardrop shape (see Fig. 5.6 (*a*)). The isovalues of σ^* calculated from Eq. 5.2 are shown in Fig. 5.6 (*b*). Combining these two plots indicates that strong events, i.e., large σ^*, are most likely to correspond to positive R, negative Q and negative D, i.e., biaxial extension (Terrapon *et al.*, 2004).

5.3 Conditional statistics

The stretching mechanisms of polymer molecules are investigated through statistics conditioned on the polymer extension. In particular, statistics are gathered for particles whose dimensionless extension $q/\sqrt{b}$ crosses a given threshold r, which is referred to as a burst of

extension. For each of these particles, different flow and polymer quantities are averaged over a period of three time units before crossing the threshold, during the burst and for three more time units after the burst (Terrapon *et al.*, 2004).

In order to generalize the findings, Newtonian and viscoelastic flows are investigated. Since the Lagrangian method developed for coupled calculations is limited by the creation and destruction of particles, the viscoelastic flows are computed using the Eulerian approach (Dubief and Lele, 2001; Dubief, 2002, 2003) in which $N_p = 10^5$ particles are tracked. In particular, a $\pi h \times 2h \times h$ channel flow at $Re = 7500$ is investigated on a $64 \times 129 \times 32$ grid. Two different cases were computed for the viscoelastic cases, i.e., a low drag reduction regime (LDR), for which $b = 10000$ and $Wi = 3$, and a high drag reduction regime (HDR) with $b = 3600$ and $Wi = 7$. In the Newtonian case, the Reynolds number in wall units was $Re^+ = u_\tau h/\nu = 318$, while for the viscoelastic case $Re^+ = 233$ and $Re^+ = 181$, corresponding respectively to drag reductions of approximatively 46% and 67%. The mean velocity profile is shown in Fig. 5.7(a), where one can see the parallel shift of the log-law in the LDR case and the change of slope of the log-law in the HDR case. The velocity fluctuations shown in Fig. 5.7(b) reproduce the qualitative behavior of drag reduced flows with an increase of the streamwise fluctuations and a decrease of the wall-normal and spanwise fluctuations.

The choice of the threshold is somehow arbitrary; it was chosen to isolate the tail of the distribution of extensions. The percentage of particles being on average above the threshold is summarized in tables 5.1-5.3. Because the duration of a burst of extension varies for each polymer molecule, statistics gathered for each particle during a burst are normalized by their burst time, which is given in tables 5.1-5.3. The tables also report the streamwise distance traveled by the particles during the three time units before the burst and during the burst, as well as the strain Γ experienced before and during the burst, where the strain is defined respectively for the FENE-P and FENE models as

$$\Gamma = \int_{t_0}^{t_1} \frac{1}{2} \frac{\langle q_i q_j \rangle}{\langle q_k q_k \rangle} \left(\frac{\partial u_i}{\partial x_j} + \frac{\partial u_j}{\partial x_i} \right) \mathrm{d}t, \tag{5.6}$$

$$\Gamma = \int_{t_0}^{t_1} \frac{1}{2} \frac{q_i q_j}{q^2} \left(\frac{\partial u_i}{\partial x_j} + \frac{\partial u_j}{\partial x_i} \right) \mathrm{d}t. \tag{5.7}$$

As expected, the burst time decreases with increasing threshold and therefore, the streamwise distance traveled by the particles during the burst decreases as well. On the other

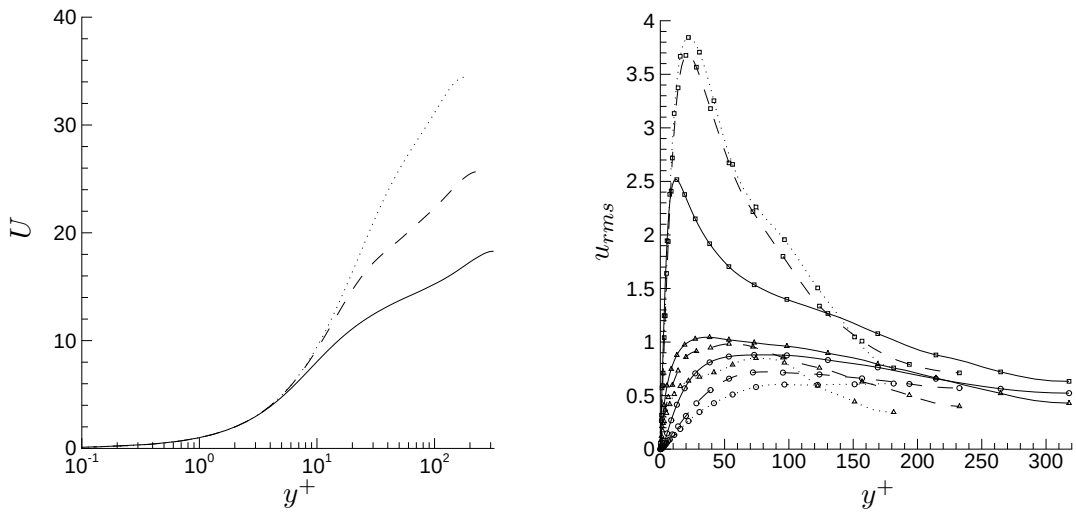

(a) (b)

Figure 5.7: Mean velocity profile (a) and velocity rms (b) for $DR = 0\%$ (——), $DR = 46\%$ (– – –) and $DR = 67\%$ (· · · ·). Streamwise: □, spanwise: △, wall-normal: ○.

hand the distance traveled before the burst remains constant since the time is maintained constant. The strain is responsible for extending the polymer molecules, thus the amount of strain experienced by the particles increases with the threshold. It is interesting to notice that when the strain experienced during a burst is multiplied by the corresponding Weissenberg number Wi, it then depends only on the threshold r and not on the flow itself. In other words, the strain in polymer time unit needed to maintain the polymer molecule extension above a threshold value r is only a function of r.

Figure 5.8 shows the dimensionless mean-square extension of the particles crossing the threshold value r before, during and after the burst for the three different flows investigated. One can observe that the polymer reaches its maximum extension in the early phase of the burst and then contracts slowly until crossing the threshold in the other direction to reach again a coiled state. As stated in the previous section, σ^* can be used to quantify the extensional character of the flow. Figure 5.9 illustrates this mechanism, where the particles experience a maximum value of σ^* shortly before crossing the threshold. However, during the burst, σ^* decreases constantly to reach a steady value after the burst. It is interesting to notice that the maximum value of σ^* experienced before the burst happens much earlier

Table 5.1: Newtonian flow.

r	0.65	0.75	0.85	0.95
$n > r \quad (\%)$	5.9	3.2	1.0	0.02
$\langle t \rangle_{\text{burst}}$	2.63	1.78	1.03	0.46
$\langle x \rangle_{\text{before burst}}$	1.37	1.33	1.31	1.42
$\langle x \rangle_{\text{burst}}$	1.15	0.81	0.49	0.21
$\langle \Gamma \rangle_{\text{before burst}}$	1.22	1.40	1.65	2.13
$\langle \Gamma \rangle_{\text{burst}}$	0.37	0.49	0.74	1.99
$Wi\langle \Gamma \rangle_{\text{burst}}$	1.11	1.47	2.22	5.97

Table 5.2: Viscoelastic flow (LDR).

r	0.45	0.55	0.65	0.75
$n > r \quad (\%)$	0.20	0.07	0.025	0.006
$\langle t \rangle_{\text{burst}}$	4.31	3.4	2.51	1.61
$\langle x \rangle_{\text{before burst}}$	1.27	1.29	1.31	1.29
$\langle x \rangle_{\text{burst}}$	1.84	1.48	1.10	0.69
$\langle \Gamma \rangle_{\text{before burst}}$	1.20	1.33	1.49	1.69
$\langle \Gamma \rangle_{\text{burst}}$	0.22	0.26	0.32	0.43
$Wi\langle \Gamma \rangle_{\text{burst}}$	0.66	0.78	0.96	1.29

Table 5.3: Viscoelastic flow (HDR).

r	0.55	0.65	0.75	0.85
$n > r \quad (\%)$	2.3	1.03	0.42	0.11
$\langle t \rangle_{\text{burst}}$	9.0	5.63	3.58	1.90
$\langle x \rangle_{\text{before burst}}$	1.42	1.41	1.42	1.35
$\langle x \rangle_{\text{burst}}$	3.87	2.63	1.72	0.90
$\langle \Gamma \rangle_{\text{before burst}}$	0.63	0.72	0.85	1.03
$\langle \Gamma \rangle_{\text{burst}}$	0.12	0.15	0.21	0.32
$Wi\langle \Gamma \rangle_{\text{burst}}$	0.84	1.05	1.47	2.24

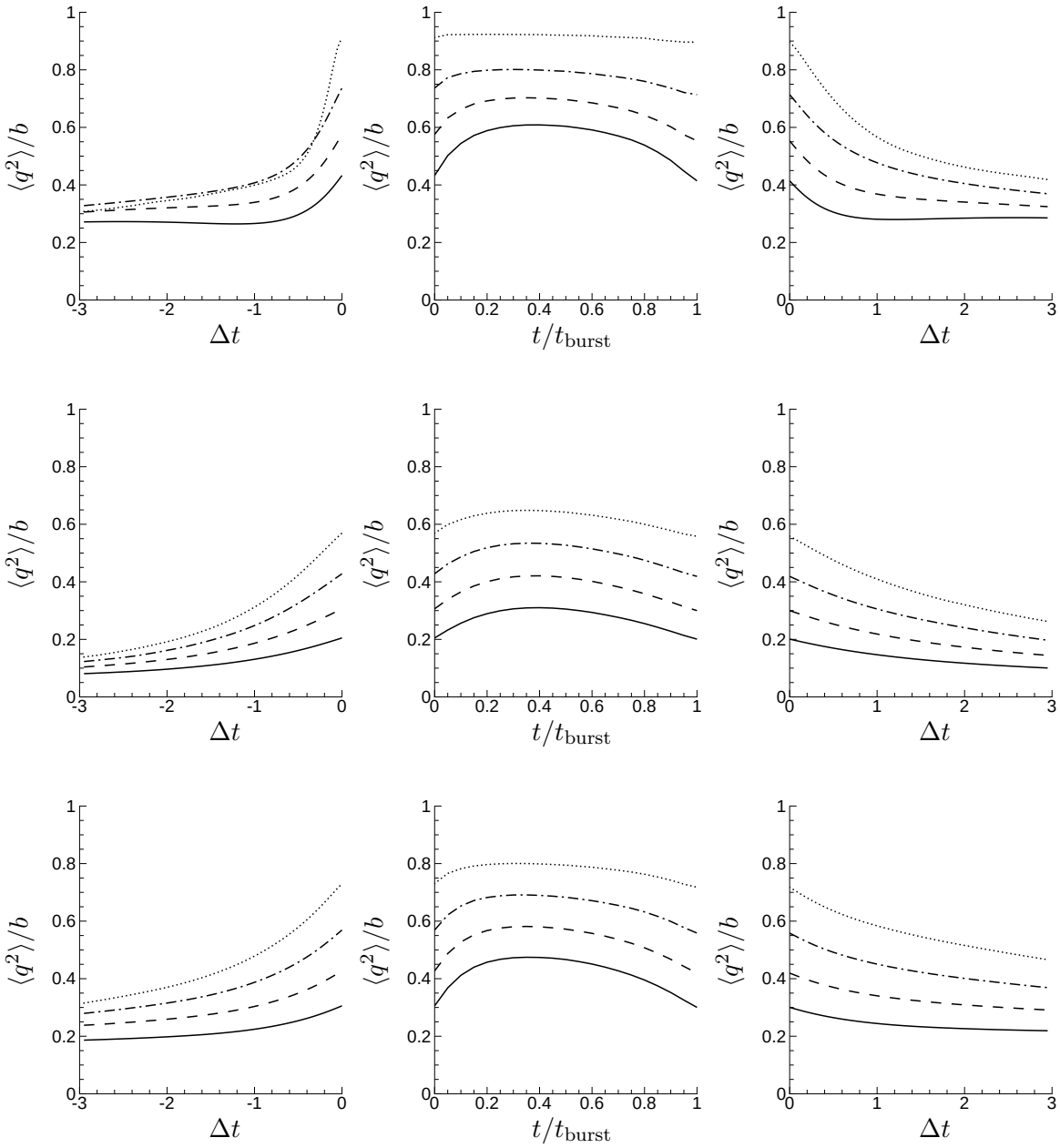

Figure 5.8: Conditional average of the mean square extension q^2/b for the polymer molecules crossing the threshold value $q/\sqrt{b} = r$ as a function of the time, Δt, before the burst (left column), during the burst (middle column) and after the burst (right column). Top row: $DR = 0\%$, $r = 0.65$: ——; $r = 0.75$: – – –; $r = 0.85$: —·—; $r = 0.95$: ····; middle row: $DR = 46\%$, $r = 0.45$: ——; $r = 0.55$: – – –; $r = 0.65$: —·—; $r = 0.75$: ····; bottom row: $DR = 67\%$, $r = 0.55$: ——; $r = 0.65$: – – –; $r = 0.75$: —·—; $r = 0.85$: ····.

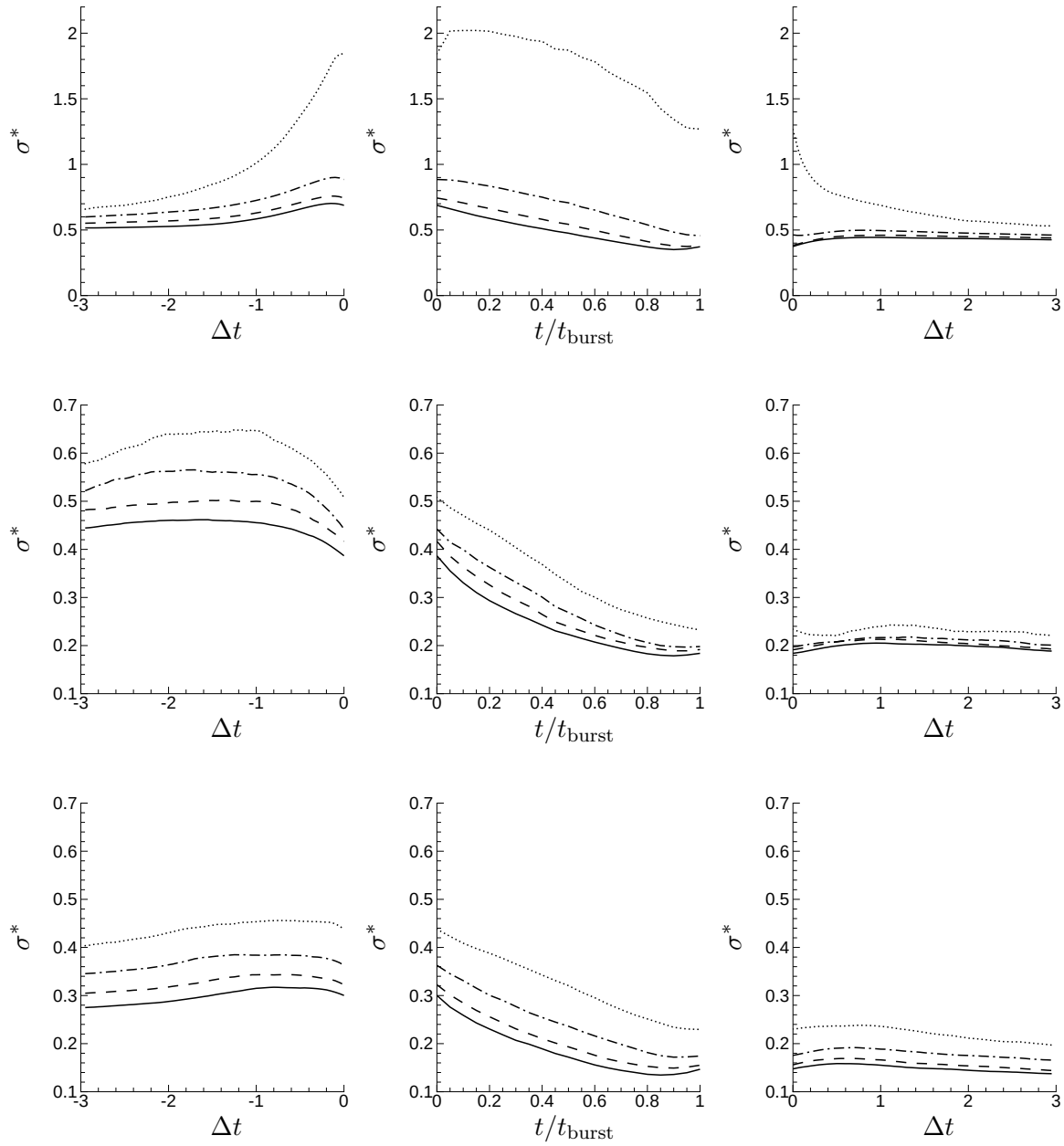

Figure 5.9: Conditional average of σ^* for the polymer molecules crossing the threshold value $q/\sqrt{b} = r$ as a function of the time, Δt, before the burst (left column), during the burst (middle column) and after the burst (right column). Same labeling as in Fig. 5.8.

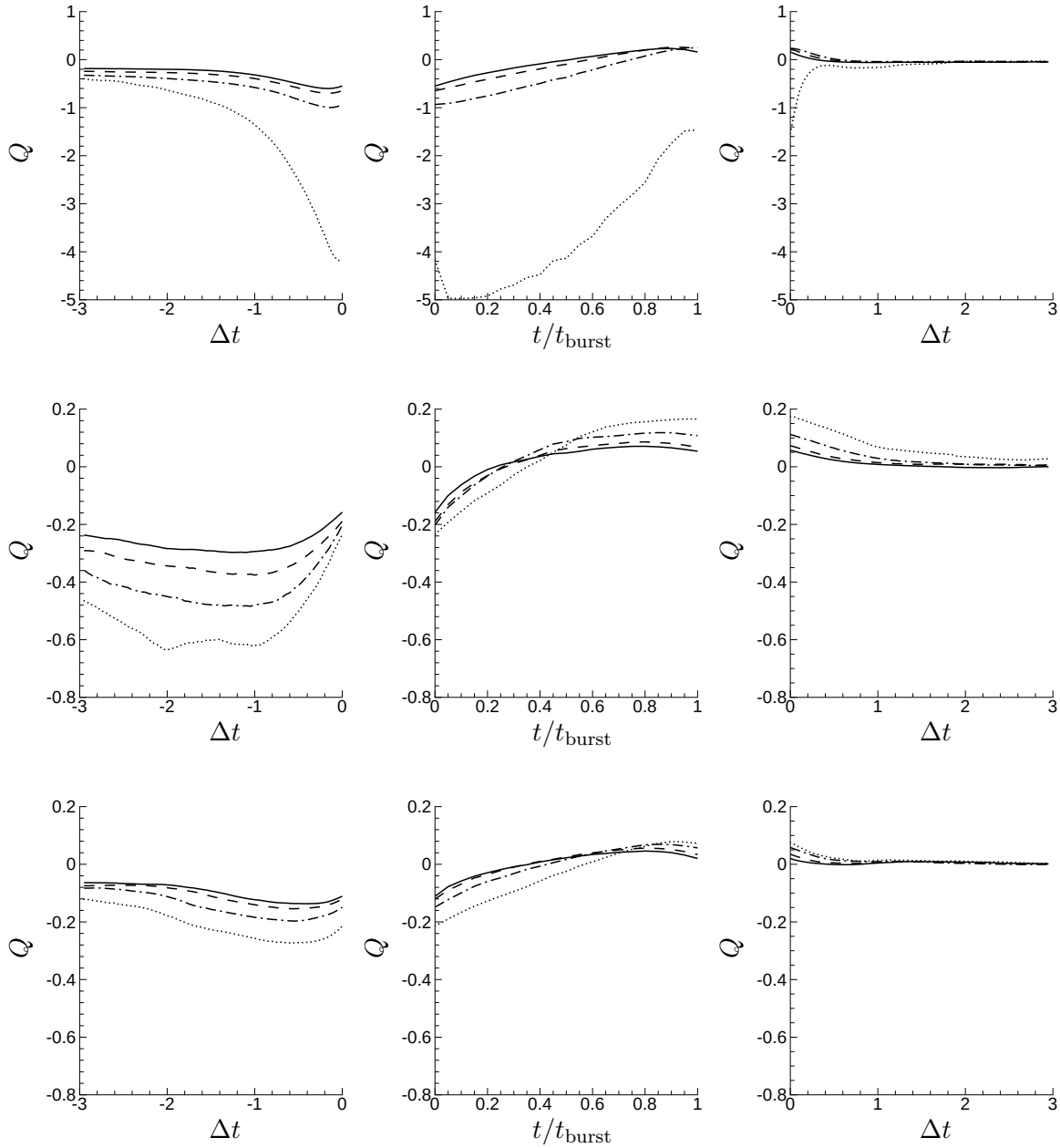

Figure 5.10: Conditional average of Q for the polymer molecules crossing the threshold value $q/\sqrt{b} = r$ as a function of the time, Δt, before the burst (left column), during the burst (middle column) and after the burst (right column). Same labeling as in Fig. 5.8.

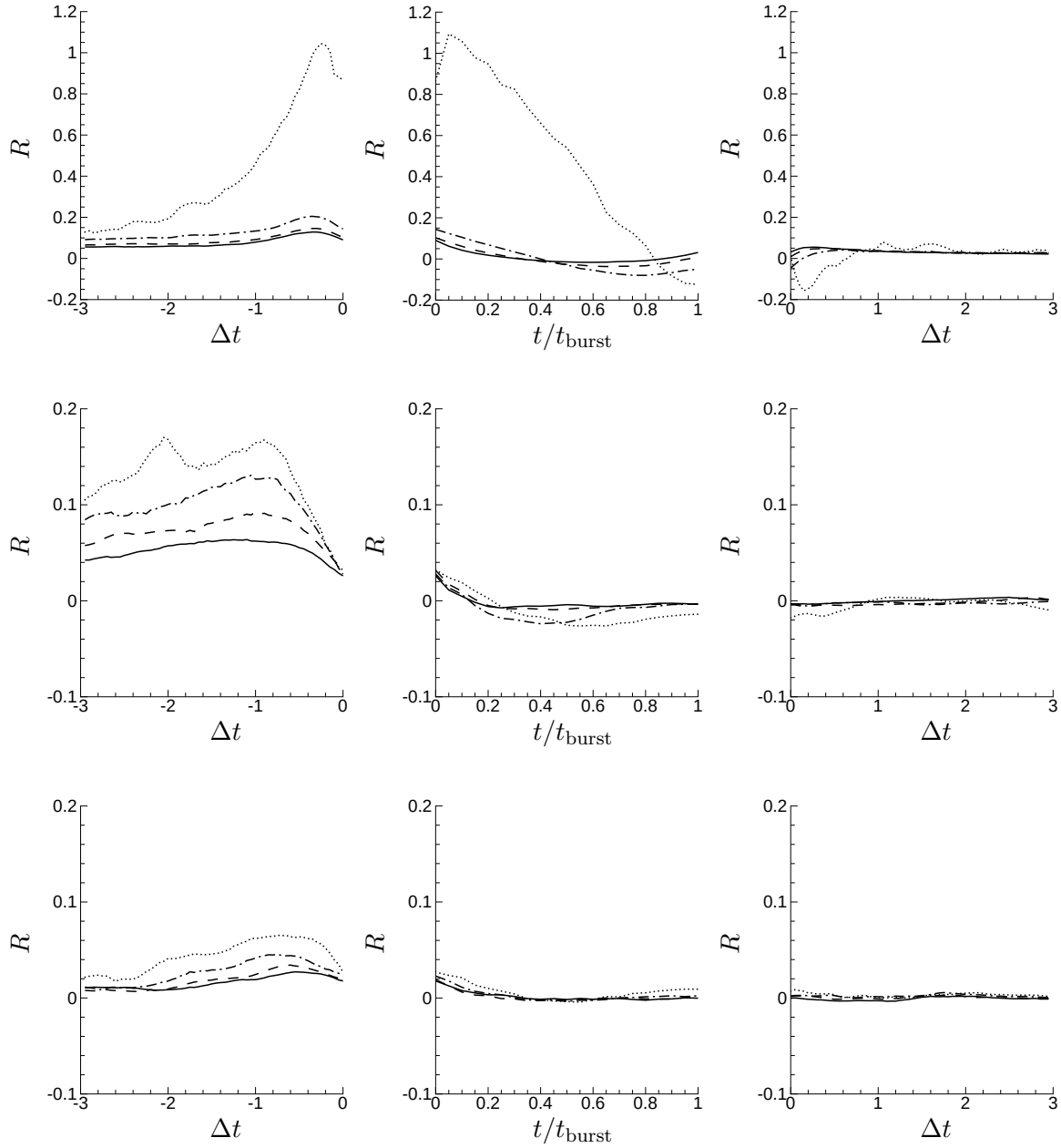

Figure 5.11: Conditional average of R for the polymer molecules crossing the threshold value $q/\sqrt{b} = r$ as a function of the time, Δt, before the burst (left column), during the burst (middle column) and after the burst (right column). Same labeling as in Fig. 5.8.

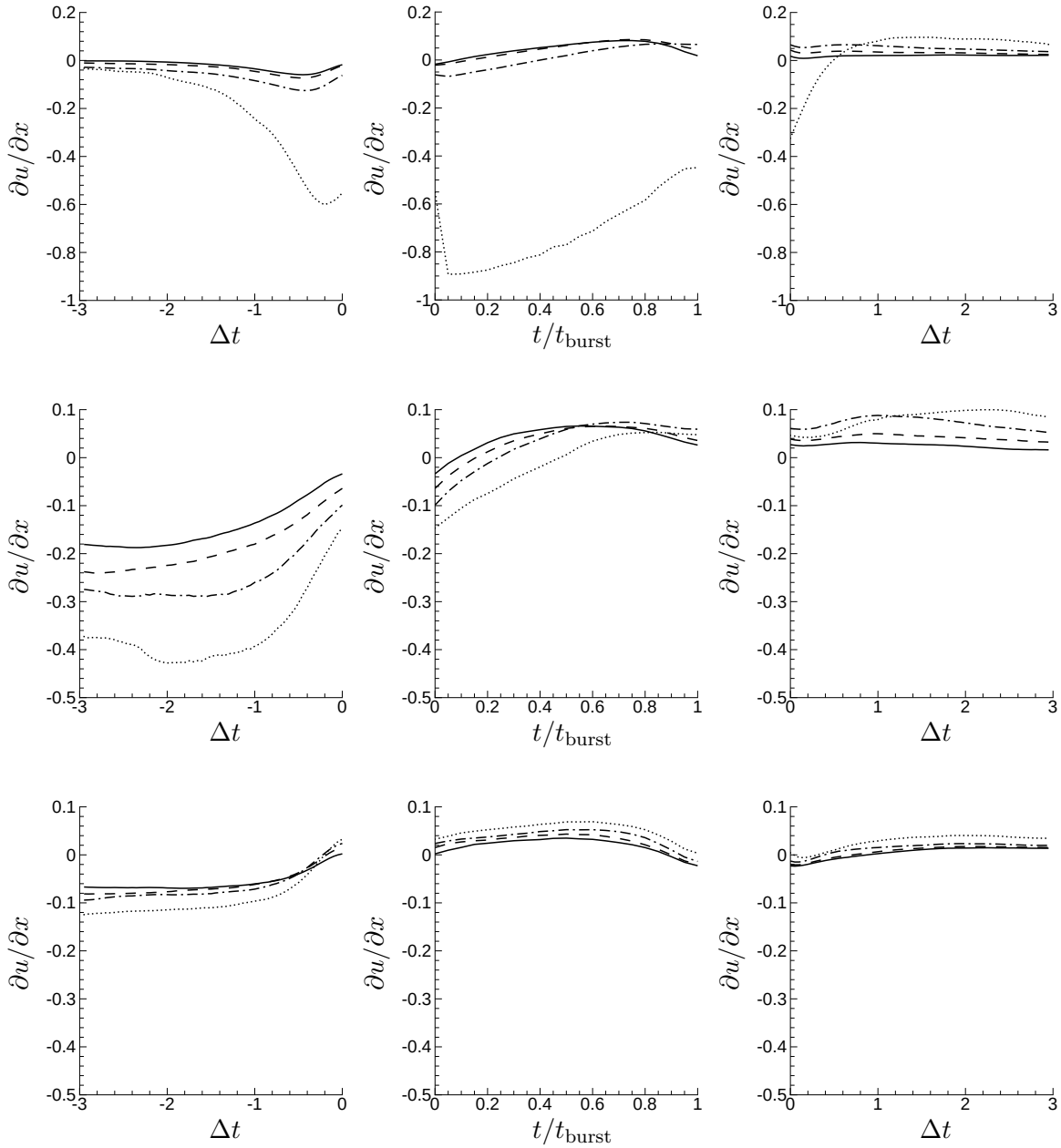

Figure 5.12: Conditional average of the velocity gradient $\partial u/\partial x$ for the polymer molecules crossing the threshold value $q/\sqrt{b} = r$ as a function of the time, Δt, before the burst (left column), during the burst (middle column) and after the burst (right column). Same labeling as in Fig. 5.8.

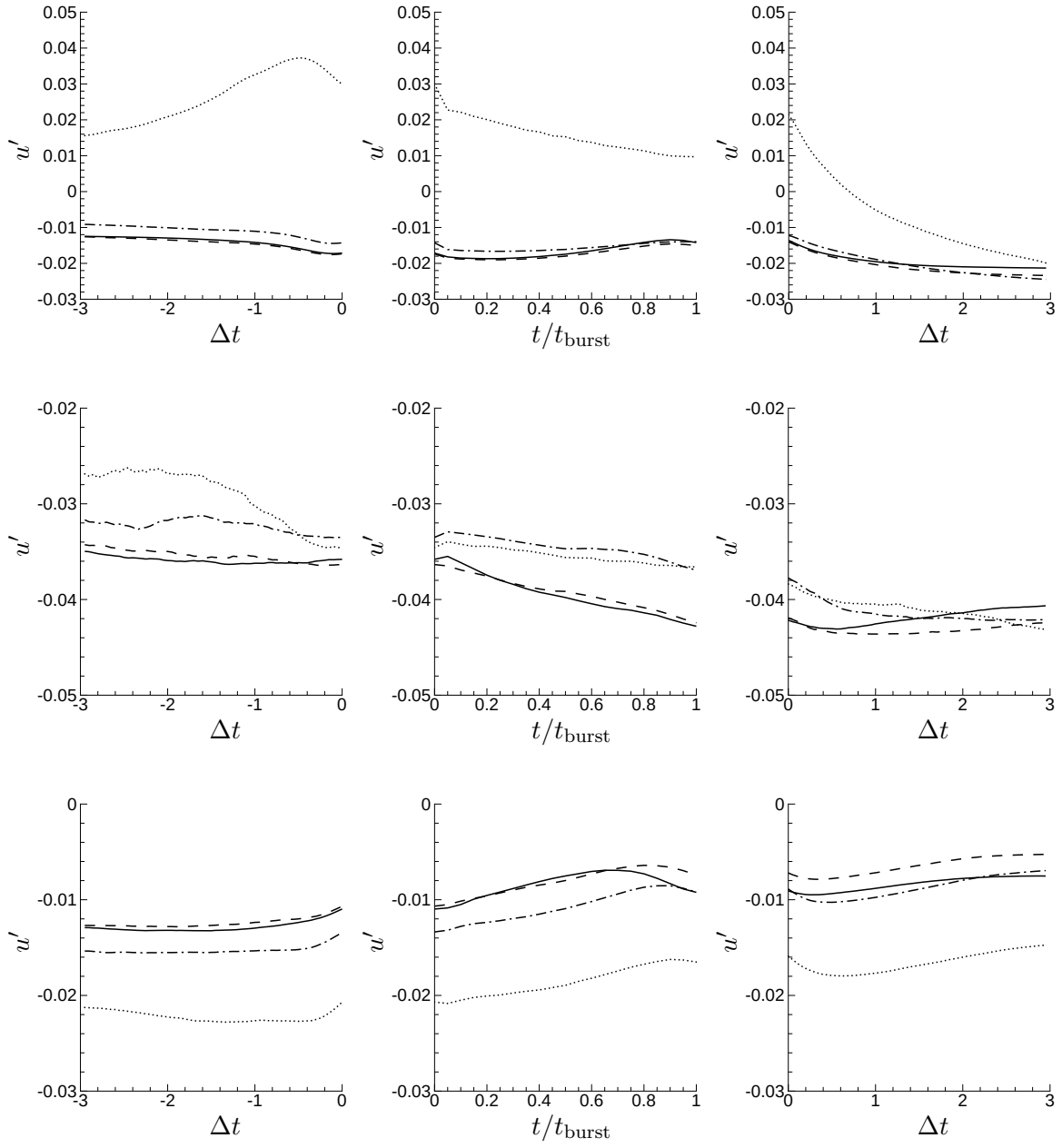

Figure 5.13: Conditional average of the streamwise velocity fluctuation, u', for the polymer molecules crossing the threshold value $q/\sqrt{b} = r$ as a function of the time, Δt, before the burst (left column), during the burst (middle column) and after the burst (right column). Same labeling as in Fig. 5.8.

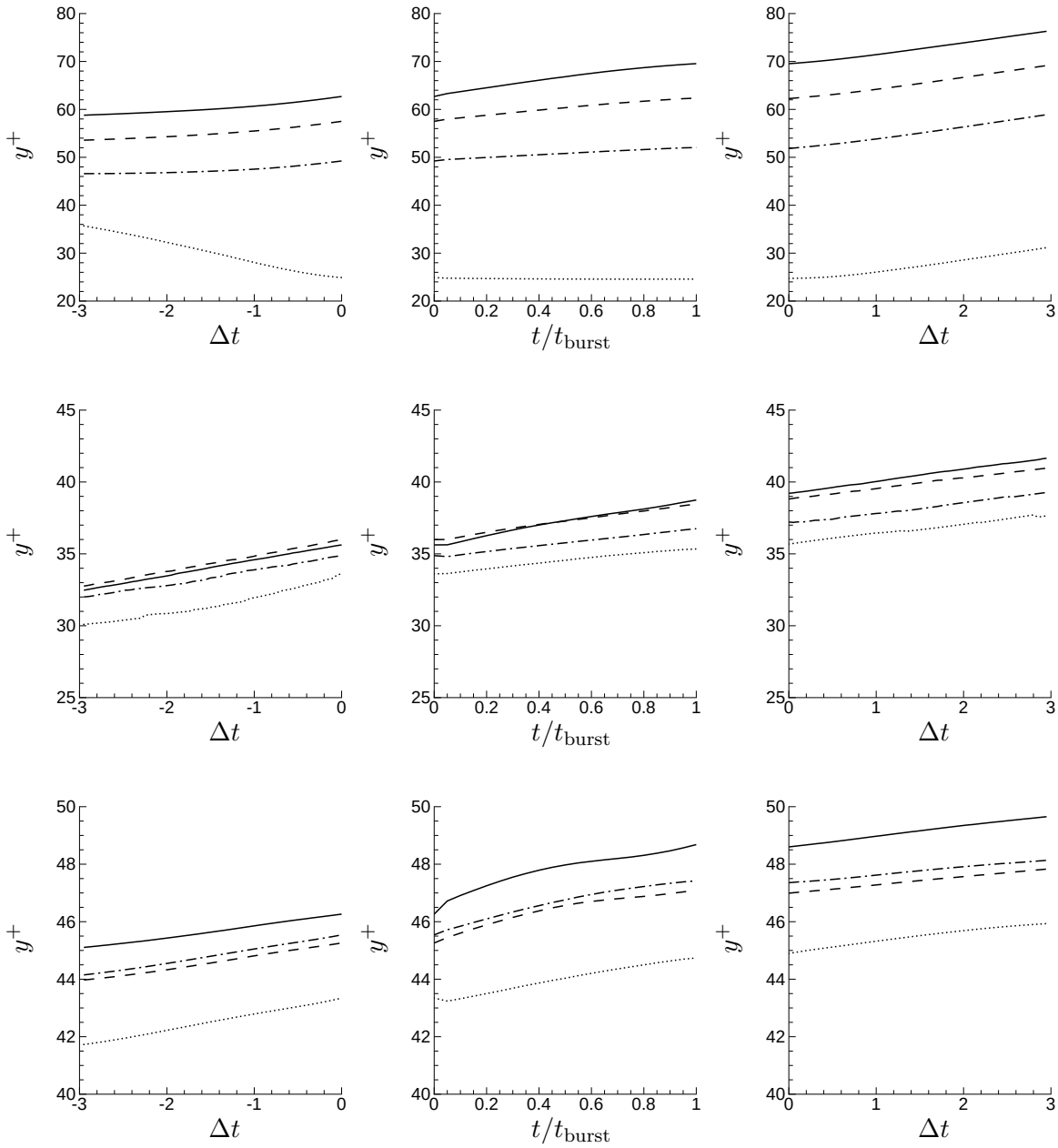

Figure 5.14: Conditional average of the distance from the wall, y^+, for the polymer molecules crossing the threshold value $q/\sqrt{b} = r$ as a function of the time, Δt, before the burst (left column), during the burst (middle column) and after the burst (right column). Same labeling as in Fig. 5.8.

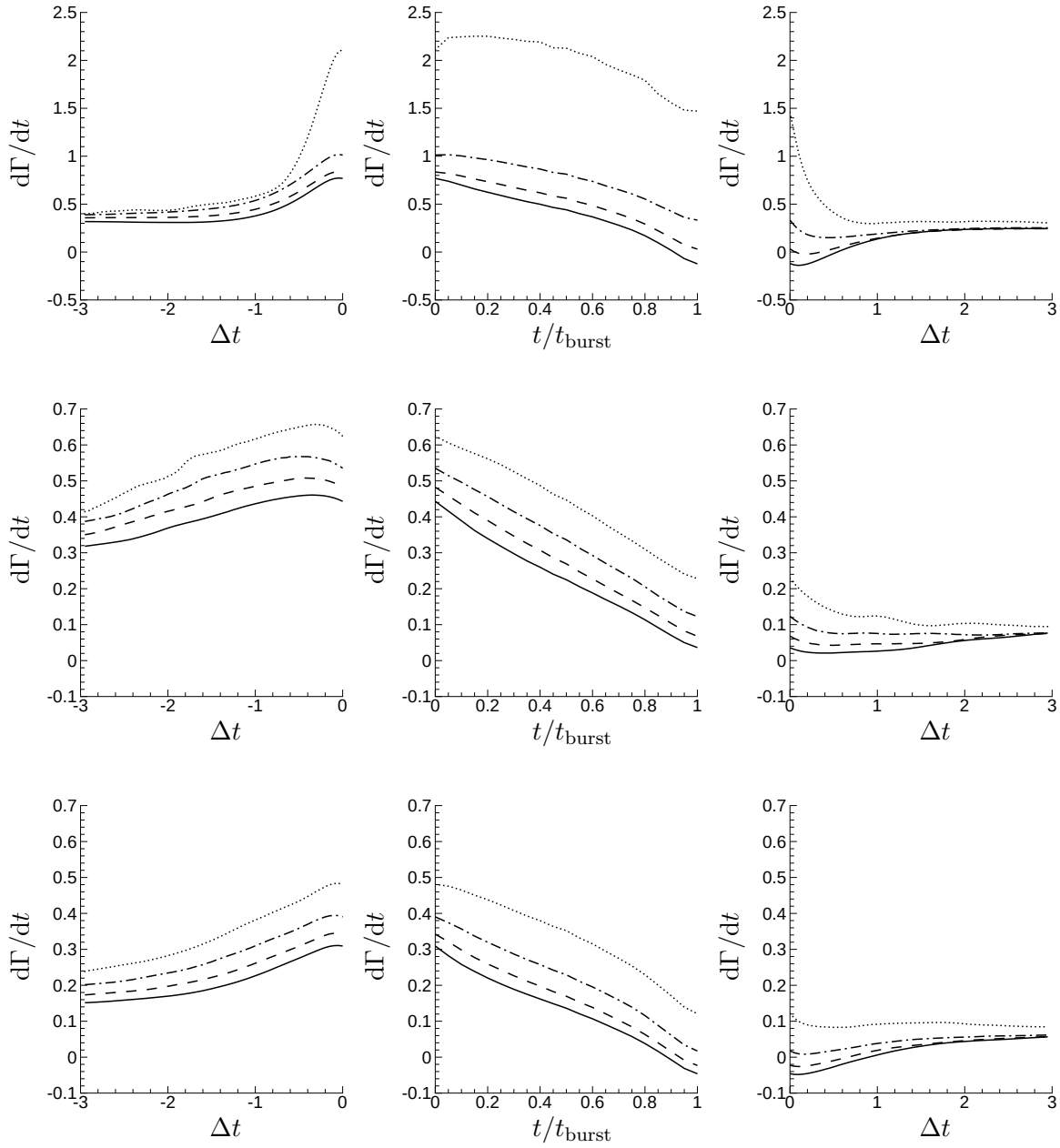

Figure 5.15: Conditional average of the strain rate $\mathrm{d}\Gamma/\mathrm{d}t$ for the polymer molecules crossing the threshold value $q/\sqrt{b} = r$ as a function of the time, Δt, before the burst (left column), during the burst (middle column) and after the burst (right column). Same labeling as in Fig. 5.8.

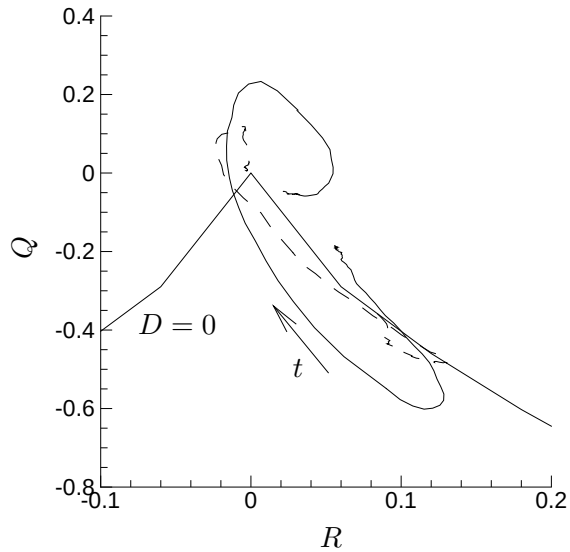

Figure 5.16: Mean time evolution of Q vs. R before, during and after the burst in a Newtonian (——) and viscoelastic flow at LDR (– – –) for a threshold $r = 0.65$. The line $D = 0$ is also shown for comparison.

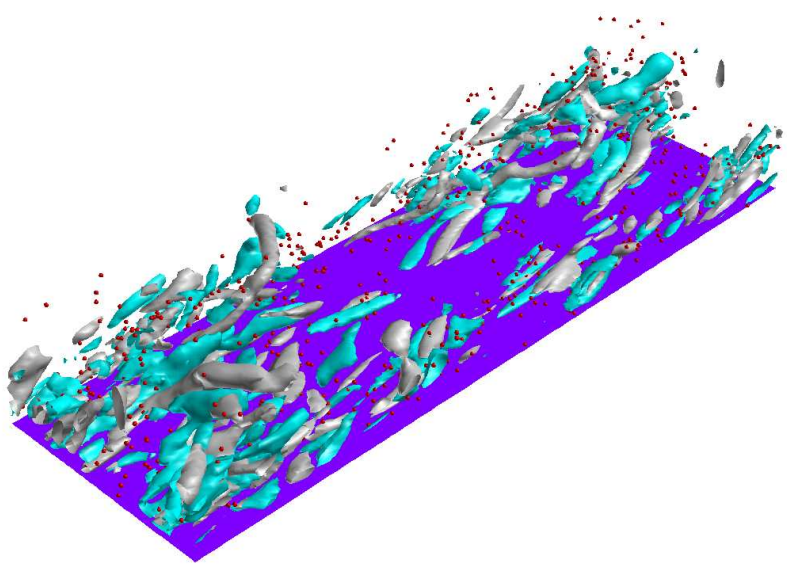

Figure 5.17: Instantaneous view of the lower half of the channel showing the isosurface $Q = 1.9$ (grey) representing the vortices, the isosurface (turquoise) of $\sigma^* = 1.6$ and the polymer molecules (red) with $q/\sqrt{b} > 0.8$ at $Wi = 3$ in a Newtonian flow.

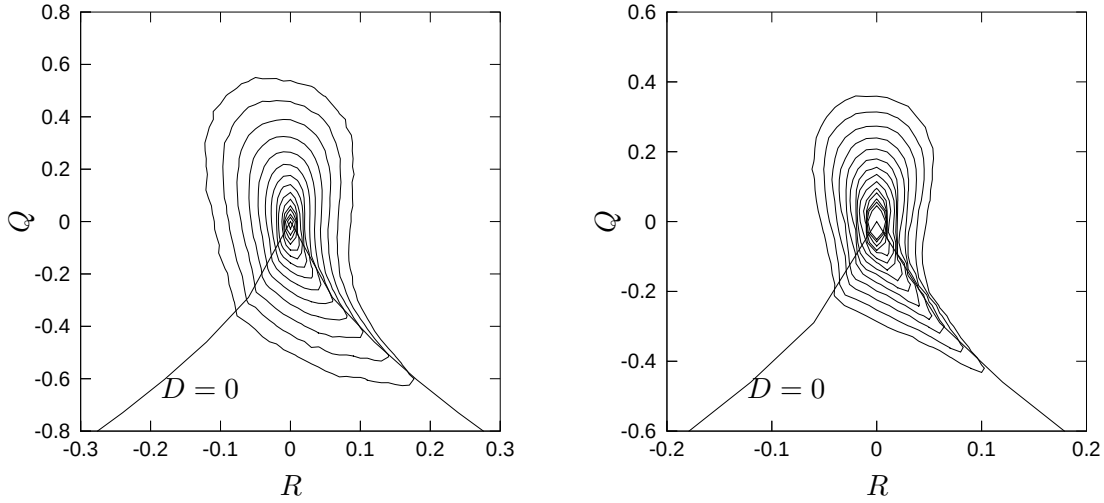

(a) LDR

(b) HDR

Figure 5.18: JPDF of the invariants Q and R.

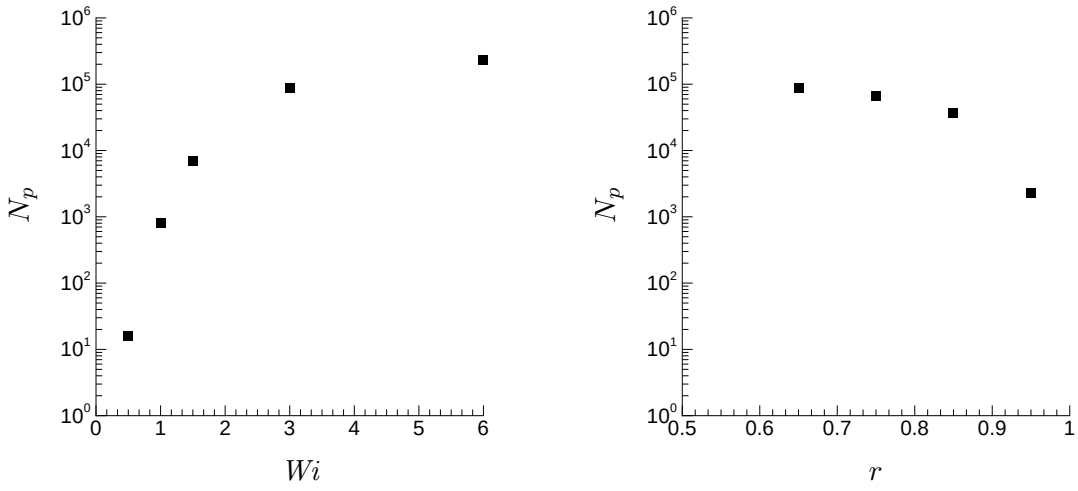

(a) $r = 0.65$

(b) $Wi = 3.0$

Figure 5.19: Number of particles N_p having crossed the threshold r in a Newtonian flow.

for the LDR case, i.e. at about one time unit before crossing the threshold while for the two other cases, the maximum is reached just before the beginning of the burst. This could be explained by the fact that the number of particles used for the statistics in the LDR cases is much lower than for the two other cases. As expected, the value of σ^* increases with the threshold. Therefore, one can conclude that only rare, strong events, i.e. large σ^*, can produce a large stretching of the polymer molecule at low Wi; at high Wi weaker events are needed but a large σ^* is more efficient and achieves a larger extension of the polymer molecule.

The average of the invariants Q and R of the velocity gradient tensor are showed in Fig. 5.10 and 5.11. One can observe a similar behaviour to the one described above; particles experience an extremum of negative Q and positive R before the burst, then a decrease during the burst to finally reach a steady value around zero after the burst. This implies that the particles have experienced, on average, a biaxial extensional flow, which is stronger for larger threshold values r. These results are in agreement with Fig. 5.6, which shows that the largest eigenvalues are rare events found at negative Q. It is also found that these events are in general characterized by a negative velocity gradient $\partial u/\partial x$, a negative streamwise velocity fluctuation, u', and a positive wall-normal velocity fluctuation, v', as illustrated in Fig. 5.12, 5.13 and 5.14. It can therefore be deduced that these strong events are correlated with ejections of low-speed fluid away from the wall. The predominance of ejection events versus sweeps can be understood by the fact that the polymer molecules experience a pre-stretching by the shear at the wall. Figure 5.16 shows the trajectory of the polymer molecules in a (Q, R) plot parametrized by the time before, during and after the burst. While the flow is very different between the Newtonian and viscoelastic case, the shape of the trajectory looks similar. The particles experience first some straining going towards negative Q and positive R until they reach an extremum in σ^* shortly before crossing the threshold. Then they move back towards positive Q and negative R. Finally, during the relaxation, the particles reach a positive Q and tend towards a simple shear flow.

The generality of these results has been demonstrated by Terrapon *et al.* (2004) who used also the FENE model and a bead-spring chain model with $N_b = 11$ beads to conduct similar statistical studies. They showed that the results were independent of the model used.

Dubief and Delcayre (2000) showed that vortices can be detected by positive isosurfaces of Q, where Q can also be computed as the difference between vorticity Ω and straining S.

It is therefore interesting to note that polymer stretching is associated with negative values of Q, i.e., straining, whereas vortices are associated with positive values, i.e., rotation. Flow visualizations also demonstrate that the regions of large σ^* are always located next to the vortices and can also be seen as structures advected by the mean flow. This is illustrated in figure 5.17, which shows isosurfaces of Q representing the vortices, isosurfaces of σ^* and the polymer molecules, which are highly stretched. The correlation between σ^* and the vortices is striking and can provide new insight into the mechanisms of polymer drag reduction. Dubief *et al.* (2004*b*) have shown by continuum calculations that polymers act on vortices by damping them. From the present results, it seems clear that the polymer is first stretched in these regions of large σ^* that are associated with the vortices, and then coil-back in the regions of positive Q corresponding to the vortices (see Fig. 5.10).

Since in a viscoelastic flow the polymer molecules significantly modify the fluctuations of the turbulent velocity field, it can be surprising that the stretching mechanisms of polymers are similar to those in a Newtonian flow. However, the analysis of the topology of viscoelastic flows shows the same teardrop-like shape of the joint probability distribution function of the velocity gradient tensor invariants Q and R, as illustrated in Fig. 5.18. The main difference between Newtonian and drag reduced flows lies in the magnitude of Q and R and in the more symmetric upper part ($Q > 0$) of the distribution in the drag reduced case. Therefore, the only events which are strong enough to unravel the polymers correspond to biaxial extensional flows.

In terms of the onset of drag reduction, only very strong events can stretch the polymers at very low values of Wi. It is not obvious that a coil-stretch transition is necessary for the polymers to reduce drag, but a sufficiently large extension is needed to produce stress. Bird *et al.* (1987) showed that the inequality $Wi \cdot \sigma > 0.5$ must be satisfied for a coil-stretch transition to occur. This gives an absolute lower bound for the Weissenberg number, $Wi_{cr} = 0.5\sigma^*_{max}$, below which no molecule can unravel. Assuming that drag reduction scales nearly linearly with the number of polymers stretching, one would see an important increase of drag reduction near what is apparently a critical Wi, since the number of molecules achieving a coil-stretch transition increases dramatically with Wi around this critical value (as illustrated in figure 5.19). This dramatic increase of the number of stretched molecules can be understood by the distribution of flow types shown in figure 5.6 (*a*), where the probability of finding weaker events increases exponentially.

Chapter 6

Coupled flow and polymer calculations

Our ultimate goal is to predict drag reduction. Therefore, the uncoupled simulations must be extended to integrate the effect of the polymer stresses into the flow. Many previous studies based on Eulerian approaches have demonstrated the ability to reproduce the characteristics of polymer drag reduction. However, all of these studies make use of numerical artifices like artificial diffusion to stabilize the computation. Lagrangian simulations provide an alternate approach to investigate the effect of these numerical artifices.

As a first step, the polymer stresses computed from both approaches are compared. Discrepancies between the two methods are analyzed and their impact on the amount of drag reduction is investigated in coupled simulations (section 6.2). Finally, a discussion of the results is presented in section 6.3.

6.1 Uncoupled simulations

For the comparison between different methods to be meaningful, it is important to compute the polymer stresses in an identical turbulent flow. Therefore, an uncoupled simulation is performed by setting the concentration parameter β in Eq. 2.51 to zero. The polymers have no effect on the flow and the polymer statistics should, therefore, be independent of the numerical method used.

A turbulent channel flow of size $10h \times 2h \times 5h$ at constant mass flowrate is investigated,

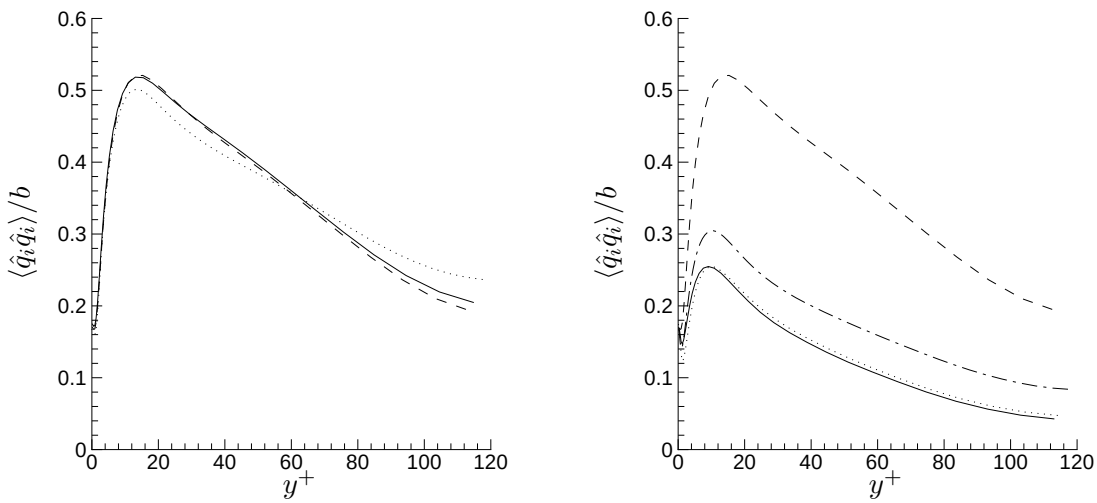

(a) (b)

Figure 6.1: Dimensionless polymer square extension in a Newtonian flow at $Re = 2760$. *a*) Eulerian calculation: $LAD = 0.1$ (——); $LAD = 10$ (– – –); $LAD = 0.1$ on a 128^3 grid (· · · ·). *b*) Lagrangian calculation without creation or destruction: $N_{\text{ini}} = 20$ (——); $N_{\text{ini}} = 10$ (· · · ·); $N_{\text{ini}} = 20$ on a 128^3 grid (– · –); Eulerian calculation: $LAD = 10$ (– – –).

where h is the half height of the channel. The domain is discretized on a $64 \times 65 \times 64$ non-uniform grid and the Reynolds number is $Re = 2760$, corresponding to $Re^+ = 125$. The Eulerian calculation is based on the method developed by Dubief and Lele (2001), while the Lagrangian computation relies on the algorithm described in section 3.4.2, where both methods proposed for the creation of particles are investigated. For the sake of simplicity and conciseness, the first method to create particles based on the mean polymer stress of the actual cell is denoted by $M(N_{\text{ini}}, N_{\text{min}}, N_{\text{max}})$ and the method based on the interpolation of the mean polymer stress from the adjacent cells is denoted by $I(N_{\text{ini}}, N_{\text{min}}, N_{\text{max}})$, where N_{ini} is the initial number of particles per grid cell at the start of the simulation and N_{min} and N_{max} are the minimum and maximum number of particles per grid cell at all times respectively. The polymer parameters are chosen to be $Wi = 7$ and $b = 10000$.

To illustrate the impact of the artificial diffusion used in the Eulerian approach, two different artificial diffusion coefficients, $LAD = 0.1$ and $LAD = 10$ are compared. The mean dimensionless square extension $\langle \hat{q}_i \hat{q}_i \rangle / b$ of the polymers as a function of the distance

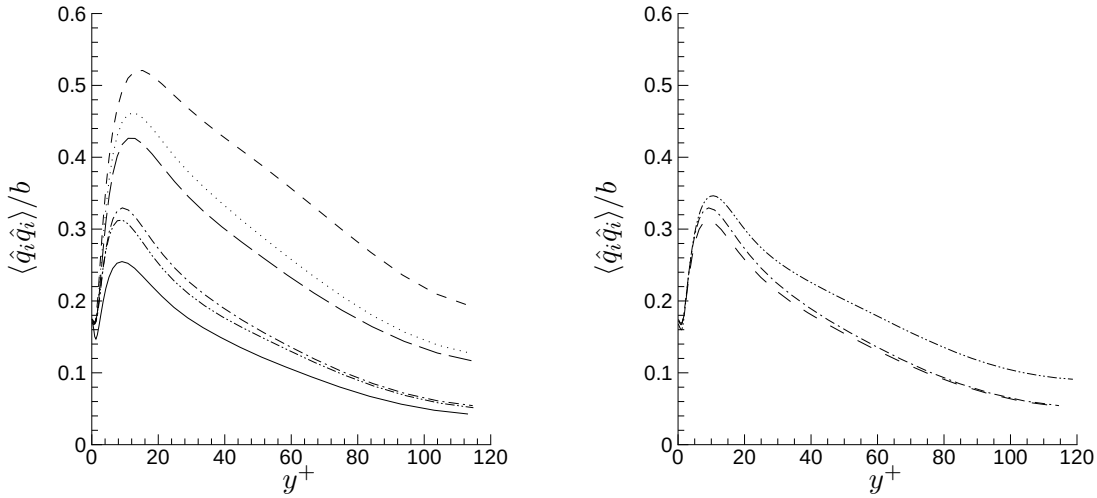

(a) (b)

Figure 6.2: Dimensionless polymer square extension in a Newtonian flow at $Re = 2760$. (a) Eulerian calculation: $LAD = 10$ (– – –). Lagrangian calculation: $I(18, 15, 21)$ ($\cdots$); $M(18, 15, 21)$ (——); $M(18, 8, 28)$ (– · –); $M(28, 8, 48)$ (– · · –); $M(20, 0, \infty)$ (——). (b) Lagrangian calculation $M(18, 8, 28)$: 64^3 grid (– · –); 128^3 grid (– · · –); $M'(18, 8, 28)$: (– – –).

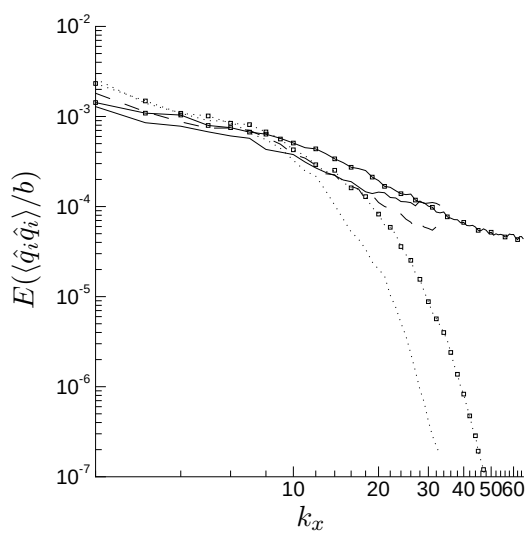

Figure 6.3: Spectrum of the dimensionless extension along the streamwise direction at $y^+ = 11$ in a Newtonian flow. Lagrangian $M(20, 0, \infty)$: ——; Lagrangian $M(18, 8, 28)$: – – –; Eulerian ($LAD = 0.1$): $\cdots$; symbols correspond to a 128^3 grid.

from the wall y^+ is shown in Fig. 6.1 (a). One can see that the two diffusion coefficients give very similar results. However, it is important to note that the artificial dissipation is local, i.e., it is used only where the conformation tensor loses its positive-definitiveness. As a consequence, a decrease of the diffusion coefficient increases the number of grid points affected by the artificial diffusion (in this case, from 1% to 15.5%). Therefore, it is impossible to conduct a systematic investigation of the impact of the artificial diffusion. Also shown on Fig 6.1 (a) are the results for a similar simulation computed on a refined mesh (128^3 grid points) and with a diffusion coefficient of 0.1. The solution is very similar to the one on the coarse mesh. It is also interesting to note that a refinement of the mesh does not decrease the number of grid points affected by the artificial dissipation. In fact, in this case 17% of the grid points are affected by it. This illustrates the difficulty of solving the FENE-P equations because of the small scales created by the nonlinear advection term.

The Lagrangian method was developed to overcome this difficulty, thus avoiding use of artificial dissipation. Fig. 6.1(b) compares the polymer extension computed with the Eulerian and Lagrangian methods, without creation or destruction of particles. The solutions are quantitatively very different, with the Lagrangian extension being smaller by a factor of two. The Lagrangian solution also shows no sensitivity on the total number of particles, as illustrated in Fig. 6.1(b). This indicates that the discrepancy between Eulerian and Lagrangian cannot be attributed to the lack of particle resolution. If the mesh is refined, a higher extension is observed, due to a better resolution of the velocity and velocity gradient fields. As mentioned in section 4.3, the creation and destruction of particles in the Lagrangian method induces some dissipation. Different cases of creation/destruction give very different results, as illustrated in Fig. 6.2(a). It is interesting to notice that the more dissipative the method is (according to the results found in section 4.3.5), the more is the extension. Fig. 6.2(b) also shows a higher extension for $M(18, 8, 28)$ when the mesh is refined. While all methods give the correct polymer extension at the wall, the solution away from the wall is strongly dependent on the numerical method, which is an undesirable characteristic for any numerical method.

In light of these results, it could be concluded that dissipation creates more extension, which is counter intuitive. Also, it was shown by Min *et al.* (2001) and Yu and Kawaguchi (2004) that Eulerian methods which are less dissipative produce more polymer extension. Moreover, it is not clear if the discrepancy between the different Lagrangian cases and between Lagrangian and Eulerian calculations can be attributed to the same cause. The

analysis of the power spectrum of the extension at $y^+ = 11$, corresponding to the peak value of extension (see Fig. 6.3), shows very different behaviour at small scales in the two approaches. The Eulerian spectrum shows the expected drop in the energy at small scales, which is due to the dissipative nature of the method. On the other hand, the small scales are much more energetic in the Lagrangian case. This is, however, expected since the FENE-P equations do not have any diffusive terms. A refinement of the mesh does not alter significantly the energy content of the small scales in the Lagrangian case but increases it in the Eulerian case, while decreasing it for large scales.

Fig. 6.3 also illustrates the spectrum of a Lagrangian simulation with creation and destruction of particles. It is observed in this case that small scales are slightly less energetic than the case without creation/destruction. This is explained by the diffusive nature of the creation and destruction process. However, it cannot explain the larger energy content of the large scales and, in particular, the higher mean extension. This is possibly due to an overprediction of the polymer stress during particle creation as a result of the nonlinearity of the relation between the conformation and stress tensors. In particular, when a new particle is created in a cell, it is assigned the average stress of all other particles in the cell. Since the function, which computes the stress from the conformation tensor, is nonlinear, monotonic and convex, the stress average of two particles is always larger than the stress corresponding to their average conformation tensor. Therefore, conserving the cell mean stress during the particle creation process always leads to a larger extension than conserving the cell mean conformation tensor. Fig. 6.2(b) shows the results of a simulation, $M'(18, 8, 28)$, where particles where created by conserving the conformation tensor and not the polymer stress. Although the mean extension is smaller than the $M(18, 8, 28)$ case, it is still much higher than for the case without creation/destruction of particles. This demonstrates that the nonlinearity of the stress function does not explain completely the overprediction of mean extension when particles are created.

Because creation and destruction of particles is an important part of the Lagrangian method, it is interesting to analyze it in more detail. Fig. 6.4(a) shows the global distribution of the number of particles in the channel. When particles are created and destroyed, the distribution is very symmetric and bounded between $N_{\min}$ and $N_{\max}$. In the case $M(20, 0, \infty)$ the distribution is much broader, with some cells having no particles. This justifies the need for particle creation. The average number of particles created per plane at each time step is illustrated in Fig. 6.4(b). Most of the particles are created at $y^+ \approx 11$,

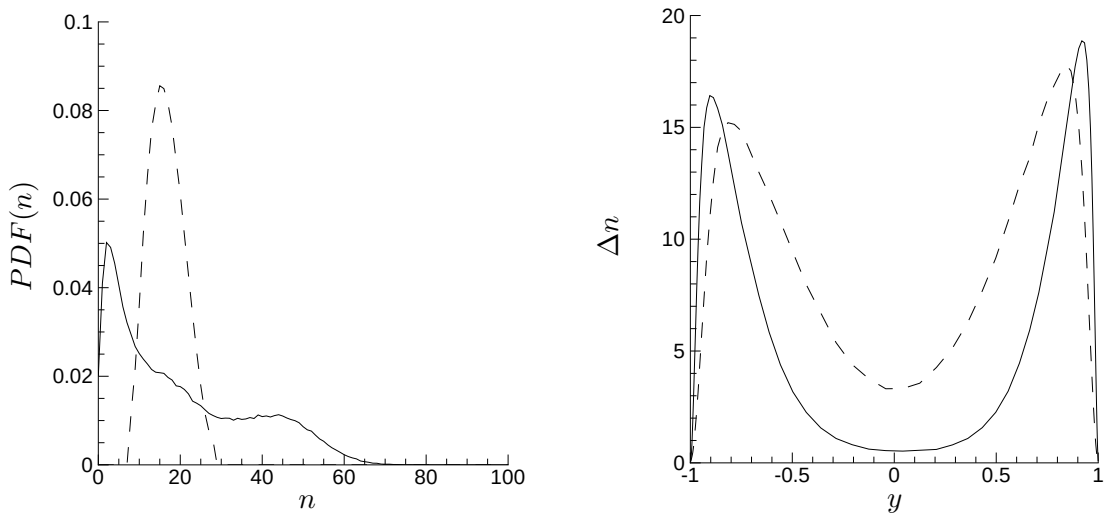

(a) (b)

Figure 6.4: (a) Global distribution function of the number of particles per cell; $M(20, 0, \infty)$: ——; $M(18, 8, 28)$: $\cdots\cdot$. (b) Plane and time average of the number of particles created (——) and destroyed ($\cdots\cdot$) at each time step for $M(18, 8, 28)$.

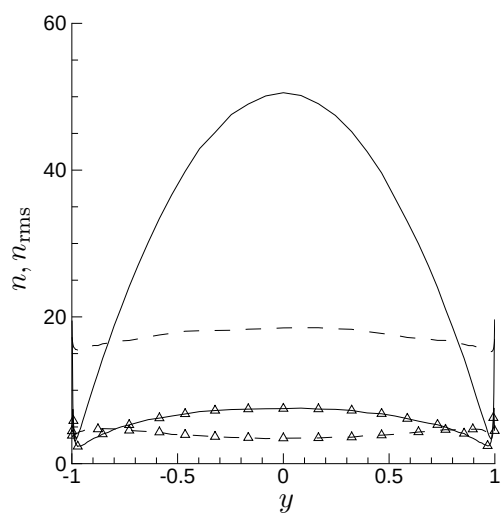

Figure 6.5: Plane average and rms (symbol) of the number of particles per cell along the wall-normal direction; $M(20, 0, \infty)$: ——; $M(18, 8, 28)$: $\cdots\cdot$.

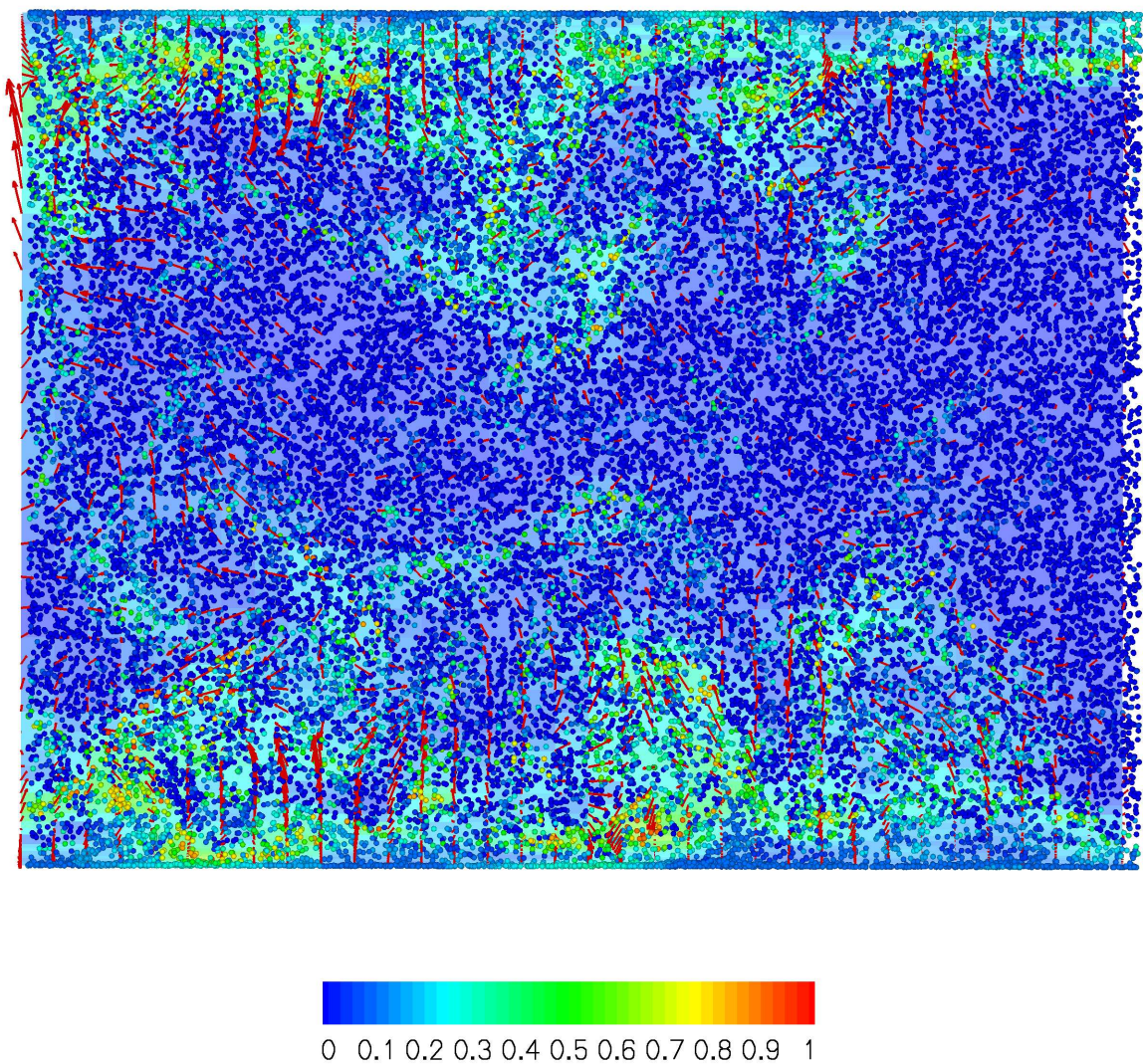

Figure 6.6: Polymer extension and velocity field in a plane perpendicular to the streamwise direction for the case $M(20, 0, \infty)$. The particles are colored according to their extension. The colored background corresponds to the cell average of the extension.

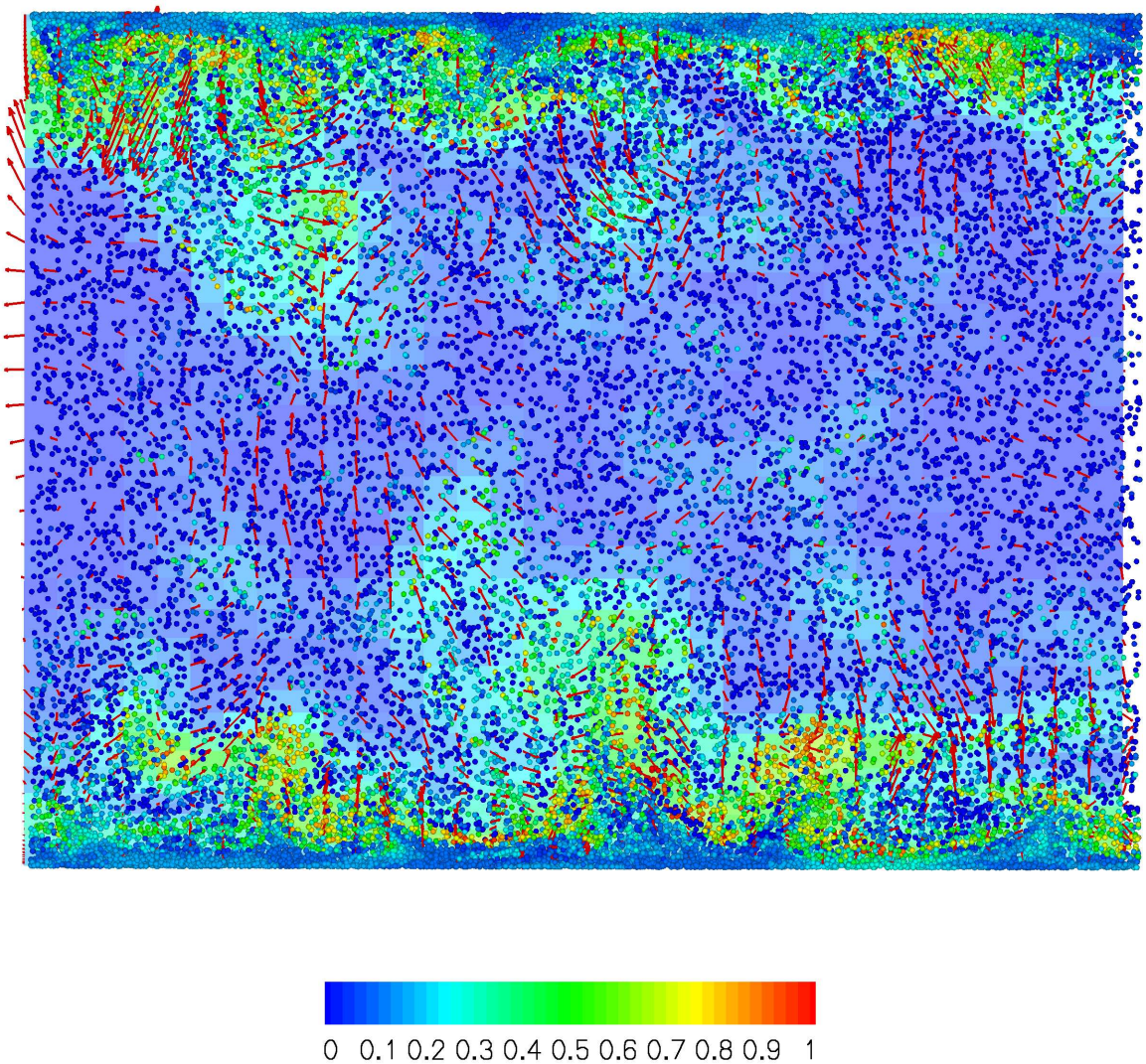

Figure 6.7: Polymer extension and velocity field in a plane perpendicular to the streamwise direction for the case $M(18, 8, 28)$. The particles are colored according to their extension. The colored background corresponds to the cell average of the extension.

where the mean extension reaches its peak, while particle destruction happens mostly at $y^+ \approx 20$, where the turbulence intensity is the highest. This could provide another explanation for the discrepancy between the different Lagrangian methods. Because particles are created in regions where their extension is high, it induces a positive flux of highly extended particles away from these regions, increasing the average extension. The plane average and rms number of particles per cell is shown in Fig. 6.5. While the case $M(18, 8, 28)$ has a very uniform distribution along the wall-normal direction, the case without creation/destruction shows accumulation of particles in the center of the channel, where the cells are much bigger, and depletion close to the wall, where the cells are much smaller. It is interesting to note that, at the wall, there is still a relatively large number of particles. This is due to very small velocities near the wall.

Fig. 6.6 and 6.7 show the particles colored by their extension in a plane perpendicular to the stremwise direction for the cases $M(20, 8, \infty)$ and $M(18, 8, 28)$. The background color corresponds to the cell mean extension. Also shown is the $y-z$ velocity field. While the case with creation/destruction shows a very homogeneous distribution of the particles, a large spatial accumulation of particle is observed close to the wall in the second case. Although the number of particles per cell is approximately uniform, the cells are much smaller close to the wall, which leads to this inhomogeneous volume distribution of particles. These two figures also illustrate clearly the small scales present in the solution of the FENE-P equations. Particles with different histories and different extensions can be found next to each other.

Based on these results, one can conclude that the more physical solution of the FENE-P equations is given by the Lagrangian method without creation or destruction of particles. However, this method is not suited for coupled calculations unless a prohibitively large number of particles is used to ensure a reasonable number of particles in every grid cell. Therefore, one has to compromise between accuracy and computational costs. The $M'(18, 8, 28)$ case seems to be a good trade-off between both requirements and surpasses by far the Eulerian method in terms of accuracy.

6.2 Coupled simulation

As mentioned in the previous section, the polymer stress, and thus the amount of drag reduction achieved, is directly dependent on the polymer extension. Therefore, it is important

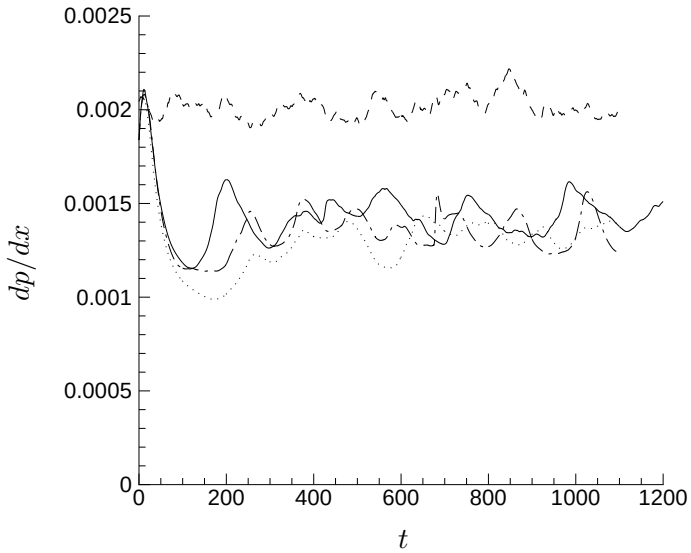

Figure 6.8: Mean pressure gradient as a function of time for a Newtonian flow at $Re = 2760$ (– – –), a viscoelastic flow at $DR = 29\%$ computed with the Lagrangian method $M(28, 8, 48)$ (——), a viscoelastic flow at $DR = 33\%$ computed with the Lagrangian method $M(18, 15, 21)$ (– · –) and a viscoelastic flow at $DR = 35\%$ computed with the Eulerian method (· · · ·).

to quantify the difference in drag reduction with the different methods. To achieve this goal, similar simulations as in the previous section have been performed with the concentration parameter $\beta = 0.9$, thus allowing the polymers to modify the turbulent flow.

Figure 6.8 represents the mean pressure gradient, driving the flow in the channel, as a function of time for the different cases tested. One can notice that the three different methods considered here, i.e., Eulerian, $M(18, 15, 21)$ and $M(28, 8, 48)$, produce drag reduction. The mean pressure gradient, wall shear stress and amount of drag reduction are summarized for each case in table 5.3, where the amount of drag reduction is defined as

$$DR = \frac{\mathrm{d}p/\mathrm{d}x_{\mathrm{newtonian}} - \mathrm{d}p/\mathrm{d}x_{\mathrm{viscoelastic}}}{\mathrm{d}p/\mathrm{d}x_{\mathrm{newtonian}}} \tag{6.1}$$

An initial increase in drag followed by a large drag reduction is observed, until the pressure gradient reaches a statistical steady value which is slightly higher than the minimum value reached during the transient phase. This is consistent with previous simulations of polymer drag reduction. As expected, the Eulerian method produces a larger amount of drag

Table 6.1: Coupled calculation with $\beta = 0.9$, $Wi = 7$ and $b = 10000$.

Method	$\mathrm{d}p/\mathrm{d}x$	τ_{wall}	δ^+	$\%DR$
Newtonian	$2.0150 \cdot 10^{-3}$	$2.032 \cdot 10^{-3}$	124.4	-
Eulerian	$1.3048 \cdot 10^{-3}$	$1.326 \cdot 10^{-3}$	100.5	35.2
$M(18, 15, 21)$	$1.3622 \cdot 10^{-3}$	$1.383 \cdot 10^{-3}$	102.6	32.4
$M(28, 8, 48)$	$1.4362 \cdot 10^{-3}$	$1.462 \cdot 10^{-3}$	105.5	28.7

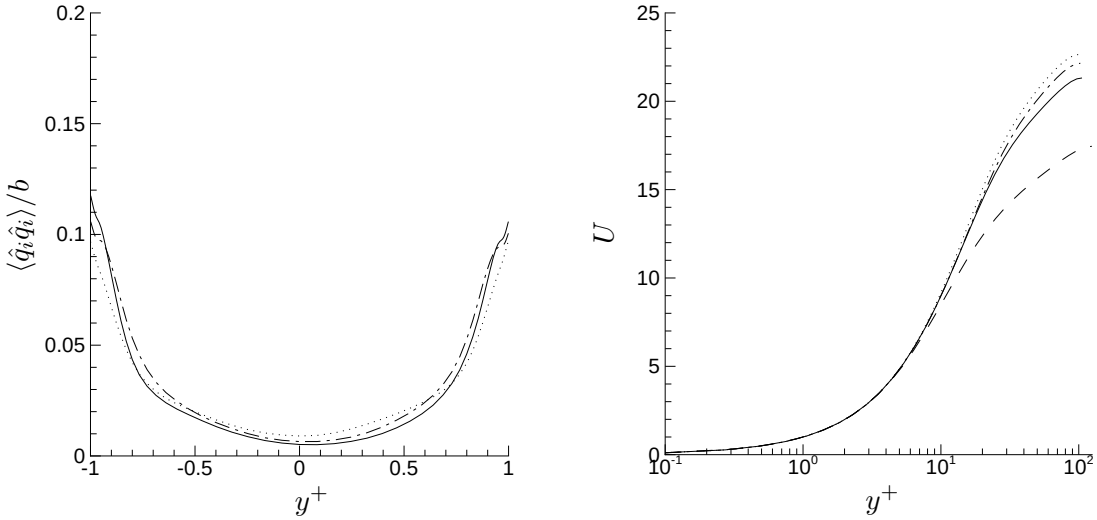

(a) (b)

Figure 6.9: Dimensionless polymer square extension (a) and mean velocity profile (b). Same labeling as in Fig. 6.8.

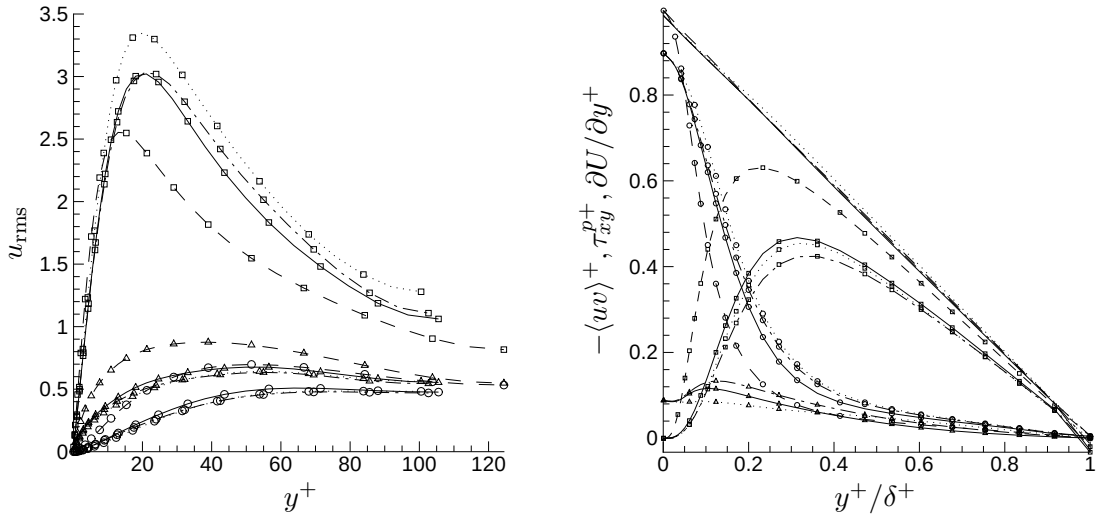

(a) (b)

Figure 6.10: (a): Velocity fluctuations; streamwise: □, spanwise: △, wall-normal: ○. (b): Stress balance; Reylnolds shear stress (□), viscous stress (○), polymer shear stress (△) and total stress (no symbol). Same labeling as in Fig. 6.8.

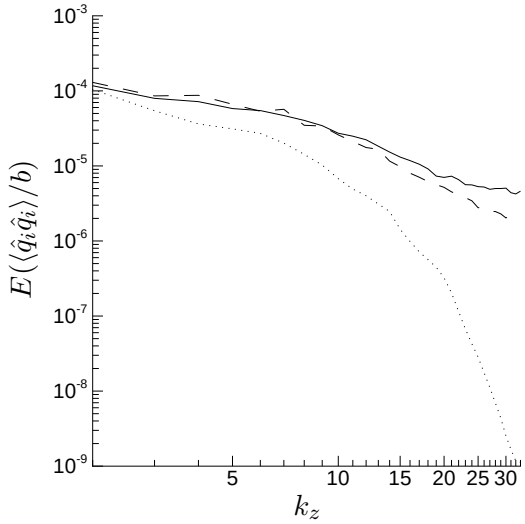

Figure 6.11: Spectrum of the dimensionless extension along the spanwise direction at $y^+ = 11$ in a drag reduced flow. Lagrangian $M(28, 8, 48)$: ——; Lagrangian $M(18, 8, 28)$: – – –; Eulerian ($LAD = 0.01$): · · · ·.

reduction, due to the higher polymer extension computed with it, while the Lagrangian method with the least number of particles created or destroyed shows the least amount of drag reduction. A better agreement in the drag reduced case is observed as compared to the uncoupled casees. The turbulence in the viscoelastic flow is much weaker, thus decreasing the strength of the nonlinear advection and the creation of very small scales, leading to better agreement in the polymer extension, as illustrated in Fig. 6.9(a). The discrepancy observed at the wall is simply due to the difference in wall shear rates between the different viscoelastic flows.

The mean velocity profiles in Fig. 6.9(b) show the well-known shift of the log-law, while the velocity fluctuations in Fig. 6.10(a) reproduce well the increase in streamwise direction and decrease in spanwise and wall-normal directions compared to the Newtonian flow. There is very good agreement amont the drag-reduced flows for the spanwise and wall-normal velocity fluctuations, while the Eulerian approach seems to overpredict the increase of the velocity fluctuations in the streamwise direction. Fig. 6.10(b) shows the decrease in the Reynolds stress which is observed in any polymer drag reduced flow. The additional polymer shear stress produced in viscoelastic flows and the viscous stress are also shown in the same figure. Finally, the spectrum of the dimensionless extension along the spanwise direction at $y^+ = 11$ is shown in Fig. 6.11. The same behaviour is found as in the uncoupled case, where the Eulerian method shows a much lower energy at small scales.

6.3 Discussion

The comparison between the Eulerian and Lagrangian methods without creation or destruction of particles has shown an important discrepancy in the uncoupled case. Although a rigorous explanation is not available, we have attributed it to the nonlinearity of the advection term and the resulting production of small scales in the Eulerian formulation. The dissipative schemes and artificial diffusion used in Eulerian simulations for numerical stability dissipate the small scales but not the larger ones, leading to an overprediction of the mean polymer stress. The Lagrangian method allows a more accurate prediction, since the nonlinear advective term does not appear in its formulation. However, creation and destruction of particles is needed in coupled simulations to ensure a reasonable number of particles in each grid cell. This process introduces numerical errors. The energy of the small scales is reduced by the diffusive nature of the process and the creation of particles

increase the polymer stress. Two possible reasons for this are the nonlinearity of the stress function and a non-zero flux of highly extended particles from the near-wall region. An easy remedy for this problem is to limit the number of particles created and destroyed. This can be achieved by choosing loose bounds on the imposed number of particles within a cell. Another approach could be to conserve the polymer conformation tensor and not stress during the creation process. This lead to a small improvement but did not compensate completely the discrepancy.

Despite these shortcomings, the Lagrangian approach has demonstrated the ability to reproduce the characteristic features of drag reduction. Comparison of the different methods shows good qualitative agreement in drag reduced flows, but it is difficult to assess the accuracy of the Lagrangian or Eulerian approaches, since no comparable work exists and a direct comparison to experimental data is extremely difficult, i.e., the Schmidt and Reynolds numbers are too high for computations, the Weissenberg number of the solution is complicated to characterize due to polydispersity, the polymer stress cannot be measured experimentally.

Chapter 7

Conclusion

The phenomenon of turbulent drag reduction by polymer additives has been investigated using a Lagrangian approach. The goal of this work was to better understand the dynamics of single polymer molecules in a turbulent flow and to develop a numerical method to simulate the effect of polymer additives on turbulence. The latter goal was motivated by the fact that the accuracy of traditional Eulerian simulations of viscoelastic flows is limited by their need for numerical artifices to stabilize the computation. This chapter summarizes the issues encountered and the results found using the Lagrangian framework to compute the polymer stresses. Finally, possible extensions of the present work and new directions for future research are suggested.

7.1 Uncoupled simulations

Uncoupled simulations, i.e., where the flow remains Newtonian, aimed at better understanding the dynamics of polymer molecules in turbulent flows, were performed. First, different models, based on both Brownian dynamics techniques and constitutive models, were compared. It was found that the qualitative behavior of all models was very similar, although the FENE-P model tended to slightly overestimate the polymer extension. An important finding from these simulations was that the internal modes of the polymer chains do not seem to be relevant to the overall mechanisms of the phenomenon.

A topological methodology was then introduced after recognizing the similarities of the FENE equation with the equation governing the flow trajectory at a singular point. This topological methodology leads to a classification of different flow types. Combining

it with conditional statistics, it was possible to isolate the particular flow types relevant to the stretching and relaxation dynamics of the polymer molecules. In particular, it was found that the most probable flow type which can stretch the polymer to a large extension corresponds to biaxial extensional flow. Strong biaxial extensional flows are mainly located in the buffer layer, in the vicinity of the quasi-streamwise vortices. Moreover, polymers with large extensions were correlated with positive wall-normal velocity, i.e., updrafts. This indicates that the pre-stretching of the polymers by the mean shear close to the wall plays an important role. It was also observed that the polymer molecules relax in rotational regions of the flow in or around the vortices. This is in very good agreement with previous works, confirming and extending the proposed mechanisms that the polymers become stretched in the buffer layer and then relax around the vortices and, as a result, damping them.

Similar simulations in viscoelastic flows showed that this mechanism is also valid in drag-reduced flows. The main difference was found to be the strength of the biaxial extensional flows, which is to be expected since the turbulence is much weaker in drag-reduced flows. However, it is important to remember that the artificial dissipation introduced in the Eulerian method has a non-negligible impact on the simulation of viscoelastic flows, as was shown in section 6.1. Because of the discrepancy between Lagrangian and Eulerian calculations, the validity of this result may be questioned. Nonetheless, this discrepancy decreases in flows with large drag reduction. Therefore, one can assume that, to a certain degree, the stretching and relaxation dynamics of polymer molecules are similar in both Newtonian and viscoelastic flows.

7.2 Coupled simulations

Due to the hyperbolic nature of the polymer equations, it was necessary to introduce artificial diffusion to stabilize Eulerian simulations. To overcome this difficulty, a Lagrangian method was developed to compute drag reduced flows. As in the uncoupled case, a large number of particles were tracked in the turbulent flow and the polymer stresses were computed along the particle trajectories. Because the velocity field was computed in an Eulerian framework and the polymer stresses were only known at the particle locations, a new technique to transfer the polymer stresses to the Eulerian grid had to be developed. The simplest approach was to compute a cell average of the polymer stresses over all particles within a cell. Because the polymer solution was assumed to be homogeneous, this required

a minimum number of particles in each grid cell. Due to the non-uniformity of the mesh, which would have required a prohibitively large number of particles, the number of particles in each cell had to be constrained between two bounds. This required the creation and destruction of particles throughout the simulation. The destruction of particles was simply achieved by replacing the two closest particles in a cell by a new one located at the mid-distance between them and by giving it the mean polymer stress of the two deleted particles. If not enough particles were present in a given cell, a new particle was created at a random location within the quadrant of the cell containing the least number of particles. Two different methods were developed to assign the initial polymer stresses to the newly created particle. The first method simply assigned it the cell average stress, while the second interpolated the mean stress from the neighbor cells at the particle locations.

The Lagrangian approach was tested for the advection problem of a passive scalar in a Taylor–Green vortex. It was shown that this method outperformed the Eulerian approach, despite its computational cost. Although no explicit artificial dissipation was used, it was observed that the creation and destruction of particles induced diffusion. However, by choosing the method where new particles are given the cell average stress values for the creation of particles and a large enough interval between the minimum and maximum number of particles, it was possible to minimize this problem.

The method was then validated in a turbulent flow with zero polymer concentration (uncoupled simulation). An important discrepancy in the extension of polymers was observed between the Eulerian and Lagrangian simulations. It was demonstrated that the dissipative nature of the Eulerian scheme led to an underprediction of the energy at small scales, but showed a higher energy in the large scales, thus overpredicting the mean polymer stress. The creation and destruction of particles in the Lagrangian method also dissipated energy at small scales, while it increased the polymer stress at larger scales. This increase of polymer stress could be due to the nonlinearity of the stress. It was shown that this could be partly compensated by conserving the mean polymer conformation tensor rather than stress when creating particles. A mesh refinement showed a slow convergence of the two methods towards a polymer extension lying between the Eulerian and Lagrangian solutions.

Finally, both approaches were tested for drag-reduced flows. All the characteristic features of polymer drag reduction could be reproduced by the Lagrangian method. Despite the large discrepancy observed in uncoupled simulations, similar amounts of drag reduction were observed with both methods. This could be explained by the much weaker turbulence

in viscoelastic flows, which renders the flow much smoother, and thus decreases the impact of the nonlinear advection term.

7.3 Future work

A better understanding of polymer drag reduction has been gained from the Lagrangian approach. Despite its shortcomings, it has led to important improvements for simulating drag-reduced flows compared to the traditional Eulerian method. Nonetheless, other improvements could be made. One important improvement would be in the development of a less dissipative method for the creation and destruction of particles. A possible new approach could use the particles within a cell to determine a probability distribution function: a random stress value would be assigned to the newly created particle based on this distribution function. In order to limit the number of particles needed to determine the distribution function, one could also assume a standard distribution and scale it according to the mean and standard deviation computed from the particles in the cell. The shape of such a distribution function would have to satisfy certain constraints, since the extension of the polymer is bounded between a minimum and maximum value.

Another extension to this work would be the implementation of the coupled Lagrangian method for other polymer models, e.g., FENE and bead-spring chain model. Because these models are based on Brownian dynamics techniques, many realizations would be needed for each particle, requiring significant computational effort. In light of the present work, however, it is not evident that a better understanding of the phenomenon would be achieved.

The final suggested application of this work would be to describe the evolution of the polymer concentration in the flow, since in most applications the polymer solution is not homogeneous but injected. Such a computation is again very challenging because of the low diffusivity of the polymers. Therefore, the Lagrangian method seems to be the best approach for this problem.

Appendix A

Spatial interpolation

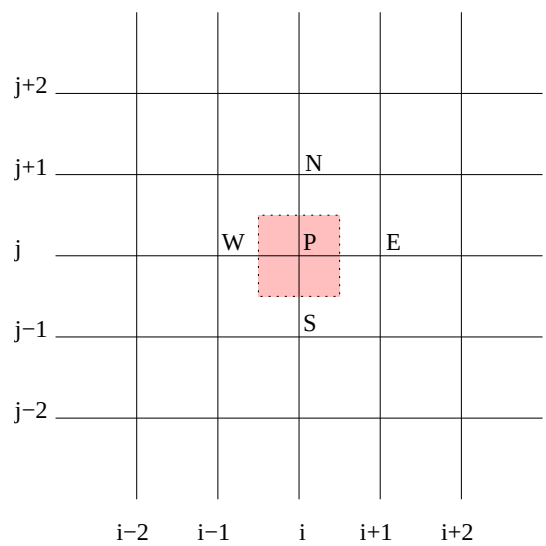

Figure A.1: Grid

The following definitions will be used throughout this appendix:

$$
\begin{aligned}
\Delta x_i &= x_{i+1} - x_i, \\
\Delta y_j &= y_{j+1} - y_j, \\
\Delta z_k &= z_{k+1} - z_k, \\
\xi &= x - x_i, \\
\eta &= y - y_j, \\
\zeta &= z - z_k, \\
f_{i,j,k} &= f(x_i, y_j, z_k), \\
f_{,\alpha} &= \frac{\partial f}{\partial \alpha}.
\end{aligned}
$$

A.1 Trilinear interpolation

The value of the function f at any point $\boldsymbol{x} = (x, y, z)$ in the cell defined by $(x_i : x_{i+1}, y_j : y_{j+1}, z_k : z_{k+1})$ can be evaluated with the following formula

$$
\begin{aligned}
f(x,y,z) = &\left(1 - \frac{\xi}{\Delta x_i}\right)\left(1 - \frac{\eta}{\Delta y_j}\right)\left(1 - \frac{\zeta}{\Delta z_k}\right) f_{i,j,k} \\
&+ \left(1 - \frac{\xi}{\Delta x_i}\right)\left(1 - \frac{\eta}{\Delta y_j}\right)\frac{\zeta}{\Delta z_k} f_{i,j,k+1} \\
&+ \left(1 - \frac{\xi}{\Delta x_i}\right)\frac{\eta}{\Delta y_j}\left(1 - \frac{\zeta}{\Delta z_k}\right) f_{i,j+1,k} \\
&+ \frac{\xi}{\Delta x_i}\left(1 - \frac{\eta}{\Delta y_j}\right)\left(1 - \frac{\zeta}{\Delta z_k}\right) f_{i+1,j,k} \\
&+ \left(1 - \frac{\xi}{\Delta x_i}\right)\frac{\eta}{\Delta y_j}\frac{\zeta}{\Delta z_k} f_{i,j+1,k+1} \\
&+ \frac{\xi}{\Delta x_i}\left(1 - \frac{\eta}{\Delta y_j}\right)\frac{\zeta}{\Delta z_k} f_{i+1,j,k+1} \\
&+ \frac{\xi}{\Delta x_i}\frac{\eta}{\Delta y_j}\left(1 - \frac{\zeta}{\Delta z_k}\right) f_{i+1,j+1,k} \\
&+ \frac{\xi}{\Delta x_i}\frac{\eta}{\Delta y_j}\frac{\zeta}{\Delta z_k} f_{i+1,j+1,k},
\end{aligned}
\tag{A.1}
$$

where f can be either a velocity or a velocity gradient's component.

A.2 Tricubic spline

A summary of the cubic spline coefficients for a three-dimensional domain can be found in Ucinski (1999). It requires the solution of tridiagonal systems.

References

Achia, B. U. and Thompson, D. W. 1977 Structure of the turbulent boundary in drag-reducing flow. *J. Fluid Mech.* **81**, 439–464.

Ahlrichs, P. and Duenweg, B. 1998 Lattice boltzmann simulation of polymer-solvent systems. *Int. J. Mod. Phys. C* **9**, 1429–1438.

Angelis, E. D., Casciola, C. M., Lvov, V. S., Piva, R. and Procaccia, I. 2003 Drag reduction by polymers in turbulent channel flows: Energy redistribution between invariant empirical modes. *Phys. Rev. E* **67**, 056312.

Angelis, E. D., Casciola, C. M., Lvov, V. S., Pomyalov, A., Procaccia, I. and Tiberkevich, V. 2004 Drag reduction by a linear viscosity profile. *Phys. Rev. E* **70**, 055301.

Babcock, H. P., Smith, D. E., Hur, J. S., Shaqfeh, E. S. G. and Chu, S. 2000 Relating the microscopic and macroscopic response of a polymeric fluid in a shear flow. *Phys. Rev. Letts* **85(9)**, 2018–2021.

Baron, A. and Sibilla, S. 1997 DNS of the turbulent channel flow of a dilute polymer solution. *Flow, Turbulence and Combustion* **59(4)**, 331–352.

Batchelor, G. K. 1959 Small-scale variation of convected quantities like temperature in turbulent fluid. *J. Fluid Mech.* **5**, 113–139.

Benzi, R., Angelis, E. D., Govindarajan, R. and Procaccia, I. 2003 Shell model for drag reduction with polymer additives in homogeneous turbulence. *Phys. Rev. E* **68**, 016308.

Benzi, R. and Procaccia, I. 2003 Simple model for drag reduction. *Phys. Rev. E* **68**, 025303.

Beris, A. and Dimitropoulos, C. 1999 Pseudospectral simulation of turbulent viscoelastic channel flow. *Comput. Methods Appl. Engrg.* **180**, 365.

Beris, A. and Sureshkumar, R. 1996 Simulation of time-dependent viscoelastic channel poiseuille flow at high Reynolds numbers. *Chemical Engineering Science* **51(9)**, 1451.

Berman, N. S. 1986 Velocity fluctuations in non-homogeneous drag reduction. *Chem. Engg. Commun.* **42**, 37.

Bhattacharjee, J. K. and Thirumalai, D. 1991 Drag reduction in turbulent flows by polymers. *Physical Review Letters* **76**, 196.

Bird, R., Curtiss, C., Armstrong, R. and Hassager, O. 1987 *Dynamics of Polymer Liquids. Vol.2. Kinetic Theory*, 2nd edn. Wiley, New York.

Bird, R. B. and Wiest, J. M. 1995 *Annu. Rev. Fluid Mech.* **27**, 169–193.

Blackburn, H., Mansour, N. and Cantwell, B. 1996 Topology of fine-scale motions in turbulent channel flow. *J. Fluid Mech.* **310**, 269–292.

Chertkov, M. 2000 Polymer stretching by turbulence. *Phys. Rev. Lett.* **84**, 4761–4764.

Choi, H., Moin, P. and Kim, J. 1993 Direct numerical simulation of turbulent flow over riblets. *J. Fluid Mech.* **255**, 503–539.

Choi, H., Moin, P. and Kim, J. 1994 Active turbulence control for drag reduction in wall-bounded flows. *J. Fluid Mech.* **262**, 75–110.

Choi, K.-S. and Graham, M. 1998 Drag reduction of turbulent pipe flows by circular-wall oscillation. *Phys. Fluids* **10(8)**, 1997–2005.

Chong, M., Perry, A. and Cantwell, B. 1990 A general classification of three-dimensional flow fields. *Phys. Fluids A* **2(5)**, 765–777.

Cruz, D. O. A. and Pinho, F. T. 2003 Turbulent pipe flow predictions with a low Reynolds number $k-\epsilon$ model for drag reducing fluids. *J. Non-Newton. Fluid Mech.* **114**, 109–148.

Cruz, D. O. A., Pinho, F. T. and Resende, P. R. 2004 Modelling the new stress for improved drag reduction predictions of viscoelastic pipe flow. *J. Non-Newton. Fluid Mech.* **121**, 127–141.

Devanand, K. and Selser, J. C. 1991 Asymptotic behavior and long-range interactions in aqueous solutions of polyethylene oxide. *Macromolecules* **24**, 5943–5947.

Dimitrakopoulos, P. 2004 Stress and configuration relaxation of an initially straight flexible polymer. *J. Fluid Mech.* **513**, 265–286.

Dimitropoulos, C., Sureshkumar, R. and Beris, A. 1998 Direct numerical simulation of viscoelastic turbulent channel flow exhibiting drag reduction: effect of the variation of rheological parameters. *J. Non-Newtonian Fluid Mech.* **79**, 433.

Dimitropoulos, C., Sureshkumar, R., Beris, A. and Handler, R. 2001 Budgets of Reynolds stress, kinetic energy and streamwise enstrophy in viscoelastic turbulent channel flow. *Phys. Fluids* **13(4)**, 1016.

Dimitropoulos, C. D., Dubief, Y., Shaqfeh, E. S. G., Moin, P. and Lele, S. K. 2005 Direct numerical simulation of polymer-induced drag reduction in turbulent boundary layer flow. *Phys. Fluids* **17**, 011705.

Dominicis, C. D. and Martin, H. 1979 *Phys. Rev.* **A19**, 219.

Doyle, P. S. and Shaqfeh, E. S. G. 1998 Dynamics simulations of freely-draining flexible bead-rod chains: start-up of extensional flow. *J. Non-Newton. Fluid Mech.* **76**, 43–78.

Doyle, P. S., Shaqfeh, E. S. G. and Gast, A. P. 1997 Dynamic simulation of freely draining flexible polymers in steady linear flow. *J. Fluid Mech.* **334**, 251–291.

Doyle, P. S., Shaqfeh, E. S. G., McKinley, G. H. and Spiegelberg, S. H. 1998 Relaxation of dilute polymer solutions following extensional flow. *J. Non-Newton. Fluid Mech.* **76**, 79–110.

Dubief, Y. 2002 *Numerical simulation of turbulent polymer solutions.*, pp. 377–388. Annual Research Briefs, Center for Turbulence Research.

Dubief, Y. 2003 *Numerical simulation of high drag reduction in a turbulent channel flow with polymer additives.*, pp. 439–448. Annual Research Briefs, Center for Turbulence Research.

Dubief, Y. and Delcayre, F. 2000 On coherent-vortex identification in turbulence. *J. Turbul.* **1(011)**, 1–22.

Dubief, Y., Iaccarino, G. and Lele, S. K. 2004*a* *A turbulence model for polymer flows.*, pp. 63–73. Annual Research Briefs, Center for Turbulence Research.

Dubief, Y. and Lele, S. 2001 *Direct numerical simulation of polymer flow.*, pp. 197–208. Annual Research Briefs, Center for Turbulence Research.

Dubief, Y., Terrapon, V. E., White, C. M., Shaqfeh, E. S. G., Moin, P. and Lele, S. K. 2005 New answers on the interaction between polymers and vortices in turbulent flows. *to appear in Flow, Turbulence and Combustion* .

Dubief, Y., White, C. M., Terrapon, V. E., Shaqfeh, E. S. G., Moin, P. and Lele, S. K. 2004*b* On the coherent drag-reducing and turbulence-enhancing behaviour of polymers in wall flows. *J. Fluid Mech.* **514**, 271–280.

Durbin, P. A. 1995 Separated flow computations with the $k - \epsilon - v^2$ model. *AIAA J.* **33**, 659–664.

Eckhardt, B., Kronjaeger, J. and Schumacher, J. 2002 Stretching of polymers in a turbulent environment. *Comp. Phys. Comm.* **147**, 538–543.

Evans, A. R. and Shaqfeh, E. S. G. 1996 The conformation of semi-rigid polymers during flow through a fixed fiber bed. *J. Non-Newton. Fluid Mech.* **64**, 95–140.

Fontaine, A. A., Petrie, H. L. and Brungart, T. A. 1972 Velocity profile statistics in a turbulent boundary layer with slot-injected polymer. *J. Fluid Mech.* **56**, 559–575.

Fouxon, A. and Lebedev, V. 2003 Spectra of turbulence in dilute polymer solutions. *Phys. Fluids* **15(7)**, 2060–2072.

Fraenkel, G. K. 1952 *J. Chem. Phys.* **20**, 642–647.

Fukagata, K., Iwamoto, K. and Kasagi, N. 2002 Contribution of Reynolds stress distribution to the skin friction in wall-bounded flows. *Phys. Fluids* **14**, 73–76.

Gallez, X., Halin, P., Lielens, G., Keunings, R. and Legat, V. 1999 The adaptive Lagrangian particle method for macroscopic and micro-macro computations of time-dependent viscoelastic flows. *Comput. Methods Appl. Mech. Engrg.* **180**, 345–364.

de Gennes, P.-G. 1974 Coil-stretch transition of dilute flexible polymers under ultrahigh velocity gradients. *J. Chem. Phys.* **60(12)**, 5030–5042.

de Gennes, P.-G. 1990 Introduction to polymer dynamics. *Cambridge University Press* .

de Gennes, P.-G. 1997 Molecular individualism. *Science* **276**, 1999–2000.

Ghosh, I., Joo, Y. L., McKinley, G. H., Brown, R. A. and Armstrong, R. C. 2002 A new model for dilute polymer solutions in flows with strong extensional components. *J. Rheol.* **46(5)**, 1057–1089.

Ghosh, I., McKinley, G. H., Brown, R. A. and Armstrong, R. C. 1998 Deficiencies of fene dumbbell models in describing the rapid stretching of dilute polymer solutions. *J. Non-Newton. Fluid Mech.* **76**, 249–279.

Ghosh, I., McKinley, G. H., Brown, R. A. and Armstrong, R. C. 2001 Deficiencies of fene dumbbell models in describing the rapid stretching of dilute polymer solutions. *J. Rheol.* **45(3)**, 721–758.

Gyr, A. and Bewersdorff, H.-W. 1995 *Drag reduction of turbulent flows by additives*. Kluwer Academic.

Halin, P., Lielens, G., Keunings, R. and Legat, V. 1998 The Lagrangian particle method for macroscopic and micro-macro viscoelastic flow computations. *J. Non-Newtonian Fluid Mech.* **79**, 387–403.

Harder, K. J. and Tiederman, W. G. 1991 Drag reduction and turbulent structure in two-dimensional channel flows. *Phil. Trans. R. Soc. Lond. A* **336**, 19–34.

Hassager, O. and Bird, R. B. 1972 *J. Chem. Phys.* **56**, 2498–2501.

Hermans, J. J. 1943 *Physica* **10**, 777–789.

Herrchen, M. and Oettinger, H. 1997 A detailed comparison of various fene dumbbell models. *J. Non-Newtonian Fluid Mech.* **68**, 17.

Hulsen, M. A., van Heel, A. P. G. and van den Brule, B. H. A. A. 1997 Simulation of viscoelastic flows using brownian configuration fields. *J. Non-Newtonian Fluid Mech.* **70**, 79–101.

Hur, J., Shaqfeh, E., Babcock, H. and Chu, S. 2001*a* The dynamics of dilute and semi-dilute dna solutions in the start-up of shear flow. *J. Rheol.* **45(2)**, 421–450.

Hur, J., Shaqfeh, E., Babcock, H. and Chu, S. 2002 Dynamics and configurational fluctuations of single dna molecules in linear mixed flows. *Phys. Rev. E,* **66**, 011915.

Hur, J. S., Shaqfeh, E. S. G., Babcock, H. P., Smith, D. E. and Chu, S. 2001*b* Dynamics of dilute and semidilute dna solutions in the start-up of shear flow. *J. Rheol.* **45(2)**, 421.

Hur, J. S., Shaqfeh, E. S. G. and Larson, R. G. 2000 Brownian dynamics simulations of single dna molecules in shear flow. *J. Rheol.* **44(4)**, 713–742.

Ilg, P., de Angelis, E., Karlin, I. V., Casciola, C. M. and Succi, S. 2002 Polymer dynamics in wall turbulent flow. *Europhys. Lett.* **58(4)**, 616–622.

Ispolatov, I. and Grant, M. 2002 Lattice boltzmann method for viscoelastic fluids. *Phys. Rev. E* **65**, 056704.

Jimenez, J. and Moin, P. 1991, The minimal flow unit in near-wall turbulence. *J. Fluid Mech.* **225**, 213–240.

Jimenez, J. and Pinelli, A. 1999, The autonomous cycle of near-wall turbulence. *J. Fluid Mech.* **389**, 335–359.

Keunings, R. 1997 On the peterlin approximation for finitely extensible dumbbells. *J. Non-Newton. Fluid Mech.* **68**, 17–42.

Kim, J. and Moin, P. 1985 Application of a fractional-step method to incompressible navier–stokes equations. *J. Comp. Phys.* **59**, 308–323.

Kline, S. J., Reynolds, W. C., Schraub, F. A. and Runstadler, P. W. 1967 The structure of turbulent boundary layers. *J. Fluid Mech.* **30**, 741–773.

Kline, S. J. and Robinson, S. K. 1988 Quasi-coherent structures in the turbulent boundary layer: Part I. *Proceedings of the International Centre for Heat and Mass Transfer* pp. 200–217.

Kontomaris, K., Hanratty, T. and McLaughlin, J. 1992 An algorithm for tracking fluid particles in a spectral simulation of turbulent channel flow. *J. Comp. Phys.* **103**, 231–242.

Kramers, H. A. 1944 The viscosity of macromolecules in a streaming fluid. *Physica* **11**, 1–19.

Kwan, T. C. B., Woo, N. J. and Shaqfeh, E. S. G. 2001 An experimental and simulation study of dilute polymer solutions in exponential shear flow. *J. Rheol.* **45**, 321–349.

Larson, D. 1999 *The Structure and Rheology of Complex Fluids.*. Oxford University Press.

Larson, R. G., Hu, H., Smith, D. E. and Chu, S. 1999 Brownian dynamics simulations of a dna molecule in an extensional flow field. *J. Rheol.* **43**, 267–304.

Larson, R. G., Perkins, T. T., Smith, D. E. and Chu, S. 1997 *Phys. Rev. E* **55**, 1794.

Laso, M. and Oettinger, H. C. 1993 *J. Non-Newtonian Fluid Mech.* **47**, 1–20.

Le, H. and Moin, P. 1991 An improvement of fractional step methods for the incompressible navier-stokes equations. *J. Comput. Phys.* **92**, 369–379.

Lee, W. K., Vaseleski, R. C. and Metzner, A. B. 1974 *AIChE* **20**, 128.

Leighton, R., Walker, D. T., Stephens, T. and Garwood, G. 2003 Reynolds stress modeling for drag reducing viscoelastic flows. ASME-JSME, Honolulu, Hawaii USA.

Li, L., Larson, R. G. and Sridhar, T. 2000 Brownian dynamics simulation of dilute polystyrene solutions. *J. Rheol.* **44**, 291–322.

Lielens, G., Halin, P., Taumain, I., Keunings, R. and Legat, V. 1998 New closure approximations for the kinetic theory of finitely extensible dumbbells. *J. Non-Newton. Fluid Mech.* **76**, 249–279.

Lim, J., Choi, H. and Kim, J. 1998 Control of streamwise vortices with uniform magnetic fluxes. *Phys. Fluids* **10(8)**, 1997–2005.

Luchik, T. S. and Tiederman, W. G. 1988 Turbulent structure in low-concentration drag-reducing channel flows. *J. Fluid Mech.* **1990**, 241–263.

Lumley, J. L. 1969 Drag reduction by additives. *Ann. Rev. Fluid Mech.1* p. 367.

Marko, J. F. and Siggia, E. D. 1991 Stretching DNA. *Macromolecules* **28**, 3427–3433.

Massah, H. and Hanratty, T. J. 1997 Added stresses because of the presence of FENE-P bead-spring chains in a random velocity field. *J. Fluid Mech.* **337**, 67–101.

Massah, H., Kontomaris, K., Schowalter, W. R. and Hanratty, T. J. 1993 The configurations of a fene bead-spring chain in transient rheological flows and in a turbulent flow. *Phys. Fluids A* **5(4)**, 881–890.

McComb, W. D. and Chan, K. T. J. 1985 Laser-Doppler anemometer measurements of turbulent structure in drag-reducing fibre suspensions. *J. Fluid Mech.* **152**, 455.

Min, T., Yoo, J. and Choi, H. 2001 Effect of spatial discretization schemes on numerical solutions of viscoelastic fluid flows. *J. Non-Newton. Fluid Mech.* **100**, 27.

Min, T., Yoo, J., Choi, H. and Joseph, D. D. 2003 Drag reduction by polymer additives in a turbulent channel flow. *J. Fluid Mech.* **486**, 213–238.

Morinishi, Y., Lund, T. S., Vasilyev, O. V. and Moin, P. 1998 Fully conservative higher order finite difference schemes for incompressible flow. *J. Comput. Phys.* **143**, 90–124.

Moyls, A. L. and Sabersky, R. H. 1978 Heat transfer and friction coeffficients for dilute suspensions of asbestos fibers. *Int. J. Heat Mass Transfer* **21**, 7.

Oettinger, H. C. 1996 *Stochastic Processses in Polymeric Fluids*. Springer, Berlin.

Oettinger, H. C., van den Brule, B. H. A. A. and Hulsen, M. A. 1997 Brownian configuration fields and variance reduced connffessit. *J. Non-Newtonian Fluid Mech.* **70**, 255–261.

Oettinger, H. C. and Laso, M. 1992 Smart polymers in finite element calculations. pp. 286–288. International Congress on Rheology, Amsterdam: Elsevier.

Oldaker, D. K. and Tiederman, W. G. 1977 Structure of the turbulent boundary layer in drag reducing pipe flow. *Phys. Fluids* **20**, 133–144.

Paschkewitz, J. S., Dimitropoulos, C. D., Somandepalli, V. S. R., Mungal, M. G., Shaqfeh, E. S. G. and Moin, P. 2005*a* An experimental and numerical investigation of drag reduction in a turbulent boundary layer using a rigid rod-like polymer. *to appear in Phys. Fluids* .

Paschkewitz, J. S., Dubief, Y., Dimitropoulos, C. D., Shaqfeh, E. S. G. and Moin, P. 2004 Numerical simulation of turbulent drag reduction using rigid fibres. *J. Fluid Mech.* **518**, 281–317.

Paschkewitz, J. S., Dubief, Y. and Shaqfeh, E. S. G. 2005*b* The dynamic mechanism for turbulent drag reduction using rigid fibers based on lagrangian conditional statistics. *to appear in Phys. Fluids* .

Perkins, T. T., Smith, D. E. and Chu, S. 1995 Single polymer dynamics in an elongational flow. *Science* **268**, 83–87.

Peterlin, A. 1961 Einfluš der endlichen Moleküllänge auf die Gradientenabhängigkeit des Staudinger-Index. *Makr. Chem.* **44**, 338–346.

Petrie, H. L., Deutsch, S., Brungart, T. A. and Fontaine, A. A. 2003 Polymer drag reduction with surface roughness in flat-plate turbulent boundary layer flow. *Exp. Fluids* **35**, 8–23.

Petrie, H. L. and Fontaine, A. A. 1996 Comparison of turbulent boundary layer modification with slot-injected and homogeneous drag-reducing polymer solutions. *ASME Fluids Eng. Div. Conf.* **237**, 205–210.

Pope, S. B. 2000 *Turbulent Flows*. Cambridge University Press.

Ptasinski, P. K., Boersma, B. J., Nieuwstadt, F. T. M., Hulsen, M. A., Brule, B. H. A. A. V. D. and Hunt, J. C. R. 2003 Turbulent channel flow maximum drag reduction: simulations, experiments and mechanisms. *J. Fluid Mech.* **490**, 251–291.

Ptasinski, P. K., Nieuwstadt, F. T. M., Brule, B. H. A. A. V. D. and Hulsen, M. A. 2001 Experiments in turbulent pipe flow with polymer additives at maximum drag reduction. *Flow, Turbulence and Combustion* **66**, 159–182.

Rabin, Y. and Zielinska, B. J. A. 1989 Scale-dependent enhancement and damping of vorticity disturbances by polymers in elongational flow. *Physical Review Letters* **63**, 512.

Robinson, S. K. 1991 Coherent motions in the turbulent boundary layer. *Ann. Rev. Fluid Mech.* **23**, 601–639.

Rouse, P. E. 1953 A theory of the linear viscoelastic properties of dilute solutions of coiling polymers. *J. Chem. Phys.* **21**, 1272–1280.

Ryskin, G. 1987 Turbulent drag reduction by polymers: A quantitative theory. *Physical Review Letters* **59**, 2059.

Shaqfeh, E. S. G., Patel, P., Mosler, A. B., Cristini, V., Blawzdziewicz, J. and Loewenberg, M. 1998 Mechanisms of drop breakup in flow through fixed beds via numerical simulations. AICHE Annual Meeting, Miami Beach, Fla.

Sibilla, S. and Baron, A. 2002 Polymer stress statistics in the near-wall turbulent flow of a drag-reducing solution. *Phys. Fluids* **14(3)**, 1123–1136.

Smith, D., Babcock, H. and Chu, S. 1999 Single polymer dynamics in steady shear flow. *Science* **283**, 1724–1727.

Smith, D. E. and Chu, S. 1998 Response of flexible polymers to a sudden elongational flow. *Science* **281**, 1335–1340.

Smith, D. E., Perkins, T. T. and Chu, S. 1996 Dynamical scaling of DNA diffusion coefficients. *Macromolecules* **29(4)**, 1372.

Somandepalli, V. S. R., Hou, Y. X. and Mungal, M. G. 2005 Streamwise evolution of drag reduction in a boundary layer with polymer injection. Proc. 2nd Int. Symp. on Sea water Drag Reduction, Busean, Korea.

Somandepalli, V. S. R., White, C. M. and Mungal, M. G. 2003 Boundary layer studies on polymer drag reduction using PIV and PLIF. *Proc. ASME FEDSM* .

Somasi, M., Komami, B., Woo, N., Hur, J. and Shaqfeh, E. 2002 Brownian dynamics simulations of bead-rod and bead-spring chains: Numerical algorithms and coarse graining issues. *J. Non-Newtonian Fluid Mech.* **108**, 227–255.

Sreenivasan, K. R. and White, C. M. 2000 The onset of drag reduction by dilute polymer additives, and the maximum drag reduction asymptote. *J. Fluid Mech.* **409**, 149.

Stone, P. A. and Graham, M. D. 2003 Polymer dynamics in a model of the turbulent buffer layer. *Phys. Fluids* **15(5)**, 1247–1256.

Stone, P. A., Roy, A., Larson, R. G., Waleffe, F. and Graham, M. D. 2004 Polymer drag reduction in exact coherent structures of plane shear flow. *Phys. Fluids* **16(9)**, 3470–3482.

Stone, P. A., Waleffe, F. and Graham, M. D. 2002 Toward a structural understanding of turbulent drag reduction: nonlinear coherent states in viscoelastic shear flows. *Phys. Rev. Lett.* **89(20)**, 208301.

Sureshkumar, R., Beris, A. N. and Handler, R. A. 1997 Direct numerical simulation of the turbulent channel flow of a polymer solution. *Phys. Fluids* **9(3)**, 743.

Tabor, M. and de Gennes, P.-G. 1986 A cascade theory of drag reduction. *Europhys. Lett.* **2**, 519.

Taylor, G. I. and Green, A. E. 1937 Mechanism of the production of small eddies from large ones. *Proc. R. Soc. Lond.* **A158**, 499–521.

Terrapon, V. E., Dubief, Y., Moin, P. and Shaqfeh, E. S. G. 2003 Brownian dynamics simulation in a turbulent channel flow. ASME-JSME, Honolulu, Hawaii USA.

Terrapon, V. E., Dubief, Y., Moin, P., Shaqfeh, E. S. G. and Lele, S. K. 2004 Simulated polymer stretch in a turbulent flow using Brownian dynamics. *J. Fluid Mech.* **504**, 61–71.

Thiffeault, J.-L. 2003 Finite extension of polymers in turbulent flow. *Phys. Lett. A* **308**, 445–450.

Thirumalai, D. and Bhattacharjee, J. K. 1996 Polymer-induced drag reduction in turbulent flows. *Physical Review E* **53**, 546.

Toms, B. 1948 Observation on the flow of linear polymer solutions through straight tubes at large reynolds numbers. *In Proc. Intl Rheological Congress*, , vol. 2, pp. 135–141. Holland.

Treloar, L. R. G. 1975 *The Physics of Rubber Elasticity.*, 3rd edn. Oxford University Press.

Ucinski, D. 1999 *Measurement Optimization for Parameter Estimation in Distributed Systems.*. Technical University Press, Zielona Gora, Poland.

Virk, P. S. 1975 Drag reduction fundamentals. *AIChE J.* **21**, 625.

Virk, P. S., Merril, E. W., Mickley, H. S., Smith, K. A. and Mollo-Christensen, E. 1967 The toms phenomenon - turbulent pipe flow of dilute polymer solutions. *J. Fluid Mech.* **30**, 305–328.

Walker, D. T. and Tiederman, W. G. 1990 Turbulent structure in a channel flow with polymer injection at the wall. *J. Fluid Mech.* **218**, 377–403.

Wapperom, P., Keunings, R. and Legat, V. 2000 The backward-tracking Lagrangian particle method for transient viscoelastic flow. *J. Non-Newtonian Fluid Mech.* **91**, 273–295.

Warholic, M. D., Heist, D. K., Katcher, M. and Hanratty, T. J. 2001 A study with particle image velocimetry of the influence of drag reducing polymers on the structure of turbulence. *Exp. Fluids* **31**, 474–483.

Warholic, M. D., Massah, H. and Hanratty, T. J. 1999 Influence of drag-reducing polymers on turbulence: effects of reynolds number, concentration and mixing. *Exp. Fluids* **27**, 461–472.

Warner, H. R. 1972 Kinetic theory and rheology of dilute suspensions of finitely extendible dumbbells. *Ind. Eng. Chem. Fundamentals* **11**, 379–387.

White, C. M., Somandepalli, V. S. R., Dubief, Y. and Mungal, M. G. 2005 Dynamic contributions to the skin friction drag in polymer drag reduced wall-bounded turbulence. *submitted to Phys. Fluids* .

White, C. M., Somandepalli, V. S. R. and Mungal, M. G. 2004 The turbulence structure of drag reduced boundary layer flow. *Exp. Fluids* **36**, 62–69.

Yeung, P. and Pope, S. 1988 An algorithm for tracking fluid particles in numerical simulations of homogeneous turbulence. *J. Comp. Phys.* **79**, 373–416.

Yu, B. and Kawaguchi, Y. 2004 Direct numerical simulation of viscoelastic drag-reducing flow: a faithful finite difference method. *J. Non-Newton. Fluid Mech.* **116**, 431–466.

Zhou, Q. and Akhavan, R. 2003 A comparison of fene and fene-p dumbbell and chain models in turbulent flow. *J. Non-Newton. Fluid Mech.* **109**, 115–155.

Zimm, B. H. 1956 Dynamics of polymer molecules in dilute solution: Viscoelasticity, flow birefringence and dielectric loss. *J. Chem. Phys.* **24**, 269–278.